UNIVERSITÄT DUISBURG ESSEN

Open-Minded

Investigating magnetic and optical properties of hybrid magnetic-noble metallic nanowires synthesized by electrodeposition

Dissertation

zur Erlangung des akademischen Grades
Doktor der Naturwissenschaften
Von der Fakulät für Physik
der Universität Duisburg-Essen

vorgelegt von

Behnaz Arvan

aus

Qazvin, Iran

Duisburg, Dezember 2016

Dedicated to

my Parents and my Family

Abstract

The structural and magnetic properties of Ni nanowires (NWs) electrodeposited in anodic aluminum oxide (AAO) membranes with diameters in the range from 35 to 75 nm and an interpore distance of 105 nm have been investigated. The expected interplay between the shape anisotropy and the dipole-dipole interactions between the NWs of different aspect ratios and packing density is analyzed. The growth rate, crystallinity, and magnetic properties of the NWs with diameter 45 nm are compared as a function of different electrodeposition potentials (-0.8V to -1.5V vs. the Ag/AgCl) to optimize the deposition process. It is observed that the average growth rate of the synthesis increases nearly linearly by increasing the deposition potential. The synthesized NWs with different deposition potentials are uniform and mostly polycrystalline but with larger grain sizes up to 50 nm for nanowires synthesized at -1 V and -1.1 V. The magnetic properties (coercivity and remanence) of the NWs (fcc structure) with the same aspect ratio are independent on the deposition potentials. It is found that for NWs with 40 nm diameter, the shape anisotropy dominates the magnetic properties. Annealed Ni NWs (650◦C under Ar atmosphere for 24h) show a smaller coercivity than as-prepared samples which suggests a lower defect density inside the nanowires. The FMR measurements on two samples of Ni NWs with different diameters (35 nm and 45 nm) but with the same length (1.6 µm), and the interpore distance of 105 nm reveal the effect of the magnetic dipole-dipole interactions between the nanowires on the effective anisotropy field. The effective field of 35 nm diameter, with the dipolar field of 68.5 mT, is μ_0H_{eff}=215 mT, while for 45 nm diameter, with the dipolar field of 109.5 mT, is μ_0H_{eff}=160 mT.

In a second study, hybrid nanowires consisting of Ni and Ag segments have been synthesized and characterized by structural, magnetic, and optical techniques. The electrodeposition process was optimized to create Ni-Ag NWs with sharp interfaces. It is demonstrated that the localized surface plasmon resonance transverse mode of the Ag segment (75($\pm$5) nm diameter and the length of 210($\pm$20) nm) changes by 12 nm with the wavelength of 438 nm due to the contact to ferromagnetic Ni. It is also revealed that higher order transverse plasmon modes of the Ag segment can clearly be identified as a distinct peak at 366 nm in the hybrid of Ag/Ni NWs rather than for individual Ag NWs that appeared as a shoulder at 375 nm. In addition, one high intensity plasmon peak at 313 nm related to Ni segments is observed.

In a third study, a new approach for the design, synthesis and optimization of complex Ni capped Ag nanohybrids, was investigated. This technique is carried out using a multi-step process combining electrochemical deposition and partial removal of the membrane.

Zusammenfassung

In dieser Arbeit werden Ni Nanodrähte mit Durchmessern von 35 nm bis 75 nm und einem mittleren Lochabstand von 105 nm durch die Elektrodeposition in anodischem Aluminiumoxid (AAO) präpariert und deren strukturelle und magnetische Eigenschaften bestimmt. Das Wechselspiel zwischen magnetischer Formanisotropie und der Dipol-Dipol-Wechselwirkung zwischen den Nanodrähten mit unterschiedlichem Aspektverhältnis wird untersucht. Die Wachstumsgeschwindigkeit, die Kristallinität und die magnetischen Eigenschaften von 45 nm Ni Nanodrähten in der AAO-Matrix werden für verschiedene elektrische Potentiale (-0.8 V bis -1.5 V) verglichen, um die optimalen Depositionsparameter zu finden. Es wird beobachtet, dass die mittlere Depositionsrate nahezu linear mit wachsendem Potential steigt. Die erhaltenen kubisch-flächenzentrierten Nanodrähte wachsen homogen und polykristallin mit einer optimierten Korngröße bis zu 50 nm für Potentiale zwischen -1.0 V und -1.1 V. Das Koerzitivfeld und die remanente Magnetisierung der Ni Nanodrähte sind für ein identisches Aspektverhältnis jedoch unabhängig vom Depositionspotential. Vielmehr dominiert die Formanistropie die magnetischen Eigenschaften. Thermische Nachbehandlung der Ni Drähte (650°C for 24h in Ar atmosphere) führt zu kleineren Koerzitivfeldern, was auf eine kleinere Defektdichte in den Nanodrähten hindeutet. Messungen der ferromagnetischen Resonanz an Ni Nanodrähten unterschiedlichen Durchmessers (35 nm und 45 nm) aber identischer Länge (1.6 µm) und mittlerem Abstand (105 nm) offerbaren den Effekt der Dipol-Dipol-Kopplung auf das effektive Anisotropiefeld H_{eff}. 35 nm Nanodrähte mit dem Dipolfeld von 68.6 mT haben $\mu_0 H_{eff} = 215\ mT$, während die 45 nm Nanodrähte ein Dipolfeld von 109.5 mT und $\mu_0 H_{eff} = 160\ mT$ zeigen.

In einer zweiten Untersuchung werden hybride Ag/Ni Nanodrähte synthetisiert und ihre strukturellen, magnetischen und optischen Eigenschaften untersucht. Hierbei wird die Elektrodeposition auf scharfe Grenzschichten optimiert. Es wird gezeigt, dass sich die transversale Mode der lokalisierten Oberflächenplasmonen des Ag-Segments (Durchmesser 75±5 nm und Länge 210±20 nm) durch den Kontakt zum Ni um 12 nm zu kleineren Wellenlängen verschiebt. Plasmonenmoden höherer Ordnung des Ag-Segments zeigen ebenfalls diese Verschiebung von 375 nm in freien Ag-Segmenten zu 366 nm in hybriden Ag/Ni Nanodrähten. Zusätzlich wird bei 313 nm eine starke Resonanz beobachtet, die den Ni-Segmenten zugeschrieben werden kann.

In einer dritten Studie wird ein neuer Ansatz für das Design und die Synthese komplexer Ni-bedeckter Ag-Nanohybride vorgestellt. Hier wird eine mehrstufige Technik eingesetzt, die die Elektrodeposition mit dem partiellen Entfernen der Membran kombiniert.

List of Abbreviations

AAO	Anodic aluminum oxide
DC	Direct current
EDX	Energy dispersive X-ray spectroscopy
FCC	Face centered cubic
FMR	Ferromagnetic resonance
HRTEM	High resolution transmission electron microscopy(e)
LSPR	localized surface plasmon resonance
TEM	Transmission electron microscopy(e)
SAED	Selected area electron diffraction
SEM	Scanning electron microscopy(e)
SQUID	Super Quantum Interference Device
XRD	X-ray diffraction
UV/VIS	Ultraviolet and visible

Contents

1 Introduction

Metallic nanostructured materials have attracted extensive attention because of their unique physical and chemical properties. In particular, the nanostructured ferromagnetic materials are of great interest in theoretical physics and practical technological applications such as ultra-high density magnetic media, spintronics, nano-sensors, high-frequency devices, optical and microwave and sensors for biological analysis [1-5]. Many works have been done to synthesize nanoparticles, nanotubes, nanorods and nanowires. The advantages of using nanowires are related to the favorable geometrical anisotropy and magnetic dipole-dipole interaction linked to the nanowire shape.

Among the ferromagnetic materials, large-scale nickel nanowire arrays are excellent candidate structures for high-density magnetic recording media as well as microwave-absorbing properties. Furthermore, nickel has been proven to be an appropriate material for fabricating biological sensors because of the detection of carbohydrates such as glucose [6].

Some methods including lithographic methods, wet chemical processes and membrane-based techniques are well known for the synthesizing of metallic nanowires. Among these approaches, membrane-based techniques provide an alternative method because of their low cost, high throughput, and high efficiency in fabricating different metallic nanowires. Typically, nanowires can be obtained by using porous membranes such as polycarbonate track-etch membranes, block copolymer and anodic aluminum oxide (AAO) membranes. AAO membranes enable the synthesis of large scale arrays of nanowires perpendicularly aligned on a substrate. However, the uniform accurate alignment of nanowires perpendicular to the substrate remains as a challenge. AAO membranes containing highly dense and ordered cylindrical nanochannels have been developed in the past two decades and have greatly advanced the synthesis of one-dimensional (1D) nanostructures, such as nanorods, nanowires, nanobelts and nanotubes.

These nanostructures are usually created by electrochemical methods in a bottom-up strategy. The pore structures of AAO membranes are adjusted by different fabrications routes to adjust the structural parameters (diameter, length, and porosity). In addition, AAO

membranes provide high structural regularity and controllability of the nanowire arrays (tuning the morphology, size, high packing density and highly ordered distributions). Typically for ferromagnetic nanowires the most significant magnetic properties such as magnetic saturation, coercivity, remanence depend crucially on the diameter and length of the nanowires. AAO gives an opportunity to control the size of the nanowires which allows to tune the magnetic properties.

The enhancement of shape anisotropy in nanowires with a high aspect ratio competes with bulk magnetocrystalline anisotropy that plays a crucial role in determining various magnetic properties. In general, the magnetic nanowires represent uniaxial anisotropy with the direction of the easy axis of magnetization parallel to the wire axis for small diameters that arises because of their strong shape anisotropy in cylindrical nanowires.

Typically, for polycrystalline magnetic nanowires, shape anisotropy dominates the magnetization reversal process because of randomly orientated grains which decreases the contribution of magnetocrystalline anisotropy. However, for single crystalline magnetic nanowires the magnetization reversal is determined by the interplay between shape anisotropy and magnetocrystalline anisotropy.

Other the methods for filling of a membrane with a desired material exist with CVD (chemical vapor deposition) it is difficult to achieve a complete filling of the membrane or by the sol gel technique it is difficult to control the length of the nanowires. The electrochemical deposition enables to fill the pores completely with precise control of the length of the nanowires under potentiostatic deposition mode by monitoring the current density and the electric charge transients.

In the recent years, many works have been done to synthesize Ni nanowires of polycrystalline and single crystalline structures with various growth orientations by controlling the electrodeposition conditions. However, some of these results are in conflict for synthesizing Ni nanowires using direct current (*DC*) potentiostatic mode. In 2003, Mingliang Tian et al. reported that the higher binding energies of Ni lead to aggregation of atoms into 3D clusters yielding polycrystalline Ni nanowires [7]. In contrast, in 2005 Pan et al. reported the fabrication of single crystal Ni nanowires, and it was experimentally demonstrated that the crystallinity and growth orientation of Ni nanowires depend on the electrolyte temperature, while they are independent of the *pH* value of the electrolyte [8]. Then, in 2009, Andrea Cortes et al. studied on the effect of the deposition conditions on the structure of Ni nanowires and reported that the *pH* value of the electrolyte influences the crystallinity while electrolyte temperature influences the quality of the crystallinity of the synthesized nanowire [9]. Many scientific efforts have been

done to synthesize the Ni nanowires, and it was mentioned that the potential deposition can crucially effect the crystalline structure of the nanowires. In a limited reduction potentials, single crystalline Ni nanowires are produced.

One of the aims of this PhD work is to synthesize Ni nanowires and investigate the structural and crystallinity of the nanowires and optimize the process of the electrodeposition as a function of the deposition potentials. In addition, understanding of the magnetic behavior of individual nanowires as well as of the effects of dipole-dipole interactions among the highly-ordered arrays of Ni nanowires inside the membrane with diameters in the range of 35-85 nm with the interpore distance of 105 nm are desired.

Plasmonic devices have recently increasing applications in broad fields including nanoantennas, biosensors, solar cells, photonics, medicine, and manufacturing of electronic and display devices because of their superior electrical and thermal conductivity, in addition to their ability to act as optical waveguides [10]. Plasmon resonance based on nanometer-sized metallic particles is an important process in obtaining selective optical transmission and absorption spectra. It has potential applications in many fields, such as optical lithography, sensing devices, and Raman spectroscopy. Noble metal nanostructures such as copper, gold and silver have a strong surface plasmon resonance (SPR) in the visible spectral region caused by the coherent motion of conduction band electrons [11].

In fact, the synthesis of the integration of multiple materials into a single, nanohybrid structures has gained a tremendous amount of attention in recent years due to their increased functionality. Combining multiple materials into one structure combined physical properties and introduces unique properties in comparson to single-component materials [12]. Low dimensional magnetic/noble hybrids can be materials that combine functional magnetic and optical properties to produce a new class of magnetically and optically active materials. This may include new or improved chemical and physical properties that can be exploited for fabricating novel nanoscale devices. For synthesizing bimetallic nanostructures two main problems arise: 1) the galvanic replacement reactions between two different metals; and 2) the tendency of alloy formation of the metals [12]. In this work, Ag is a good alternative as a noble metal for synthesizing hybrid segmented of Ag and Ni because they are immiscible and expected to form sharp interface [13].

The control of localized surface plasmon resonance (LSPR) is a key feature that dictates the performance of nanoscale optic and photonics devices, as well as the fabrication of biosensors. [14] In general, the frequency of the LSPR oscillation can be tuned actively through

the size, shape, composition and the dielectric function of the metal and the surrounding medium [14-16]. Among these approaches that have been proposed to achieve active plasmonics, an external magnetic field can also modify the properties of electron plasma [17-20]. Pineider et al, studied the effect of a magnetic field on plasmonic resonance of colloidal gold nanoparticles [17] but the magnetic fields that enable noticeable changes in noble/metal plasmonic structures in the visible spectral range are of the order of several tesla that are too large for realistic applications [19]. Many works have been studied an enhanced magneto-optical response based on ferromagnetic and noble metal heterostructures to observe magneto-plasmonic effects [17, 20-23]. Bratschitsch et al. studied the combination of magnetic and plasmonic counterparts in a magneto-plasmonic system to modify the wave propagation vector of plasmon resonance [19].

Since a magnetic field can optimize the properties of one electron plasma [19], in this work the main approach was to investigate the effect of ferromagnetic metal, Ni, on the optical properties of a noble metal, Ag, by combining magnetic and plasmonic counterparts in a hybrid nanowire. Consequently, a novel optical property of Ag (by tuning the plasmon frequency), especially because of its low energy loss in visible range of spectrum [24], is offered in a combination of Ni-Ag-Ni hybrid nanowires.

On the other hand, plasmons in ferromagnetic metals reveal a stronger damping [25], however, they possess the advantage of stronger magnetic polarization so make them suitable for nanoantenna combine with their optical plasmon resonance [20]. Hybrid structures consisting of noble and ferromagnetic lead to overcome this excess damping because the noble metals increase the plasmon response.

Many different types of multicomponent nanostructures contain heterojunctions between combinations of the two materials have been successfully fabricated with a variety of shapes and sizes [26-29]. Despite this success, the synthesis, and the design of more complex multicomponent nanostructures, particularly, core-shell nanostructures are desired. In fact, the morphological complexity can often provide a wide range of innovative properties that are used for innovative device production. In this thesis, an innovative method for synthesizing and designing of very complex multicomponent of Ni capped Ag nanohybrids, is investigated. This method is achieved by using a multi-step process combining electrocehmical deposition and the partly removing the AAO membrane.

In summary, the overall goal of this PhD dissertation is the design, the synthesis, and the thorough structural and magnetic characterization of pure Ni and the optical and magnetic

characterizations of the hybrid structures consisting of Ni and Ag to study the interplay between a ferromagnetic and noble metals on their optical and magnetic properties.

In addition, the design and the synthesize of the complex multicomponent of Ni and Ag is described.

The PhD thesis is divided into the following chapters. The introductory chapter includes the theoretical background of the magnetism and plasmonic at the nanoscale, the principles of the membrane-based electrodeposition that have been used. In the chapters presenting the synthesize procedure and scientific results as well as the thorough morphological, and structural characterizations.

2 Theoretical background

In this chapter, the fundamentals of magnetism and plasmonics in nanoscale systems are discussed that will be used for analyses of the experimental results. Finally, the method of synthesizing nanowires in this PhD thesis is explained.

2.1 Fundamentals of Magnetism in nanoscale range

The fundamentals of the magnetic properties of nanostructures are summarized using the references [30-36].

The emergence of novel magnetic properties of magnetic nanowires and nanoparticles has attracted considerable interest in recent years. Two reasons for new magnetic properties when the dimension approaches to a few tens of nanometer are:

1. A significant fraction of the total number of atoms is at the surface of the crystal and causes changes in the electronic structure and a large magnetic surface anisotropy due to the break of symmetry.
2. The size of the nanostructure can be smaller than the critical length of some interaction, e.g. exchange length.

The origin of magnetism of single atom comes from the motion of electrons around the nucleus and the intrinsic spin of the electrons. The atomic *d*-orbitals of the transition atoms are not filled so the spins of the electrons are unpaired giving the atom a net magnetic moment. The interaction between atomic magnetic moments in a crystal is of two types:

1. The exchange interaction comes from the overlap of the *d* orbitals of different transition metals. The exchange interaction is short-range and between two spins S_i and S_j of two neighboring atoms within the Heisenberg model can be described by:

$$E_{ex} = -2JS_i . S_j \quad (2.1)$$

where J is the exchange constant and for $J > 0$ and $J < 0$ parallel and antiparallel alignment of spins is favored, respectively. If J is positive a ferromagnet appears. Indeed, the exchange interaction results from the coulomb energy and symmetry consideration for fermions. According to the Pauli exclusion principle, two electrons at the same quantum electronic state can only have the opposite spins.

2. The dipole-dipole interaction represents the interaction between two magnetic dipoles, and it is long-range. The exchange interaction is about 10^3 times bigger than the dipole interaction of nearest magnetic moment [37].

Spontaneously, in a bulk ferromagnet (below the Curie temperature), magnetic domains are formed to decrease the magnetostatic energy of the whole system. The magnetostatic energy represents the interaction energy of each dipole with the magnetic field generated by the other dipoles throughout the crystal. As the result, a single-domain structure, has higher dipolar energy than any structure consisting of two or more domains with opposite magnetization.

Minimization of the magnetostatic energy of a ferromagnet in a demagnetized state can be achieved by formation of domains. On the other hand, the exchange energy of the ferromagnet will increase because of the antiparallel alignment of the spins adjacent to the boundary between the domains (domain wall). The exchange energy can be minimized if the spins directions change gradually inside the boundary and not abruptly. In fact, the thickness of the domain wall is determined by the competition between exchange energy and anisotropy energies (see section 2.1.2).

The domain configuration and its average size in a ferromagnetic material is the result of the minimization of the magnetostatic energy, the exchange energy, and the anisotropy energy. As the result, if the volume of a sample decreases to below a certain critical value that energetically favors just one domain so this sample stays permanently magnetized. This critical size depends on type of the material and the morphology.

In this thesis, Ni nanowires with diameter between 35 nm and 75 nm are investigated and a single domain wire is expected for Ni with diameter less than 55 nm [38].

2.1.1   Magnetic anisotropy

The magnetic anisotropy energy (MAE) in a ferromagnetic material is the energy difference associated with rotating the magnetization from the direction of minimum of ground

state energy (easy axis) to the direction of maximum ground state energy (hard axis). The two microscopic sources of MAE are: 1. the spin- orbit interaction that couples the spin to the lattice and 2. the dipole-dipole interaction between the magnetic moments.

The effective magnetic anisotropy energy density for a ferromagnetic material, with a significant contribution of surface anisotropy, is composed of different contribution:

$$K = K_{magnetocrystalline} + K_{shape} + K_{surface} + K_{strain} + K_{exchange} \quad (2.2)$$

2.1.1.1 Magnetocrystalline anisotropy energy

The origin of the magnetocrystalline anisotropy is the spin-orbit interaction. By applying an external field, the magnetic moment is forced to rotate consisting of spin and orbital moment. The orbital momentum couples to the spin lattice. The simplest form of crystal anisotropy is the uniaxial anisotropy energy which is given by

$$E_{uni} = K_u V sin^2\theta \quad (2.3)$$

where K_u is the effective uniaxial anisotropy energy density constant, V is the sample volume and θ is the angle between the symmetry axis and the magnetization. The magnetocrystalline anisotropy also depends on the symmetry of the sample. For cubic structure the magnetocrystalline anisotropy is in the range 0.2 $\mu eV/atom$ for Ni (FCC) and 1.4 $\mu eV/atom$ for Fe (BCC) while 70 $\mu eV/atom$ for Co with HCP crystalline structure [39].

2.1.1.2 Shape anisotropy energy

The shape anisotropy depends on the shape of the magnetic material comes from the anisotropy of the demagnetizing field arising from the poles at the surface. The energy related to the demagnetizing field of a sample with volume V is given by

$$E = \frac{\mu_0}{2} \int \vec{M} \vec{H_d} dV \quad (2.4)$$

where M is magnetization and H_d is the demagnetized field which is given by

$$\vec{H_d} = N\vec{M} \quad (2.5)$$

N is in general the demagnetization tensor, and for all samples except a sphere is anisotropic.

In general, the shape anisotropy energy density for a homogenously magnetized sample is given by

$$K_{shape\ anisotropy} = \frac{\mu_0}{2}(N_x M_x^2 + N_y M_y^2 + N_z M_z^2) \quad (2.6)$$

with the components of the magnetization M_i and the components of the demagnetization factors that the sum of them of a material must be 1

$$N_x + N_y + N_z = 1 \quad (2.7)$$

As an example, the shape anisotropy energy density for a prolate ellipsoid that is uniaxial is given by

$$F_d = \frac{1}{2}\mu_0 M^2 N_z + \frac{1}{2}\mu_0 M^2 (N_x - N_z)sin^2\theta \quad (2.8)$$

Consequently, the shape anisotropy constant is given by the θ –dependent part of the anisotropy energy

$$K_d = \frac{1}{2}\mu_0 M^2 (N_x - N_z) = \frac{1}{2}\mu_0 \Delta N M^2 \quad (2.9)$$

For a system with uniaxial shape anisotropy, it is easier to magnetize the sample along its long axis, in other words, the demagnetizing field is lower. In this case, the demagnetizing factors are given by

$$N_z(long\ axis) = \frac{1}{m^2-1}\left[\frac{m}{\sqrt{m^2-1}}ln\left(\frac{m+\sqrt{m^2-1}}{m-\sqrt{m^2-1}}\right) - 1\right] \quad (2.10)$$

$$\text{for } m \gg 1, \ N_x = N_y = \frac{1}{2}\left[1 - \frac{ln(2m-1)}{m^3}\right]$$

m represents the aspect ratio of the ellipsoid between the long and short axes. For a cylinder with infinite length, if the sample is magnetized along the long axis, $N_z = 0$ and if magnetized along the short axis $N_x = N_Y = 1/2$.

The anisotropic part of the total energy of a system equals the sum of all contributions that is magnetocrystalline anisotropy and the shape anisotropy. Particularly, for Ni with low magnetocrystalline anisotropy respecting to $K_{mc} = -0.5 \times 10^4 (J/m^3)$, the shape anisotropy energy overcomes it. As the result, the magnetic properties are dominated by the shape anisotropy, and other contributions act as perturbations. In the case of Ni nanowires, the magnetic properties can be tuned by changing the aspect ratio of them.

2.1.1.3 Surface anisotropy energy

This additional magnetic anisotropy for nanosized materials arises from breaking of symmetry (at facets and edges). In comparison to bulk materials, the ratio of surface to volume atoms in nanoparticles is large. By the reduction of the coordination number of the atoms and different lattice spacing at the surface, electronic structure and magnetic interactions at the surface is different from the volume. As the result, there is additional contribution to the magnetic anisotropy that enhances by decreasing the size of the sample.

In a phenomenological approach based on the model of Neel's anisotropy [40] the magnetic anisotropy on a given surface atom is calculated by considering all magnetic pair interactions of its nearest neighbors $L(\vec{m}.\vec{r_{ij}})^2$. Subsequently, the surface anisotropy energy for the whole particles is given by

$$E_{surface\ anisotropy} = \frac{L}{2}\frac{\sum_{i,j}(\vec{m}.\vec{r_{ij}})^2}{\|\vec{r_{ij}}\|^2} \qquad (2.11)$$

where L is the Neel constant and depends on the interatomic distance r and $\vec{m}$ is the unit vector along the local magnetization direction.

The effective anisotropy (K_{eff}), which describes the magnetic anisotropy for single nanoparticle, gains contribution from the volume atoms as well as the surface anisotropy which in the first order is supposed to be uniaxial. In the case of spherical particles, the effective anisotropy is given by

$$K_{eff} = K_V + \frac{S}{V}K_S \qquad (2.12)$$

K_V and K_s are the volume and surface anisotropy constant, respectively and S and V are the surface and volume of the sphere, respectively.

2.1.1.4 Strain anisotropy energy

The strain anisotropy arises from a magnetostrictive effect. A local change of atomic positions leads to a change of the shape of the orbitals and consequently the spin-orbit interaction. The strain magnetic anisotropy is given by

$$E_{strain\ anisotropy} = -\frac{3}{2}\lambda_s \sigma S cos^2\theta \qquad (2.13)$$

λ_s is the saturation magnetostriction (for bulk Ni, -33×10^{-6} [41]), σ is the strain per area, S is the sample surface and θ is the angle between the magnetization and the strain axis. Consequently, the strain anisotropy constant is given by [42]

$$K_1 = \frac{3}{2}\lambda_s\sigma \qquad (2.14)$$

The electrodeposited Ni nanowires inside a membrane are subjected to large and almost uniaxial strains [42-44].

2.2 Ferromagnetic resonance (FMR)

FMR is the standard experimental technique that is used for investigation the basic parameters of ferromagnetic materials such as: the saturation magnetization, anisotropy constants, g-factor, information about exchange interaction and dipolar interactions. FMR has been widely used for studying magnetic nanowires.

FMR is caused by precession of motion of spins in an external magnetic field toward the new equilibrium position. The theory of FMR is based on the Landau–Lifshitz–Gilbert equation. More information can be found in [45,46].

For hexagonal arrays of ferromagnetic nanowires the free energy density is given by considering Zeeman energy and the effective anisotropy energy [47,48]

$$K = -\vec{M}.\vec{H} + K_{eff}sin^2\theta \qquad (2.15)$$

The first term corresponds to the Zeeman energy, where M and H indicate magnetization and external magnetic field, respectively and the second term is the effective anisotropy energy. K_{eff} is the effective uniaxial anisotropy, represents the exchange and dipolar interactions within the system of spin as well as the interaction of the spin with the lattice, which can be written as

$$K_{eff} = \frac{\mu_0}{2}M^2(1 - 3P) + K_u \qquad (2.16)$$

The first term indicates the dipole-dipole interactions between nanowires embedded inside the membrane [48,49] and the second term is the second-order uniaxial anisotropy (for Ni, $K_u = -0.5 \times 10^4\,J/m^3$). P is the porosity of the membrane that is calculated by

$$P = \frac{\pi}{2\sqrt{3}}\frac{d^2}{r^2} \qquad (2.17)$$

where d is the pore diameter and r is the interwire distance (Figure 2.1).
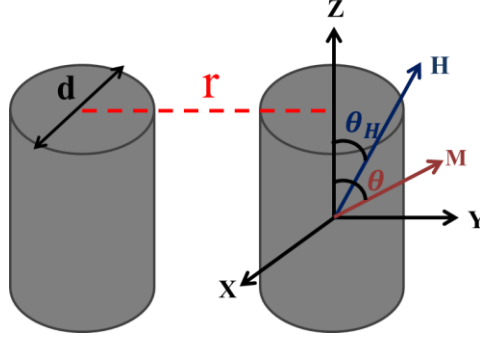
Figure 2.1. Schematic description of nanowires with diameter *d*, interpore disatance *r*. *θ* and *θ*_H represent the angles between the longitudinal axis (anisotropy axis) of the nanowires with $\vec{M}$ (the magnetization) and $\vec{H}$ (the external magnetic field), respectively.

The resonance condition for uniaxial ferromagnet by solving the Landau–Lifshitz–Gilbert equation is given by

$$\left(\frac{\omega}{\gamma}\right)^2 = \left[H_r \cos(\theta - \theta_H) + H_{eff} \cos^2\theta\right]\left[H_r \cos(\theta - \theta_H) + H_{eff} \cos 2\theta\right] \quad (2.18)$$

where $\omega = 2\pi f$ and for our experiment $f = 9.7 GHz$, and $\gamma = g\mu_B/\hbar$ is the gyromagnetic ratio, H_r is the resonance field and H_{eff} is an effective anisotropy field. The effective anisotropy field is written as

$$H_{eff} = \frac{\mu_0}{2} M_S (1 - 3P) + 2\frac{K_u}{M_S} \quad (2.19)$$

According to the resonance field obtained from FMR measurement, the effective anisotropy field can be calculated for two cases depending on the direction of the external magnetic field with respect to the long axis of the nanowires: parallel (1) and perpendicular (2):

1) $\theta_H = \theta = 0°$

$$\frac{\omega}{\gamma} = H_r + H_{eff} \quad (2.20)$$

2) $\theta_H = \theta = 90°$

$$\left(\frac{\omega}{\gamma}\right)^2 = H_r(H_r - H_{eff}) \quad (2.21)$$

2.3 Fundamentals of Plasmonics

The present summary of the plasmonic properties of nanostructures has been prepared based on basic literatures [50-55].

As it was mentioned in section 2.1, the large percentage of atoms on the surface of nanostructures is one of the principle factors that leads to different physical properties from those of the bulk materials. In addition, a reduction in size leads to different optical properties. In other words, by reducing the size and the dimensionality of a material, the density of states is reduced, therefore, the electronic properties change drastically. In metals the density of energy levels is so high, that a significant separation of energy levels of the conduction band will be observed only in nanoparticles with just a few atoms.

2.3.1   Surface Plasmons

The research area of plasmonics refers to manipulating light by metals at nanoscale size [56]. A plasmon is a collective excitation of a conductive electron gas in a metal. The excitation of a plasmon arises of the interaction between the electromagnetic field and free electrons in a metal, and this interaction can be understood using the classical Maxwell's equations.

The electric component of light can excite the free electrons in the metal that can generate collective oscillations of electron densities. There are two main ingredients of plasmonics [57]: 1) surface plasmon polaritons that refers to the propagating of an electromagnetic wave along the interface of metal- dielectric and 2) localized surface plasmon resonance that refers to the interaction between the collective oscillation of conduction electrons on the metal surface and an alternating electric field of incident light [58,59].

The frequency and width of the surface plasmon resonance depend in the size, shape, composition, and the dielectric function of the metal as well as the surrounding medium [57]. In noble metals, the electrons of conduction-band can be well approximated by the Drude model. In this model, the conduction-band electrons are supposed to move freely and independently from the ionic background, whereas the ions act as scattering centers, which occur with an average rate of $\gamma = \frac{1}{\tau}$ and τ is the relaxation time. In an external field only the electrons near the Fermi level are accelerated. According to the band theory there is a correction of the movement of electrons and this correction is incorporated into an effective mass that is denoted by m^*, and in general it is different from the free-electron mass m_e.

By assuming the Drude model, the equation of motion of free electrons oscillating in an electric field $\vec{E}_t = \vec{E}_0 e^{-i\omega t}$ is given by

$$m_e \frac{d^2\vec{X}}{dt^2} + m_e \gamma \frac{d\vec{X}}{dt} = -e\vec{E} \qquad (2.23)$$

where m_e is the effective free electron mass. The solution of this equation can describe the oscillation of the electron, $\vec{X} = \vec{X}_0 e^{-i\omega t}$. The polarization, $\overrightarrow{P}$, that describes the density of the electric dipole moments per unit volume of a dielectric material is given by $\vec{P} = -ne\vec{X}$, n is the density of conduction electrons. In noble metals, the electrons have a higher possibility to polarize so the surface plasmon resonance occurs with a lower frequency.

The dielectric function of Drude form can be written as

$$\varepsilon(\omega) = \varepsilon_\infty - \frac{\omega_p^2}{\omega^2 + i\gamma\omega} \qquad (2.24)$$

where ε_∞ refers to the contribution of the bound electron to the polarization and if only the conduction band electrons contribute to the dielectric function it will be 1, and ω_p is the plasma frequency of the free electron gas and is defined by the relation

$$\omega_p = \sqrt{\frac{ne^2}{\varepsilon_0 m^*}} \qquad (2.25)$$

By neglecting γ, the Drude dielectric function simplifies to $\varepsilon(\omega) = 1 - \omega_p^2/\omega^2$ and two frequency regions are distinguished: If $\omega > \omega_p$, $\varepsilon(\omega)$ is positive leads to have real refractive index $n = \sqrt{\varepsilon(\omega)}$ and if $\omega < \omega_p$, $\varepsilon(\omega)$ is negative leads to imaginary refractive index that implies the electromagnetic field cannot propagate inside the metal. The dielectric function can be described in terms of a complex function, $\varepsilon = \varepsilon_1 + i\varepsilon_2$.

Table 2.1 represents the Drude-parameters for the noble metals.

TABLE 2.1. Presents the relevant values for the noble metals. The electron density n from Kopitzki (1993) and the ratio of the effective mass to the mass of electron m^*/m_e from Johnson and Christy (1972). [Carsten Sönnichsen, PhD thesis, Ludwig-Maximilians University; 2001]

	$n\ (10^{28}\text{m}^{-3})$	$\omega_P\ (10^{16}s^{-1})$	m^*/m_e	$\gamma\ (10^{12}s^{-1})$
Ag	5.86	1.36	0.96	27.3
Au	5.90	1.37	0.99	40.8
Cu	8.47	1.64	1.49	52.4

The optical properties can also be described in terms of a complex refraction index $N = n + i\kappa$. Where n is the ordinary refraction index and κ is known as the extinction coefficient. The extinction coefficient is an optical function that determines the optical absorption of light through a medium

$$\kappa = \frac{\varepsilon_2}{2n} \quad (2.26)$$

Consequently, the absorption coefficient that determines how easily a light with a particular wavelength can penetrate through a medium is given by

$$\alpha_{(\omega)} = \frac{2\kappa_{(\omega)}\,\omega}{c} \quad (2.27)$$

In the range of low frequency, $\omega\tau \ll 1$, the field falls off inside the metal as $e^{-z/\delta}$, where δ is the skin depth, $\delta = \frac{2}{\alpha}$, while $\delta \gg l$ (l the mean free path of the electrons).

Experimental measurements are usually made in terms of transmittance, τ_λ, which is defined as $\tau_\lambda = I/I_0$ where I is the light intensity after passing through the sample, and I_0 is the initial light intensity. Subsequently, the absorption of light by a specimen (Figure 2.2) is given by

$$A = -log\,\tau = -log\,(I\,/\,Io) \quad (2.28)$$

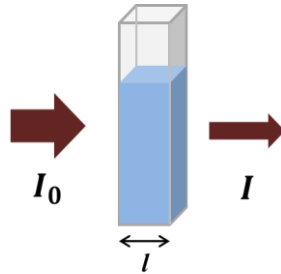which is known as the Beer-Lambert law.

Figure 2.2. Diagram of the Lambert-Beer Law of transmittance of a beam of light as it travels through a cuvette of width l (path length).

2.3.2 Plasmon modes in metal nanoparticles

The surface scattering in metal particles with big ratio of surface to volume, leads to additional collisions of the conduction electrons with an average rate $\gamma_{surface}$, proportional to the Fermi velocity, v_F, (about $1.4\times10^{-6}\,m/s$ in Au and Ag). The additional damping $\gamma_{surface}$ is given experimentally by [Kawabata and Kubo, 1966; Genzel and Kreibig, 1980]

$$\gamma_{surface} = A\frac{v_F}{L_{eff}} \quad (2.29)$$

where L_{eff} is the effective mean free path of free electrons that depends on the size and shape of nanoparticles and is obtained in terms of volume and surface area of the particle $L_{eff} = 4V/S$ [60], and A is an experimental parameter that represents the loss of coherence and depends on surface chemistry. Particularly, the values of A for silver are between 0.1 and 0.7 [Persson, 1993; Charle *et al.*, 1998].

As the diameter of a nanoparticle is in the range of the skin depth of the optical electromagnetic field in metals, particularly in silver the skin depth is 30 *nm*, the electromagnetic field can penetrate the particle. Consequently, the conduction electrons are shifted because of the field inside the particle, and negative charge and positive charge on opposite sides of the surface of the particle appear. As the result, a restoring force is created because of the attraction between different surface charges so the restoring force depends on the separation of the surface charges, in other words on the particle size as well as the polarizability of the medium. The strength of the restoring force determines the resonance frequency. The surface charges generate an oscillating dipole which radiates electromagnetic waves.

If the frequency of the electromagnetic field is in resonance with the frequency of this collective oscillation, very strong oscillation will appear. The amplitude of the oscillation and the width of the plasmon resonance depend only on the damping.

2.3.3 The scattering and absorption of light by prolate particles

The optical characteristics of absorbing and scattering of light in metal nanoparticles occur strongly at the plasmon resonance frequency. The ratio of scattering to absorption depends on the size of a particle and it increases with increasing the size of the particle. The extinction refers to combination of both processes of scattering and absorption. Frequency dependent cross-sections describe the characteristics of scattering, absorption, and extinction of particles, C_{sca}, C_{abs} and C_{ext}, respectively. Indeed, the scattering cross section C_{sca} multiplied by the incident energy flux gives the total power removed from the incident light because of the scattering of the incident radiation. Analogously, the absorption cross section multiplied by the incident energy flux gives the total power removed from the incident light because of the absorption of the incident radiation. Finally, the sum of the scattering and absorption cross section gives the extinction cross section.

The magnitude of the scattered light is given by

$$I(\omega) = \frac{I_0(\omega)}{A} C_{sca}(\omega) \quad (2.30)$$

where $I_0(\omega)/A$ refers to the intensity of incident light per area.

The absorption, scattering and extinction cross section of nanorods are calculated by Gans theory [61] are given by

$$C_{abs} = k \, Im(\alpha) \quad (2.31)$$

$$C_{sca} = \frac{k^4}{6\pi}(|\alpha|^2) \quad (2.32)$$

$$C_{ext} = k \, Im(\alpha) + \frac{k^4}{6\pi}(|\alpha|^2) \quad (2.33)$$

where $k = 2\pi \frac{\sqrt{\varepsilon_m}}{\lambda}$ is the wave vector and α is the polarizability for a single particle.

In recent years, there has been increasing interest in the study of the optical properties of nanowires because of the advantages of displaying transverse and longitudinal modes when electrons oscillate along the short and long axes of nanowires (Figure 2.3). The extension of the theory of light scattering by spherical particles to prolate particles characterized by three semi axes $(a > b = c)$, the polarizability along the axis x is given by [Bohren and Huffman, 1982]

$$\alpha_x = V \frac{\varepsilon_{(\omega)} - \varepsilon_m}{\varepsilon_m + L_x(\varepsilon_{(\omega)} - \varepsilon_m)} \quad (2.34)$$

where L_x is a depolarization factor and depends on the shape of the particles. The sum of L_x in three axes should be 1, therefore for spherical particle $L_x = \frac{1}{3}$ so the polarizability is highly dependent on both size and shape. The factor L_a for a prolate particle along its long axis is given by

$$L_a = \frac{1-e^2}{e^2}\left(-1 + \frac{1}{2e} ln \frac{1+e}{1-e}\right) \qquad e^2 = 1 - \frac{b^2}{a^2} \quad (2.35)$$

$\frac{a}{b}$ represents the aspect ratio of nanorod.

As it was mentioned in section 2.3.2, unlike the bulk that has dimensions very large compared to the mean free path of the free electrons, nanoparticles have dimensions that are so small and approach few times the mean free path. In this case, the free electrons experience extra dispersion from the surface of nanoparticles which causes an extra damping term [62] and the dielectric constant depends on the size.

In fact, the surface scattering does not effect on the location of the resonance position, however, it can increase the width and decrease the intensity of the resonance peak because of the coupling of the surface plasmon resonance modes with the external applied field.

A nanorod, unlike a spherical nanoparticle, has sufficient volume to scatter light efficiently so the radiation damping will be important for nanorods [61].

2.3.4 Shape dependent radiative properties

According to Gans theory, polarizability, and the surface plasmon resonance depend on size and shape of the nanoparticles. If symmetry of particles is broken and thus particles become more elongated along one axis the surface plasmon resonance will gain additional modes [51,63-65]. In other words, the plasmon resonance mode splits into two modes. In the case of nanorods two different surface plasmon modes exist: (1) longitudinal and (2) transverse. Figure 2.3 represents these two modes of nanorods.
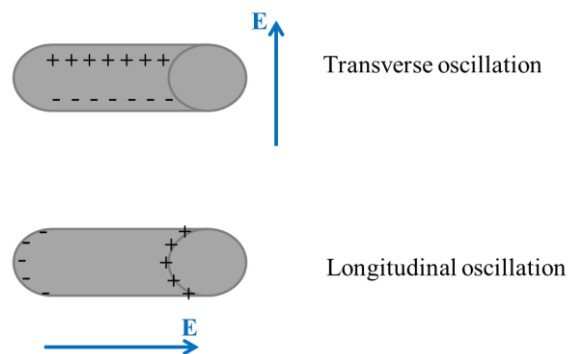

Figure2.3. Schematic representation the two surface plasmon resonance: transverse and longitudinal modes of nanorods. The plasmon resonance of nanorods splits into two modes: one longitudinal mode parallel to the long axis of the rod and a transverse mode perpendicular to the first.

By increasing the aspect ratio (ratio of length to diameter) increases, the energy separation between the resonance frequencies of the two plasmon bands increases [66,67]. The nanorod is easier polarized along its long axis because of low depolarizing factor so polarizing longitudinally occurs at a lower energy and thus higher wavelength. The longitudinal and transverse modes are sensitive to the aspect ratio (ratio of length to diameter) of the nanorods. For a fixed diameter, by changing the aspect ratio the position of both modes will be changed increasing the length of the changing the aspect ratio the position of both modes will be changed so in this case it is possible to tune and control the surface plasmon resonance [68].

2.4   Fundamentals of AAO electrochemistry

2.4.1 Self-ordered nanoporous anodic aluminum oxides

Among the methods for fabricating nanostructures, the membrane-base methods are promising candidates [69]. In particular, the anodic alumina membrane consisting of highly ordered hexagonal arrays of cylindrical and aligning pores perpendicular to the surface of substrate provides low cost processes to synthesize metallic nanowires with tunable diameter, space and length. Especially for magnetic nanowires [70,71], it is important to tune the magnetic properties (such as saturation magnetization, coercivity) of nanowires by controlling the diameter and the distance between the nanowires. In addition, this type of membranes has enough stability at high temperature (about 600°C) that is very useful for annealing the nanowires embedded in the membrane, and in organic solvents. Anodization of aluminum with highly ordered nanopore arrays consists of the anodic oxidation of a high purity Al electrode under well-controlled electrochemical conditions.

Generally, the anodization setups include the Al anode, an inert electrode as counter electrode, and an acidic electrolyte while the required voltage for anodization is supported by a direct current (*DC*) power supply. During the process of anodization, an external thermostat often controls the temperature. The arrangement, shape and size of alumina pores depend on the applied voltage, type, and concentration of the electrolyte as well as temperature. The aim is to anodize the aluminum as hexagonally arranged arrays with circular pores with tunable diameter of pores and interpore distance.

The main chemical reaction during the process of anodization is the oxidation of Al and the evolution of hydrogen gas

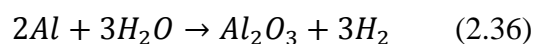$$2Al + 3H_2O \rightarrow Al_2O_3 + 3H_2 \qquad (2.36)$$

Figure 2.4 presents the schematic of the anodization process and the formation of pores in an acidic electrolyte. During the process of anodization there is a balance between the oxide dissolution at the interface of electrolyte/Al_2O_3 and the formation of oxide at the Al_2O_3 /metal interface that keeps the thickness of the barrier layer constant [69,72].

The thickness of this non-conductive barrier layer that is between the bottom of the pores and the aluminum, depends on the anodic potential. It is given by $t_{BL} = \alpha V$ where α refers to the ratio of anodization and typically its value is between *1.2 nm/V* and *1.4 nm/V* [72]. Indeed,

sufficient strength of the electric field across the barrier layer is required for penetrating ions of the electrolyte through it. By increasing the thickness of the oxide layer the strength of the field across it decreases which leads to discontinue the penetrating of ions. Consequently, the thickness of the barrier layer at this point remains constant.

On the other hand, a self-assembled nanoporous alumina layer grows on top of the barrier layer and the depth of the pores depends on the duration of anodization. Anodic alumina membranes have been fabricated in a variety of acidic electrolytes includes sulphoric, oxalic and phosphoric acids [73,74].
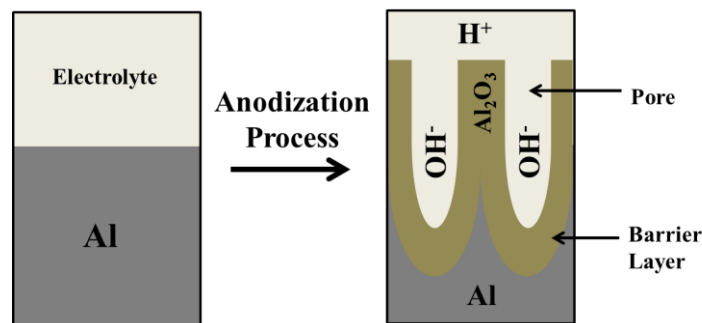

Figure 2.4. Schematic of anodization process to form pores in an acidic electrolyte.

The different stages of pore development are described with respect to the current transients recorded during the potentiostatic anodization process [75]. In the first stage of the process, a barrier layer forms on the surface of the aluminum surface that decreases the anodic current density suddenly.

On the surface of the oxide (at the interface of oxide and electrolyte) pores nucleate in random positions. The reason for nucleation of pores in such self-assembled process is the difference of the volume expansion between the aluminum and the alumina which leads to mechanical stress in the barrier layer [76]. In fact, the volume expansion that was determined by Nielsch et al. [77] is a crucial factor to improve the regularity of the pores in which the best ordered periodic nanoporous will be obtained if the volume expansion coefficient is about 1.2 [78]. The volume expansion is independent of the electrolyte, and it creates the repulsive forces between the neighboring pores at the metal/Al_2O_3 interface to enhance the formation of ordered hexagonal pore growth. In addition, Jessensky et al. [79] determined that the mechanical stress for a certain value of the volume expansion is adequate to promote ordered pores.

After nucleation of pores, the electric field is stronger at the bottom of the pores which increases the rate of oxidation and dissolution. As the result, in this stage the anodic current density increases. Finally, after a slight decrease of the current density, it reaches a constant

value which represents a steady-state equilibrium between the oxidation and dissolution of alumina. At this balance point, the thickness and geometry of the barrier layer remains constant, while the pores form and grow. Figure 2.5 shows an SEM image of porous alumina with highly ordered arrays anodized in oxalic acid. The walls between pores consist of a dark inner layer and bright outer layer. This different contrast in SEM image is explained by Thompson et al [79]. The pore diameter (D_p) mainly depends on the pH value of the electrolyte, while the interpore distance (D_{int}) is determined by the applied field [77] and their relation by the phenomenological expression [75]

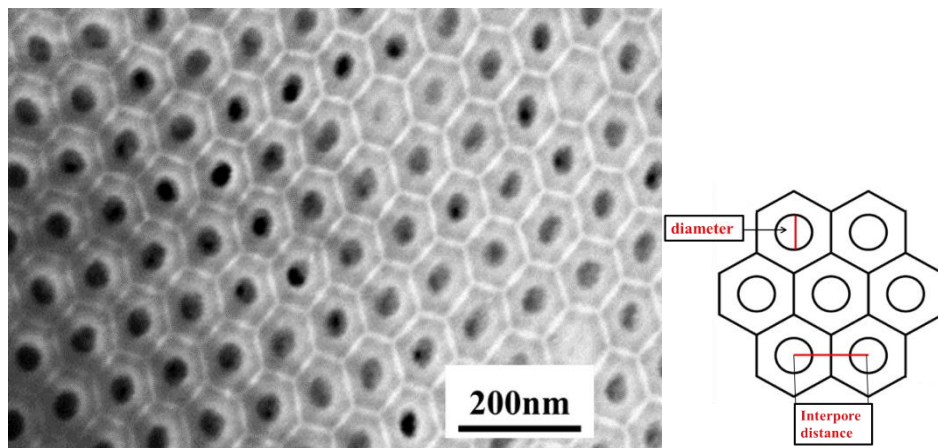$$D_{int} = D_p + 2 \propto V \qquad (2.37)$$

Figure 2.5. SEM image of the top side of an anodic alumina membrane with highly ordered hexagonal nanopore arrays with 35 nm diameter. Schematic representation of the pore diameter and interpore distance of the top view of the membrane.

To improve the process of fabricating alumina with highly ordered pore arrays Masuda et al. [73] suggested a two-step process of anodization. In brief, a high purity aluminum foil (99.999% purity) is used for fabricating nano-pourous alumina and prior to anodization it is cleaned and electropolished. The anodization process is performed under optimized conditions (Table 2.2) for a long time usually for 24 h. Then, the disordered first alumina is removed by using the method of wet chemical etching from the Al foil, so that an ordered concave pattern on the surface of the Al foil appears. This pattern plays as an ordered mask for the next step of anodization in which the nucleation and growing of the pores begins from these regular points. Subsequently, the second anodization is performed with the same conditions applied for the first step of anodization. The thickness of the membrane depends on the duration of the anodization and depths of 40 μm and 100 μm.

In this PhD work, the membranes were fabricated by using oxalic acid as electrolyte at 40 *V* to fabricate nanoporous anodic alumina membrane, with the pore diameter range between 35-75 *nm*.

TABLE 2.2. Typical Parameters applied for anodization and the structure properties of self-ordered nanoporous alumina membrane [Vazquez 2015, Nielsch 1998].

Electrolyte	Anodic Voltage	Temperature (°C)	Pore diameter $D_P(nm)$	Interpore distance $D_{int}(nm)$
0.3 M H_2SO_4	25 V	1	25	65
0.3 M $(COOH)_2$	40 V	3	35	105
0.1 M H_3PO_4	195 V	1	220	490

2.5 Fundamentals of Electrodeposition

During the past two decades, nanoporous anodic alumina membranes have been widely used for synthesizing metallic nanowires by growing them into the nanopores. Among several methods applied for filling the nanopores, such as atomic layer deposition (ALD), chemical vapor deposition (CVD), sol-gel techniques and electrochemical deposition, the electrochemical deposition is a promising method to synthesize nanowires with tunable aspect ratio and complete filling of the pores [80].

In the process of the electrodeposition, the deposition of a metal from a solution of its reagents will occur. In the simplest model of the electrochemical cell two electrodes are used which are so-called counter electrode and working electrode. The counter electrode acts as the anodic electrode where the oxidation takes place while, the working electrode acts as the cathodic electrode where the reduction takes place and is coated by the metallic deposit. These electrodes are immersed inside the electrolyte so they are separated by the ionic conductor. Typically, a reference electrode with a stable and certain electrode potential is required to apply in the cell of the electrodeposition. The reference electrode is not involved in the reaction during the electrodeposition but provides the control of the electrical conditions to make the electrodeposition process more stable.
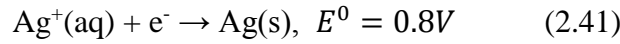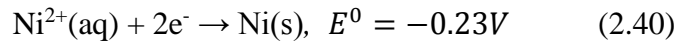
During the process of the electrodeposition there is an equilibrium of the aqueous solution

$$M^{n+} + ne^- \rightleftharpoons M + E \qquad (2.38)$$
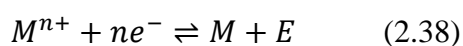
where E is the reduction potential of the cell. E is estimated by using the Nernst equation

$$E = E^0 + \frac{RT}{nF} \ln \frac{[M^{n+}]}{[M]} \qquad (2.39)$$

R is the ideal gas constant ($R=8.314$ J/Kmol), T the absolute temperature, F the Faraday constant ($F = 9.648\ 533\ 99(24) \times 10^4\ C\ mol^{-1}$), n the number of electrons in the reaction, $[M^{n+}]$ and $[M]$ are the molar concentration of the reagents and products, respectively. E^0 is the standard reduction potential that shows the tendency of chemical species for reduction and is measured in volt. The standard reduction potentials in aqueous solution at 25^oC for $Ni^{2+}_{(aq)}/Ni_{(s)}$ and $Ag^+_{(aq)}/Ag_{(s)}$ are -0.23V and 0.8V, respectively, referred to $2H^+_{(aq)}/H_{2(g)}$ as reference.

$$Ni^{2+}(aq) + 2e^- \rightarrow Ni(s), \quad E^0 = -0.23V \qquad (2.40)$$

$$Ag^+(aq) + e^- \rightarrow Ag(s), \quad E^0 = 0.8V \qquad (2.41)$$

In fact, the process of electrodeposition should be supplied with enough energy for starting the growth process.

By using Faraday's laws the mass, m, of the deposited material is estimated

$$m = \frac{M}{neN_A} \int_0^t I dt \qquad (2.42)$$

I is the current intensity, t the time of deposition, M the molar mass, n the valence of the deposited ion and N_A the Avogadro's constant ($N_A = 6.02214129 \times 10^{23}$ mol^{-1}). Note, the current efficiency (η) for each metal is less than 100% because of H_2 evolution. For Ni corresponding to the reaction conditions it is about 86% [80].

To control the length of nanowires during the process of electrodeposition, first the mass of the nanowires with desired length should be estimated by using the formula of density ($m = \frac{\rho}{V}$).

Respecting to the diameter of nanopores, the porosity and the area of the membrane as well as the desired length for the nanowires, the total volume of the nanowires is calculated. Then, by using the formula of density the mass of nanowires with desired length is estimated. Subsequently, by considering the Faraday's law the amount of charges that should pass through the working electrode is estimated for depositing material with a certain mass. In this case, for controlling the length of nanowires and obtaining the desired length of the nanowires, in other

words the desired aspect ratio, monitoring the charge during the process of the electrodeposition is essential.

For synthesizing nanowires inside the membrane, the electrodeposition temperature and *pH* value of the electrolyte are two of the most important parameters that influence the electrodeposition. The temperature of the electrolyte affects the diffusion velocity of the ions. The electrolyte with low *pH* value leads to higher evolution of H_2 that may prevent depositing the material into the pores. In addition, in an acidic solution the membrane of anodic alumina may be destroyed. On the other hand, the electrolyte with high *pH* value increases the OH^- ions concentration around the metallic ions which make it difficult for them to deposit [81].

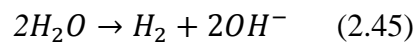In general, the main reactions that take place during the electrodeposition are:

1. The metal ions M^{z+} in aqueous solution are reduced at the cathode (working electrode)

$$M^{z+} + ze^- \rightarrow M \quad (2.43)$$
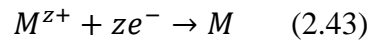
2. The reduction of hydrogen ions into gaseous H_2

$$2H^+ + 2e^- \rightarrow H_2 \quad (2.44)$$
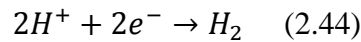
3. The generation of OH^- ions at the cathode

$$2H_2O \rightarrow H_2 + 2OH^- \quad (2.45)$$

4. Subsequently, the reaction of M^{z+}ions with the OH^-ions leads to the generation of metal hydroxides

$$M^{z+} + OH^- \rightarrow MOH^{z+-1} \quad (2.46)$$

5. The reduction of metal occurs following a *z* steps reaction

$$MOH^{z+-1} + (z+-1)e^- \rightarrow MOH \quad (2.47)$$

$$MOH + e^- \rightarrow M + OH^- \quad (2.48)$$
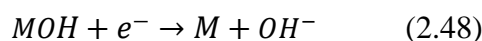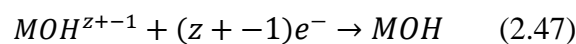
The growth mechanism of the electrodeposition inside the membrane is complex and it is not completely clear and any explanation about it is speculative. It can include: (1) The formation of isolated nuclei; (2) Coalescence of some isolated clusters to form an elongated

crystallite, (3) Formation the linked network structure to cover the surface; (4) A continuous deposit containing vacancy.

In the template-assisted method of electrodeposition there are different modes of applying the electrical field to the electrochemical cell. Two distinct electrodeposition methods are:

1. The *galvanostatic mode* implies a constant current (*DC*) during the process of electrodeposition between the working electrode and the counter electrode. It is not common for synthesizing nanowires as the potential of the deposition isn't constant during the electrodeposition. Therefore, it will influence on the properties and composition of the deposits. However, in comparison with the potentiostatic mode explained in the following, this mode can lead to a better control of the amount of the material on the working electrode because of the constant growth rate.

2. The *potentiostatic mode* is the most common approach for electrodeposition at the laboratory scale. In this method, the reference electrode is applied to measure the working electrode's potential and is kept constant by using a potentiostat. In addition, during the electrodeposition the cathodic current density is monitored. Using this mode of electrodeposition is useful to optimize the conditions of the deposition.

Among different methods of electrodeposition in potentiostatic mode 1) Direct current (*DC*) [71, 80]; 2) Alternating current (*AC*) [82]; and 3) Pulsed electrodeposition [83,84], *DC* electrodeposition, a constant potential is applied during the deposition, is a promise method to enhance the rate of deposition [80] and optimizing control of the composition and crystallinity of the nanowires [85].

To fill the pores of the membrane during a potentiostatic or galvanostatic process, an electrical contact at one side of the membrane is required to provide the electrochemical reduction of electrolyte cations. For achieving it, Figure 2.5 shows the different steps in which the non-conductive barrier layer at the bottom of the pores should be removed either by wet chemical etching, ion etching, or other electrochemical approaches [75]. Prior to removing the barrier layer, the membrane should be released from the rest of the aluminum explained in detail in section 3.1.2. For the next step, one side of the free-standing membrane is coated by depositing a metal have an electrical contact as working electrode. Among the metals gold, silver and copper are typically evaporated on the surface of the membrane because removing them after the end of the process is easy [86].

3 Experimental techniques: synthesis and characterization

In this chapter, the details of the experimental procedures used for this PhD work is explained. The two-steps of fabricating anodic aluminum oxide (AAO) membranes followed by preparation the membranes for synthesizing the nanowires using a new method for optimizing the pore diameter is described. Subsequently, a general overview of synthesizing the nanowires using the membrane combined with the electrodeposition method and preparing the samples for characterization are explained. Finally, briefly description of the overall characterization techniques employed to obtain the results presented in this thesis is given. Scanning electron microscopy (SEM) and transmission electron microscopy (TEM) are employed for the morphological characterizations as well as the energy dispersive X-ray (EDX) spectroscopy was used to determine the chemical composition analysis of the nanowires. The magnetic properties are characterized using superconducting quantum interface device (SQUID) magnetometry and ferromagnetic resonance (FMR). Finally, UV/VIS-Spectrometry is employed for optical characterization.

3.1 Synthesis method

Magnetic nanowires have been synthesized by electrodeposition on the corresponding magnetic materials in anodic aluminum oxide (AAO) membranes. In the following, two-step anodization process of an aluminum foil and the synthesis of the nanowires are discussed.

3.1.1 Preparation of AAO membranes

Highly pure aluminum foils (99.999%) of 0.5 *mm* thickness and 21 *mm* diameter are used for fabricating anodic aluminum oxide (AAO) membranes by a two-step anodization

technique. Prior to anodization the process of pre-treatment is performed including 2 steps: cleaning the samples and electropolishing. The Al foils are cleaned with ethanol under sonification for 10 minutes. Subsequently, the foils are electropolished using an electrolyte solution with a ratio of 1:7 of perchloric acid in pure ethanol by applying a voltage 30 *V* for 3 min at 2°C [6] to create a smooth surface.

After the process of pre-treatment, the foils are anodized in 0.3 *M* oxalic acid solution at 4ºC under an applied potential of *40 V*. Figure 3.1 (a) shows a schematic representation of the home-made anodization cell. This system consists of a polyvinylchlorid (PVC) cylindrical container working as a thermal insulator to keep the temperature constant. The Al foils (previously electropolished) are pressed with an O-ring on the bottom of the cell to prevent of any leak. Then an Al plate is fixed on the bottom side of this set up and it works as positive electrical contact (anode) and cooling plate simultaneously. A refrigeration circuit is used to cool the Al plate. A chemical inert Pt wire acts as the cathode and is placed ~ 20 *mm* away from the sample. During the process of anodization, a mechanical stirrer is used to keep constant the homogeneity of the electrolyte and temperature. A *DC* voltage is applied between the anode and the cathode to anodize the aluminum foil. Figure 3.1 (b) shows the top view of the home-made anodization and electrodeposition cell. The circular holes with diameter 9 *mm* show the sample positions and illustrate to carry out such process for four samples simultaneously. However, the number of the holes can be varied by covering them using PVC cylinder. The Pt wire with *1 mm* diameter and a length of *60 cm* seen as a zig-zag structure is used as counter electrode. In fact, the surface area of the counter electrode should be big enough to ensure that the reaction at this electrode can take place fast so as not to limit the reaction at the working electrode.
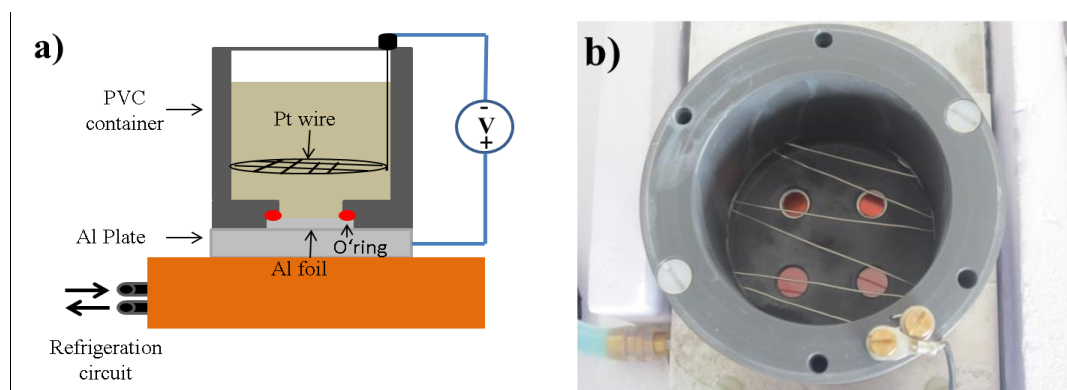
Figure 3.1. a) Schematic representation of the set-up for the process of anodization and electrodeposition. The aluminum foil is placed at the bottom of the cell in contact with an aluminum plate that act as working electrode. A Pt wire is placed above the sample and acts as a counter electrode. b) Top view image of anodization and electrodeposition set-up. The circular holes are the sample positions and illustrate to carry out such process for four samples simultaneously. The number of the holes can be varied by covering them using PVC cylinder.

The process of anodization under constant applied potential of 40 *V* (*DC*) is monitored, measuring the current (Figure 3.2). The first anodization process lasted 24 *h* to enhance the regularity of the pores. As in details described in section 2.4.1, the current drops because of the formation of the barrier layer at the surface (stage 1) and it passes through a minimum value illustrates that the thickness of the barrier layer is reaching to its maximum. In the second stage, increasing the current indicates the nucleation of the pores in the random positions of the oxide due to the difference of the volume expansion of the aluminum and the alumina leads to local electric field distribution at the fluctuations of the oxide surface. Finally, in stage 3 the current reaches to a stable level which corresponds to the continued growth of the pores.

Then, the first anodized layer is removed under a wet chemical etching process. The anodized foils are immersed in a solution composed of phosphoric acid (6%) and chromic acid (1.8%) at 60 °C for 12 *h* so-called orange solution [87,88] to get the mask for the second anodization step for 20 *h*. The thickness of membrane depends on the time of the second anodization process. The thickness of the membrane is estimated respecting to the rate of about 2 *μm/h* [89] so after 20 *h* the thickness of the membrane is estimated about 40 *μm*.
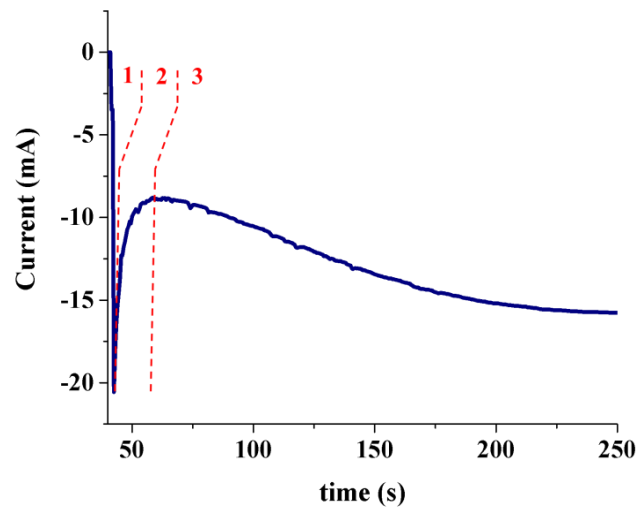
Figure 3.2. Behavior of the current during the anodization process. The illustrations show the different stages of the formation of the barrier layer and the pore growth. In stage 1, dropping the current indicates the formation of non-conductive layer (barrier layer). Then, in stage 2, increasing the current indicates the nucleation of the pores in random positions of the oxide. Finally, in stage 3 the current reaches to a stable level corresponding to the growth of the pores.

Figure 3.3 (a) and (b) shows the SEM images of top view and cross section of a membrane, respectively. It represents highly ordered hexagonal self-assembled nanopore arrays with pore diameter of 35 *nm* and interpore distance of 105 *nm* under these conditions. The properties of the membrane such as the pore size distribution and the surface roughness of the pores influence on the properties of the synthesized nanowires [90].
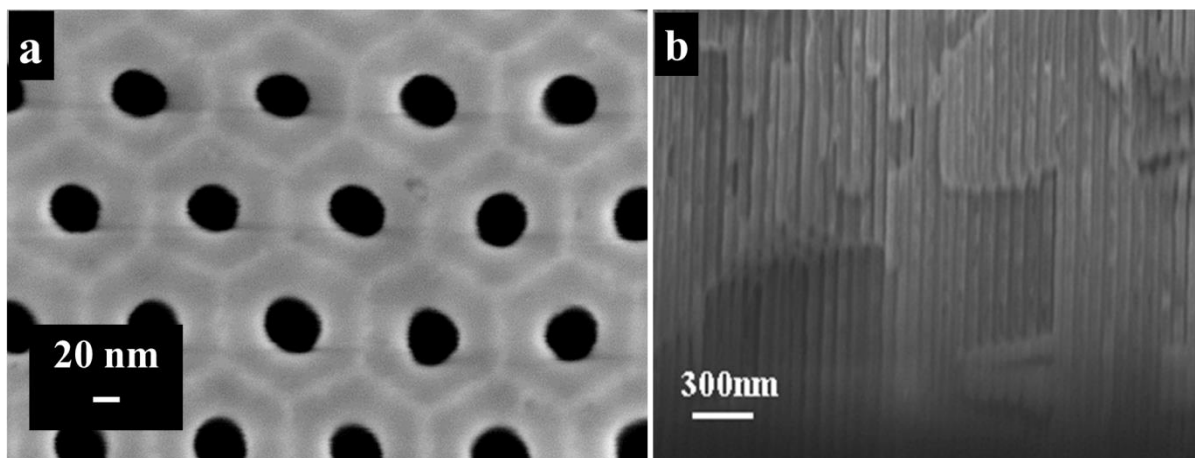

Figure 3.3. SEM images of a) top view and b) cross section of the membrane represents highly ordered hexagonal nanopore arrays after the second step of anodization.

The diameter of pores can be tuned between 35 *nm* to 85 *nm* by using chemical etching processes.

3.1.2 Optimization of pore diameter

Since in section 2.4.1 is explained the preparation process of the AAO membrane for synthesizing nanowires by using *DC* electrodeposition, the non-conductive layer at the bottom of the pores (Figure 2.3) should be removed. In this case, the rest of the aluminum is removed in a solution of $CuCl_2$ and HCl. Figure 3.4 shows the SEM image of convex shape of barrier layer in back side of the membrane revealed after removing the rest of Al.
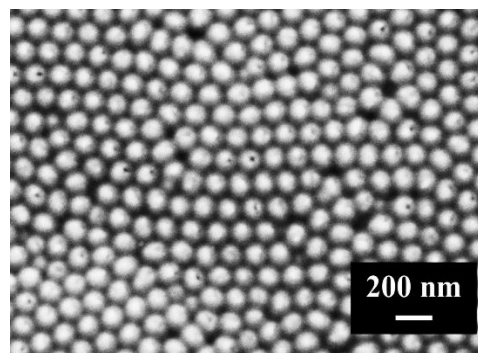

Figure 3.4. Shows SEM image of back-side of the membrane after removing the rest of Al to reveal the convex shape of barrier layer.

Figure 3.5 represents the schematic of removing barrier layer. The revealed barrier layer at the bottom of the pores is chemically etched in 5 wt% H_3PO_4 at 30 ℃ [73]. In addition, during the process of removing the barrier layer the pores are enlarged simultaneously. This process is so called pore-widening in which the diameter of the pores depends on the time of the etching process (Figure 3.6).

Figure 3.5. Represents the schematic of removal of remaining aluminum and barrier layer. During this process the pores diameter are widened.
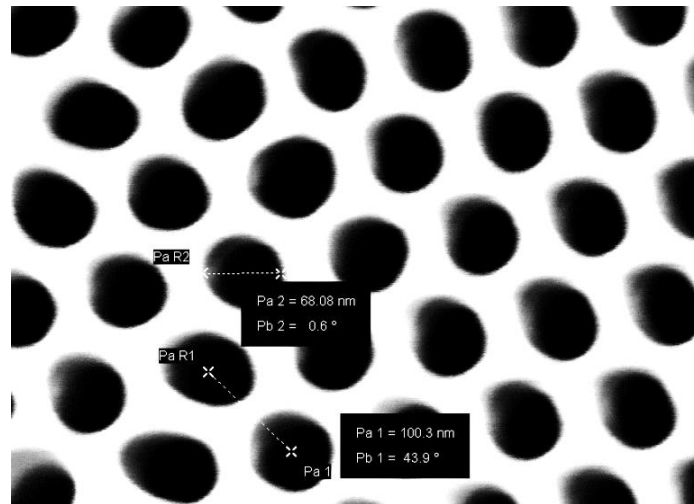
Figure 3.6. Shows SEM image of top side of the membrane after pore widening process for 45 *min* by 5 wt.% H_3PO_4. The pore diameter is about 70 *nm*.

During this process, the whole sample is immersed in a phosphoric acid solution, which causes to remove the barrier layer but also enlarge the pore diameter simultaneously (Figure 3.7).
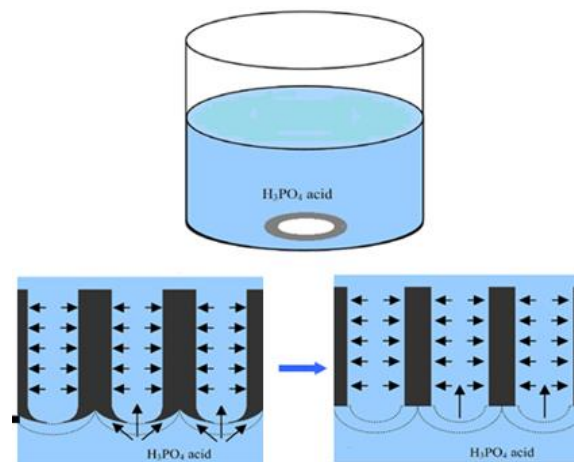

Figure 3.7. Schematic illustration of the method for removing barrier layer and pore widening of the anodic alumina membrane [91].

Therefore, there is a challenge of obtaining small pore diameters. To precise control on the pore-widening process for achieving small pore diameter, one cell is designed and fabricated (Figure 3.8). The backside of the membrane is in contact with phosphoric acid while the top side is in contact with pure water to avoid of pore widening process. Two electrodes are placed very close to each other and below the membrane inside the distilled water and they are connected to a home-made *AC* generator for polarization of water. When the barrier layer is

removed, the ions of phosphoric acid go through the pores and reach the electrodes. A digital multimeter switched in *AC* current mode with very high resolution (*nA*) is applied to show very slight change in current to reveal that the barrier layer is removed. A mechanical stirrer was used inside the phosphoric acid to provide homogenous solution.
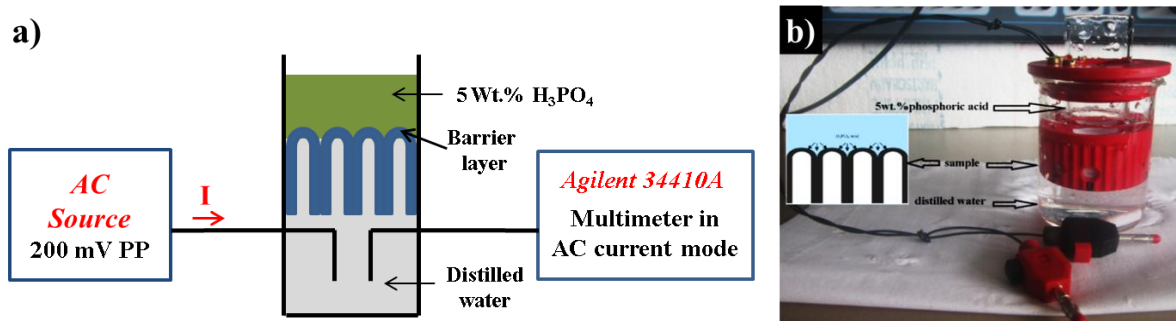

Figure 3.8. (a) Schematic of the setup for removing the barrier layer on backside of the membrane with high control on pore-widening process. (b) The cell.

It was observed that there is a direct relation between current, time and diameter of the pores during the process of removing barrier layer and pore-widening. Table 3.1 summarizes the results of this study.

Table 3.1. Relation between the current, time and obtained diameter of the pores during the process of removing barrier layer for membranes with initial diameter 35*nm* and length of 30*μm*.

Diameter	35 nm	40 nm
Time (min)	38	48
Current (nA)	335	1590

3.1.3 Synthesis of nanowires by electrodeposition method

After preparing the membrane and removing the barrier layer a continuous layer of Au (300 *nm* thick) is thermally evaporated on the backside of the membrane. This layer is used as working electrode that is responsible for electrodepositing materials inside the pores of the membrane. Prior to deposit gold layer on the surface of the membrane, the sample was put inside an oven at 80 ℃ for 20 *min* to completely remove bubbles and water inside the pores of the membrane.

During the depositing of the gold layer, shadow effect is used by putting the samples not directly below the target and by changing the position of the samples. Figure 3.9 shows the

SEM images of the backside of the membrane with pore diameter 45(±5) nm after depositing Au layer with a thickness of 150 *nm* (a) and 250 *nm* (b). It is seen that even by depositing 250 *nm* of gold layer the pores are not completely covered. To block the pores completely and prevent the so-called pudding effect (that causes one tip of the nanowire to have a mushroom shape) a layer of sacrificial metal is deposited. Afterwards, after the deposition process, the Au and the sacrificial layers are dissolved. In the case of the synthesis of Ag nanowires, Ni is used as a sacrificial layer.
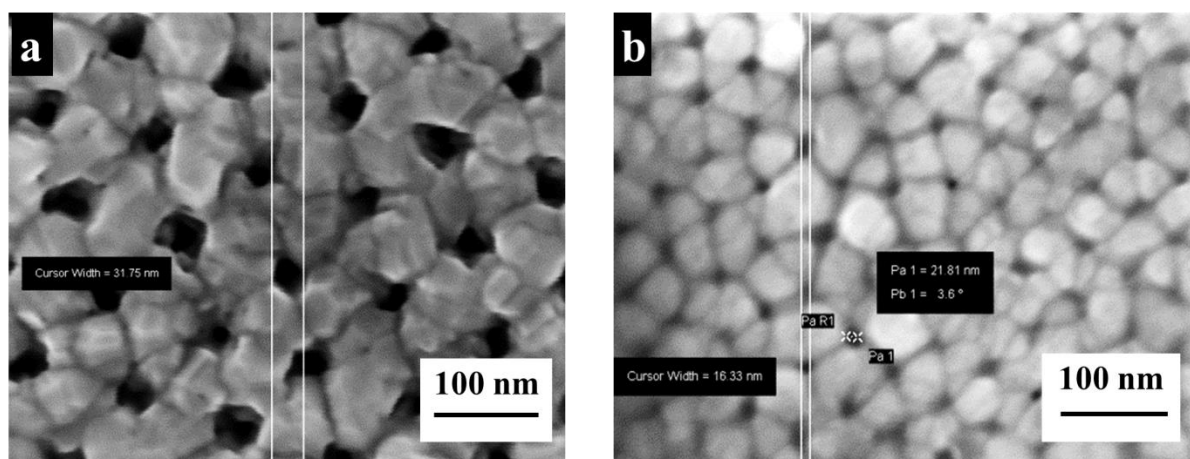

Figure 3.9. SEM images of the backside of the membrane after depositing Au layer a) 150nm and b) 250nm, respectively.

Figure 3.10 illustrates the schematic of a conventional three-electrode electrodeposition cell. The deposited material fills the pores of the membrane to form the nanowires. The detail is described in section 2.5. For the process of electrodeposition, a potentiostat Amel 2049 is used to apply a *DC* potential under potentiostatic mode. In these experiments, Ni and Ag nanowires are synthesized inside the membranes.
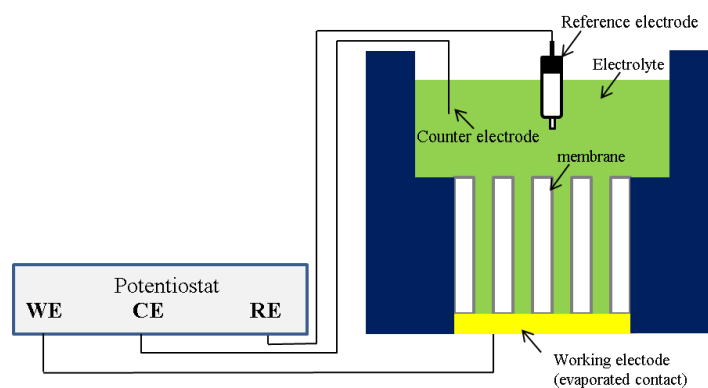

Figure 3.10. Schematic illustration of a conventional three-electrode cell for electrochemical deposition of nanowires inside the AAO membrane (WE: working electrode; CE: counter electrode; RE: reference electrode).

Figure 3.11 demonstrates a typical current-time curve recorded during the process of potentiostatic metal deposition inside the AAO membrane. After an initial transient, the current-time curve exhibits a nearly steady-state regime of electrodeposition, which corresponds to Ag growth inside the AAO membrane [92,93].
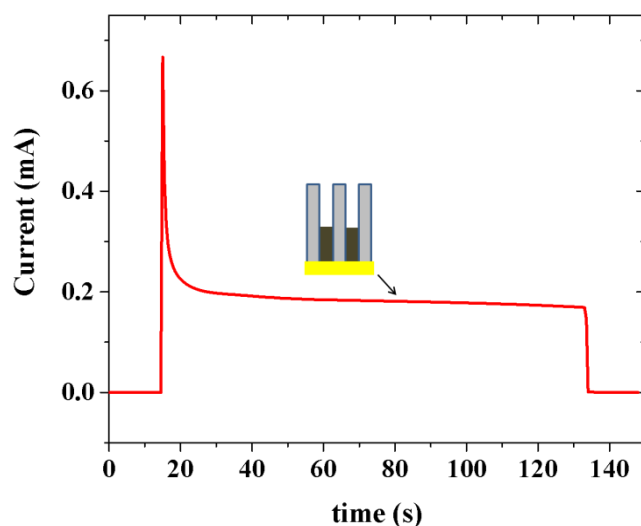

Figure 3.11. The current-time transient curve for deposition of 200 *nm* diameter Ag nanowires in a membrane with pore diameter 75 *nm*, interwire distance 105 *nm*, thickness 40 *μm* and pore density $1\times10^{13}/cm^2$.

Figure 3.12 shows a) the AAO membrane surrounded by aluminum with diameter 9 *mm*, thickness 40 *μm* pore diameter 75 *nm* and pore density of $1\times10^{13}/cm^2$. Ag nanowires are synthesized inside the membrane and b) the released Ag nanowires with the length of nearly 400 *nm* and diameter 75 *nm* after removing the membrane.
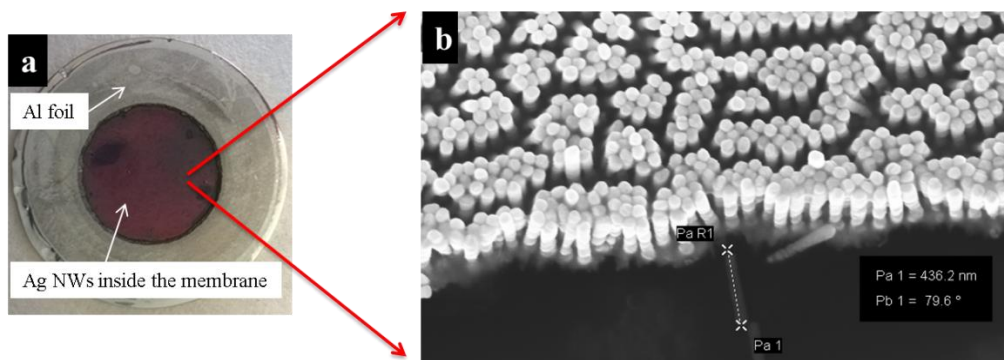

Figure 3.12. a) The synthesized Ag nanowires inside a membrane with pore diameter 75 *nm*, thickness 40 *μm* and pore density of $1\times10^{13}/cm^2$.   b) SEM image of Ag nanowires on Si substrate with diameter 75 *nm,* and the length of around 400 *nm* after removing the membrane.

3.1.4 Synthesis of multisegmented Ni-Ag nanowires

There are two main ways for synthesizing segmented nanowires by using electrodeposition [94]. The first strategy is to use one electrolyte bath containing all precursors of the desired metals by using the method of pulse electrodeposition [95].

The second strategy is to synthesis by sequential electrodeposition using alternating bath of metal ions [96]. In this case, one metal is synthesized in its bath and then the bath is exchanged with the other electrolyte. By this strategy, *DC* electrodeposition is possible. Despite of the being a time-consuming method, the main advantage is to prevent the trace of the different metal inside the other segments, what also leads to a sharp interface between the segments.

3.1.5 Sample preparation for characterization

To prepare samples for measuring magnetic properties, first the layer of the Au on the backside of the sample is removed by using the solution of *KI* and *I₂*. Then the sample (consisting of nanowires embedded inside the membrane) is adhered on a cleaned Si substrate ($5 \times 5\ mm^2$) by using G-varnish, which does not have a significant signal on the measured magnetic properties of nanowires.

For characterizing the morphology and structure of nanowires, the Au layer is also removed as described above and the membrane is dissolved using wet etching process. The resulting nanowires are redispersed in distilled water and the solution is stirred by ultrasonic bath to separate the agglomerated nanowires. The nanowires are finally redispered into ethanol.

Releasing nanowires and collecting them is one of the major challenges especially for short length nanowires. Here very briefly the problems of releasing nanowires will be described and subsequently, the improvement of such process will be shown.

To etch the Al_2O_3 membrane there are several options [97]: 1) using the orange solution (6 wt.% H_3PO_4 + 1.8 wt.% H_2CrO_4), 2) using a basic solution (3 *M* NaOH) and 3) using acidic solution (6wt% H_3PO_4) (Table 3.2). NaOH is used to remove the membrane because phosphoric acid is one of the etchants of Ni. Indeed, NaOH is not a good etching of alumina as it produces non-soluble aluminum hydroxide, but it is a very effective etchant for alumina dissolution.

TABLE 3.2. Summary of the etchants of the used materials.

Material	Etchants
H_3PO_4	Ni and Ag
HNO_3	Ni and Ag
NaOH	-

To release the nanowires from the membrane, a piece of the sample is dissolved with 1 *M* NaOH solution 3 h. Afterwards, the acidic solution is removed and exchanged with water. The sample is washed 6 times with distilled water and the nanowires are precipitated by centrifugation (10000 *rpm*, 5*min*). Finally, the nanowires are redispersed in water.

Figure 3.13 shows an SEM image of released Ni nanowires synthesized with length of 300 (± 50) *nm*. According to this image there is a contamination around nanowires and some nanowires are broken or damaged during the releasing process.
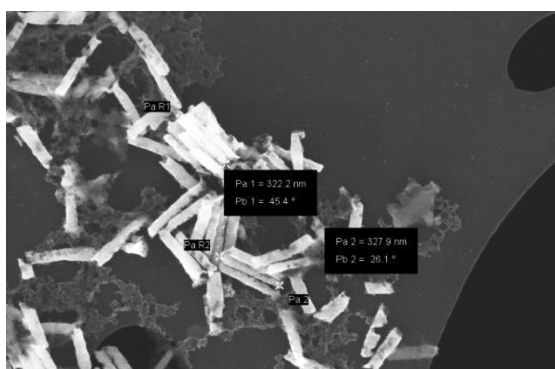

Figure 3.13. SEM image of released Ni nanowires with NaOH solution on a TEM grid.

As already mentioned, this contamination is a side-product of the reaction between the AAO membrane and the NaOH solution that produces aluminum hydroxide. This product is like a gel and it traps very short nanowires, as shown in Figure 3.14 (a) and (b). In addition, upon dissolution of the membrane a significant number of the nanowires agglomerate (Figure 3.14 (c)). Figure 3.14 (d) shows SEM image of released Ni nanowires after dispersing on the Si substrate that indicates the improvement of releasing and dispersing the nanowires.

After improving this process for releasing the nanowires without contamination and dispersing them with less agglomeration, releasing nanowires even with short length is

performed successfully. Figure 3.15 shows an SEM image of dispersed Ni nanowires with diameter 80 (±5) *nm* and the length of 250 (±30) *nm* on Si substrate.
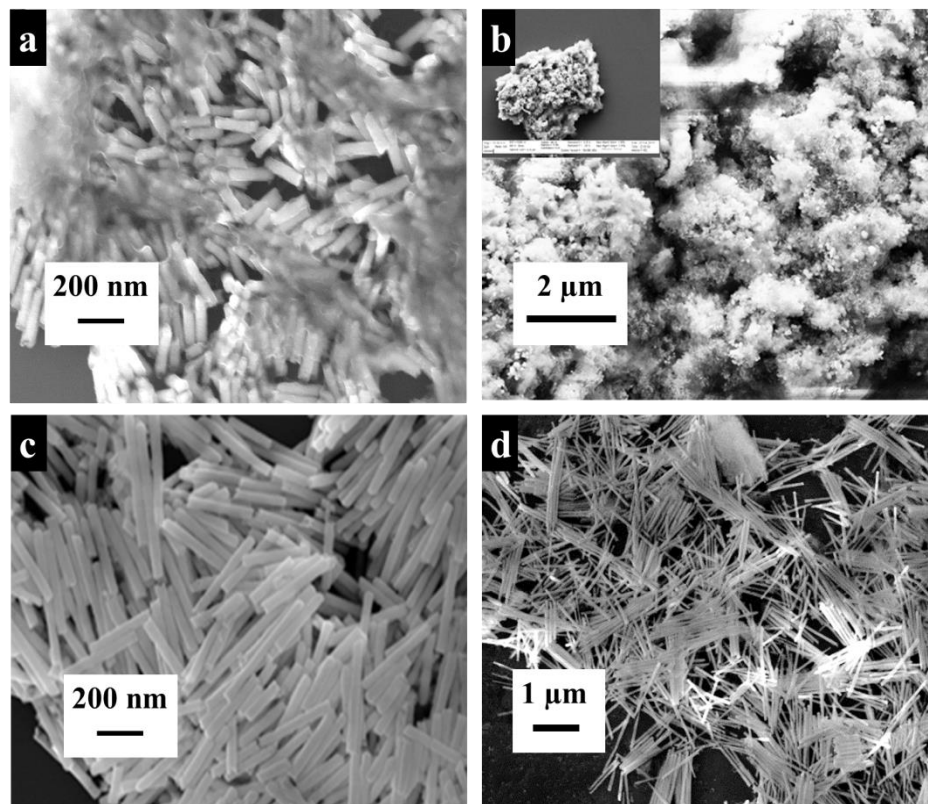
Figure 3.14. (a) and (b) SEM images of trapped Ni nanowires in non-soluble Al(OH)$_3$ after dissolving the membrane in NaOH. (c) SEM images of released Ni nanowires on Si substrate, forming an agglomeration due to interactions. (d) SEM image of released Ni nanowires presented the improvement of releasing and dispersing nanowires.
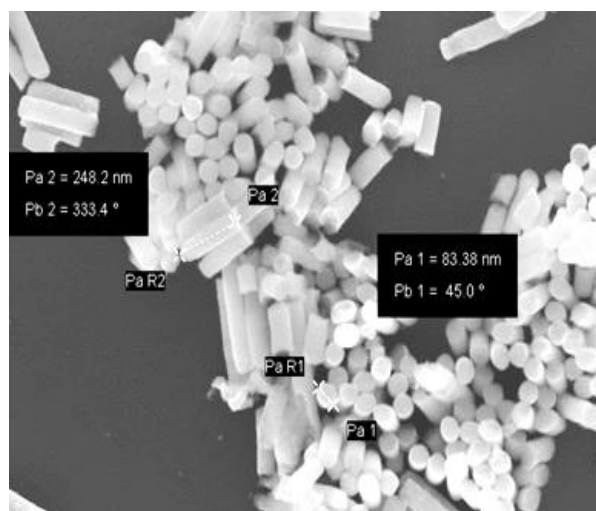

Figure 3.15. SEM image of dispersed Ni nanowires with short length of 250 *nm* on Si substrate.

The releasing process of multisegmented nanowires (with two or three segments) is more complicate because during the process of releasing and dispersing the nanowires in solution they break at the interface of the segments. Figure 3.16 presents the SEM image of released three-segmented Ag/Ni on Si substrate that clearly reveals that some segments are separated. The length of each segment is around 500 *nm* and Ni and Ag segments of the nanowires are identified by their light and dark contrast, respectively.
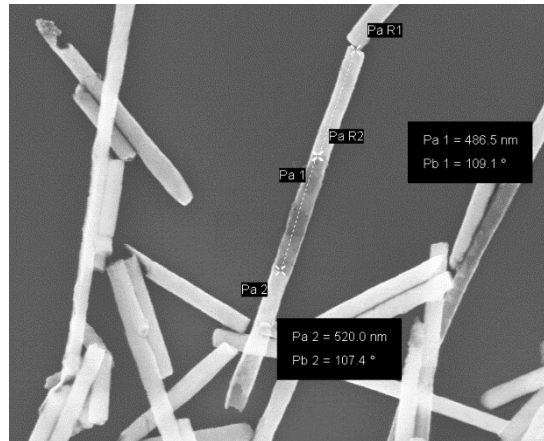
Figure 3.16. SEM image of released three-segment Ni and Ag nanowires on Si substrate. The length of each segment is 500 (±50) *nm* and Ni and Ag segments of the nanowires are identified by their light and dark contrast, respectively.

For such nanowires ultrasound is used just for a short time to disperse the nanowires because it caused to break the interface of the segments. The rest of the releasing process is carried out as previously described. Figure 3.17 shows the improvement for dispersing the Ni-Ag-Ni nanowires on Si substrate.

Figure 3.17. SEM image of released hybrids of Ni-Ag-Ni nanowires and Ni and Ag segments of the nanowires are identified by their light and dark contrast, respectively.

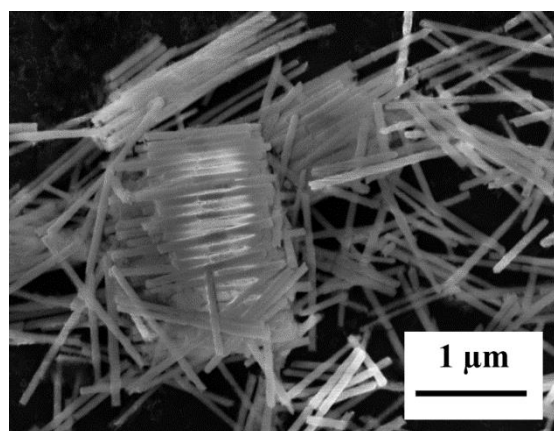To characterize the optical properties of hybrid segmented Ni-Ag nanowires the nanowires are kept in ethanol because ethanol does not influence the optical properties measurements of the nanowires.

3.2 Characterization techniques

Several techniques have been used to characterize the chemical composition as well as the magnetic properties of the synthesized nanowires.

Transmission electron microscopy (TEM) has been used to characterize the morphology, crystalline structure, and chemical composition of nanostructures. In addition, scanning electron microscopy (SEM) is used to support the morphological characterization. For measuring the magnetic properties of the nanowires, a superconducting quantum interference device (SQUID) magnetometry has been used. Ferromagnetic Resonance (FMR) also supports to measure the magnetic properties of the nanowires. For measuring the optical properties of the nanowires UV/VIS spectrometry is used.

In this section, the principles and the experimental setups of the techniques are described briefly.

3.2.1 Electron microscopy

3.2.1.1 Scanning electron microscopy (SEM)

In this experiment, a Leo 1530 SEM equipped with an accelerating voltage range of 200 V-30 kV and resolution less than 10 nm is used to characterize the morphology of Ni and Ag nanowires as well as their hybrids. In scanning electron microscopy, the images are produced by focusing an electron beam with energy typically within 5-20 kV at the surface of the sample to scan across it. The electrons interact with the atoms that lead to produce a variety of signals. The generated signals reveal information about the sample surface topography, chemical composition. The common SEM mode is to create the topography of the surface by detecting the secondary electrons emitted from the atoms of very close to the sample surface. In addition, the interaction of the back-scattered beam with atoms causes shell transition leads to emission of X-ray radiation with a certain energy characteristic of the parent element.

Thus, the detection and measurement of these energies permits the elemental analysis (energy dispersive X-ray spectroscopy or EDX). More extensive detailed description can be found in [98,99].

For SEM investigation of the cross-section of the samples, the nanowires embedded in the membrane, a part of the samples adhered on the Si substrate using carbon tape are placed parallel to the electron beam (applying special sample holder). In addition, for SEM investigation of the released nanowires, the samples are prepared by dropping few microliters of the nanowires solution onto the surface of Si substrate, then the samples re installed on the normal sample holder.

3.2.1.2 Transmission electron microscopy (TEM)

In these experiments, morphological, crystalline structure and chemical composition of nanowires were investigated using a FEI Tecnai F20 TEM and CM12 Philips TEM with a point resolution of 0.24 nm and an information limit of 0.14 nm. TEM works based on a transmission of an accelerated electron beam through a specimen and interacting with the atoms of the specimen and producing a variety of signals by electron-sample interaction. These signals are collected and reveal variety of information about the topography, crystalline structure, and chemical composition of the sample surface.

The electron gun emits an electron beam that is accelerated by a high voltage of 200 kV and focused onto the sample using a condenser lens system in vacuum. The electron beam is scattered as it passes through the sample and then focused by an objective lens system. Subsequently, it is amplified by magnifying lenses and finally it produces an image in the fluorescent screen. Images are taken by a multipixel CCD camera.

In scanning transmission electron microscopy (STEM) the electron beam is focused down to a small spot (1 *nm*) and scanned through the sample and spatial resolution in the STEM mode is 0.18 *nm*.

Energy dispersive X-ray (EDX) spectroscopy was used to reveal the chemical composition of the nanowires. When an incident electron is focused into the sample, there is a probability that it excites an electron in an inner shell with low energy of the sample atom. Consequently, one electron vacancy is created and the electron from an outer level with higher energy will jump into this vacancy to conserve the stationary state of the atom. This difference energy between the higher energy level and lower energy level can be released in the form of

X-ray radiation. Since each element has its unique atomic structure allows determining the elemental composition. When EDX spectroscopy measurements perform in STEM mode, the elemental distribution within the sample along so-called line scan can be determined as well as obtaining a two-dimensional elemental map. In this work, Energy-dispersive X-ray (EDX) spectra are recorded on the Tecnai microscope which is equipped with thin window energy-dispersive (EDAX.SUTW) Si (Li) detector. The energy resolution was 134 eV. For more details the reader is referred to [100,101,102].

For all TEM investigations, copper grids with an amorphous carbon are used as a substrate. The samples for TEM measurements are prepared by dropping few microliters of the nanowires solution onto a copper grid.

3.2.2 SQUID magnetometry

A SQUID (Superconducting quantum interference device) magnetometry is a powerful tool to magnetically characterize magnetic samples with high sensitivity. The experiments were performed using a SQUID magnetometer by Quantum Design (model MPMSXL) working at field up to 5 T and in a temperature range of 5-400 K. The system presents a resolution of $10^{-8} emu$ for $1mm$ by $1mm$ substrate covered with monolayer of a ferromagnetic metal and is equipped with 5 T superconducting coil. The magnetic moment is detected either as a function of the temperature in a constant field or as a function of the applied field at constant temperature. It makes possible to determine saturation magnetization, remanent magnetization, coercive field, and magnetic susceptibility. The SQUID magnetometry works based on superconducting loops containing Josephson junctions. The system detects the magnetic field by linear motion of the sample through the superconducting detection coils. For more detailed description of the system the reader is referred to [103,104]. In this experiment, the magnetization characterization is performed as a function of the applied magnetic field varied from -5 to 5 T at room temperature.

3.2.3 Ferromagnetic Resonance (FMR) spectroscopy

FMR spectrometer is a powerful tool for measuring the magnetic anisotropy and it contains a microwave resonant cavity with an electromagnet. For detecting the microwaves, one detector is placed at the end of the cavity. The sample is placed inside the resonator between

the magnet poles producing the homogeneous magnetic field and the incident microwaves. The angle-dependent FMR measurements can be performed for typically 5×5 mm^2 sized sample. The magnetic field is slowly swept produced by electromagnet reaching a maximum field of 1.6 T and simultaneously the resonant absorption intensity of the microwaves is detected. A klystron generates the microwaves at constant power of 200 mV. The resonant absorption abruptly increases if the frequency of the magnetization precession and the frequency of the resonant cavity are the same. The uncertainties of the setup are about ± 2 mT. For more detailed description, the reader is referred to [105].

For this work, FMR measurements are performed using a resonator-based X-band FMR setup at the microwave excitation frequency of $f = 9.77$ GHz at 300 K by varying the external magnetic field direction and magnitude.

3.2.4 UV/VIS-Spectrometry

The UV/VIS absorption spectra are acquired using a spectrometer from Perkin-Elmer, model "Lambda 35". It operates in the ultraviolet (UV) and visible (VIS) spectral ranges. It contains a tungsten-halogen-lamp (VIS) and a deuterium-lamp (UV) as light source and holographic concave grating with 1053 *line/mm*. For operating in the Vis range, one mirror (M_1) reflects the radiation from the halogen lamp onto source mirror M_2 and at the same time the radiation from the deuterium lamp is blocked. For operating in the UV range mirror M_1 reflects the radiation from the deuterium lamp onto source M_2. In combination with the installed silicon-photodiodes, the spectrometer has an operational range from 190 nm − 1100 nm with wavelength accuracy of $\pm$ 0.1 nm. Two photodiodes detectors are used one for the sample beam and the other for the reference beam.

In these experiments, for measuring the optical properties of Ag nanowires as well as hybrid segmented Ni-Ag nanowires the nanowires are immersed inside the ethanol.

4 Magnetic Ni nanowires

This chapter describes the growth of high quality Ni nanowires by direct current electro-deposition into anodic alumina membranes with interpore distances of 105 *nm* and tunable diameters (35-75 *nm*). The growth rate, crystallinity and magnetic properties of the Ni nanowire arrays are investigated as a function of the electrodeposition potentials in the range from -0.8 *V* to -1.5 *V* vs. the Ag/AgCl as reference electrode. The magnetic properties of Ni nanowires and annealed Ni nanowires at 650°C under Ar atmosphere are studied. A detailed analysis of the structural, morphological, and magnetic properties of the synthesized nanowires is performed using scanning electron microscopy (SEM), transmission electron microscopy (TEM), SQUID magnetometry and ferromagnetic resonance (FMR) measurement.

4.1 Synthesis of Ni nanowires

For these experiments, the nanowires were synthesized inside the alumina membranes by applying *DC* potential under potentiostat mode. In the following I give an overview of literature investigations.

The standard electrolyte water based solution for growing Ni nanowires (Watt's bath) contains 1.14 M $NiSO_4 \cdot 6H_2O$, 0.19 M $NiCl_2 \cdot 6H_2O$ and 0.73 M H_3BO_3 into water [6, 80]. The *pH* value of 4.5 was adjusted by boric acid used as buffer solution to keep the *pH* value constant during the process of electrodeposition. As it was mentioned in section 2.4, the exact adjustment of the *pH* value is very important for the deposition$(3 < pH < 5)$ since at low *pH* value (< 3) the acidic solution leads to dissolution of the membrane as well as an increase of H_2 evolution. On the contrary, high *pH* values (> 5) increase the amount of OH^- ions around the metallic ions that inhibits metal deposition.

The temperature of this electrolyte was typically adjusted to 35°C that affects the surface diffusion of atoms [6,80,84]. In fact, Anderea Cortes et al. experimentally investigated that at

lower temperature the quality of the crystalline structure of Ni nanowires decreases because of the presence of chloride ions into the electrolyte [9]. Napolskii et al. studied a modified deposition of Ni in anodic aluminum oxide (AAO) membranes in a limited range of applied potentials from around -0.7 to -1.2 *V* vs. Ag/AgCl corresponding to the measured cyclic voltammetry [93]. In addition, Proenca et al. investigated the fabrication of Ni nanowires in the range of potentials from -0.7 to -4 *V* which obtained from linear voltammetry measurement to fabricate nanowires with high growth rate [80]. In fact, at lower negative potentials than -0.7 *V* the rate of the depositions is very low and at higher negative potential the probability of H_2 evolution increases blocking some pores and stopping the deposition. It consequently has a bad effect on the homogeneous filling of the nanowires inside the pores.

In the following, I describe my investigation on the effect of the deposition potential on the structural, morphology and magnetic properties of Ni nanowires.

For the first experiments, we started to synthesize Ni nanowires at -1.5 *V* vs. the reference electrode and investigated the homogeneous filling of the pores and the crystallinity of the nanowires.

Figure 4.1 shows the schematics for the synthesis of Ni nanowires inside the alumina and preparing the sample for characterizing. The first and second steps show the preparing the fabricated membranes to synthesize nanowires by using *DC* electrodeposition. As it was described in section 2.4, the barrier layer for using this method of deposition should be removed and subsequently, one layer of metal, preferably Au, should be evaporated as electrode. These steps are described in detail in chapter 3. Step 3 represents the synthesizing of Ni nanowires inside the cell under the potentiostat mode by applying three electrodes. The length of the nanowires is controlled by monitoring the charge passed through the pores during the deposition time. After synthesizing the nanowires, the samples are prepared to characterize them. Step 4 illustrates the removing of the Au layer by wet chemical etching process. To measure magnetic properties of the samples after step 4 the samples are attached on the silicon substrate ($4\times4\ mm^2$) by using G-varnish glue. To prepare the sample for SEM and TEM characterizing step 5 is carried out that shows the process of releasing nanowires into ethanol after etching the membrane in a solution of *5Wt.%* NaOH in water. The details of these steps are described in section 3.1.5.
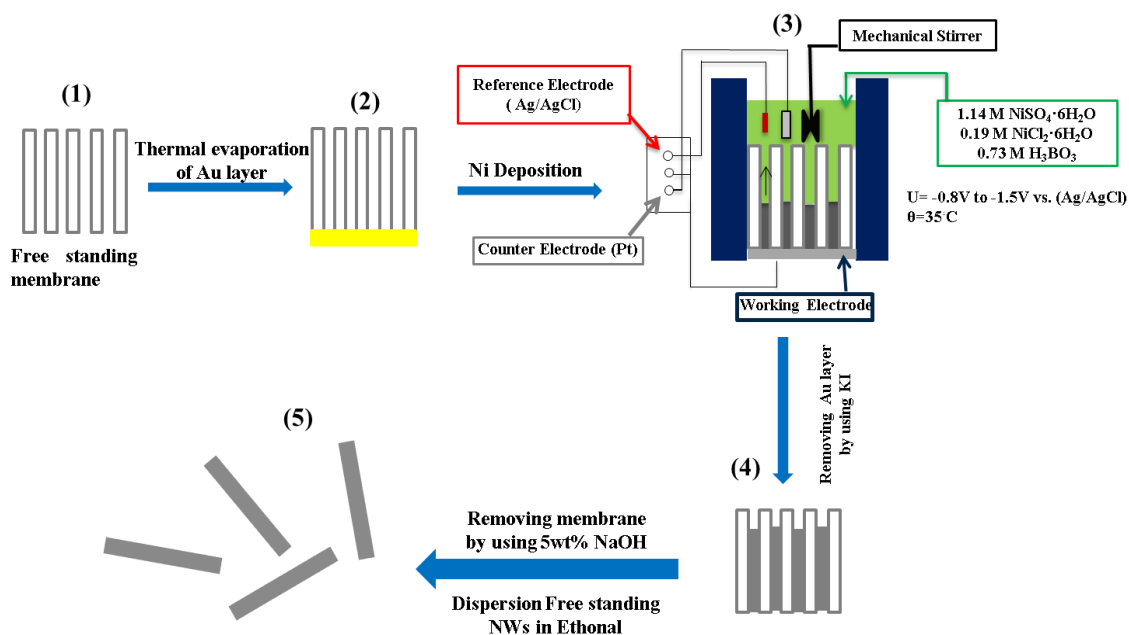
Figure 4.1. Schematic representation of the synthesis of Ni nanowires includes 5 steps. Step 1) and 2) illustrate the preparation of the membranes with the thickness 40 μm and 100 μm for *DC* electrodeposition: 1) removing the barrier layer at the bottom of the membrane and 2) depositing a layer of Au (300 nm thickness) as an electrode. Step 3) indicates the electrodeposition of Ni under potentiostat mode by applying 3 electrodes. Step 4) represents the removing of Au layer and step 5 releasing the nanowires in ethanol.

Figure 4.2 shows a cross section SEM image of Ni nanowires with diameter 70 (± 5) nm synthesized at -1.5V vs reference electrode embedded in the membrane. This Figure also proves that the pores are filled completely with Ni up to 1.5 μm length with narrow length distribution indicated the high quality of the synthesizing.
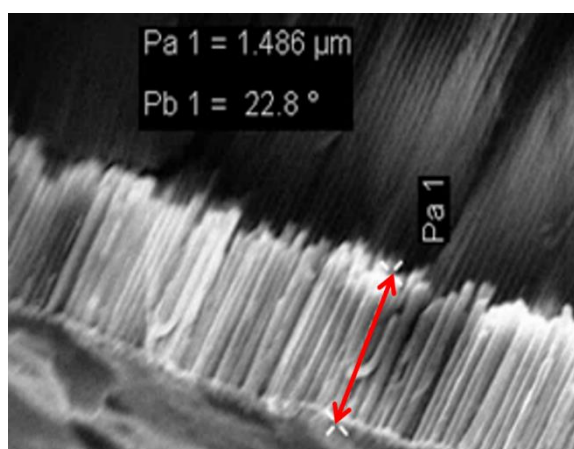

Figure 4.2. Cross section SEM image of the synthesized Ni nanowires in an alumina membrane with a length of up to 1.5 μm proving a complete filling of pores with Ni with narrow distribution of length (± 150 nm).

Figure 4.3(a-d) presents SEM images of synthesized high density Ni nanowires with different diameter and length after partial removal of the membranes. Figure 4.3a shows the dispersed nanowires on the surface of the sample. Figures (b-d) illustrate the agglomerated nanowires. As described in section 6.2.1, the bending stiffness of the nanowires depends on their diameter and aspect ratio. Consequently, for nanowires with long length and small diameter the bending stiffness is too small to keep them standing individually after removing the membrane.
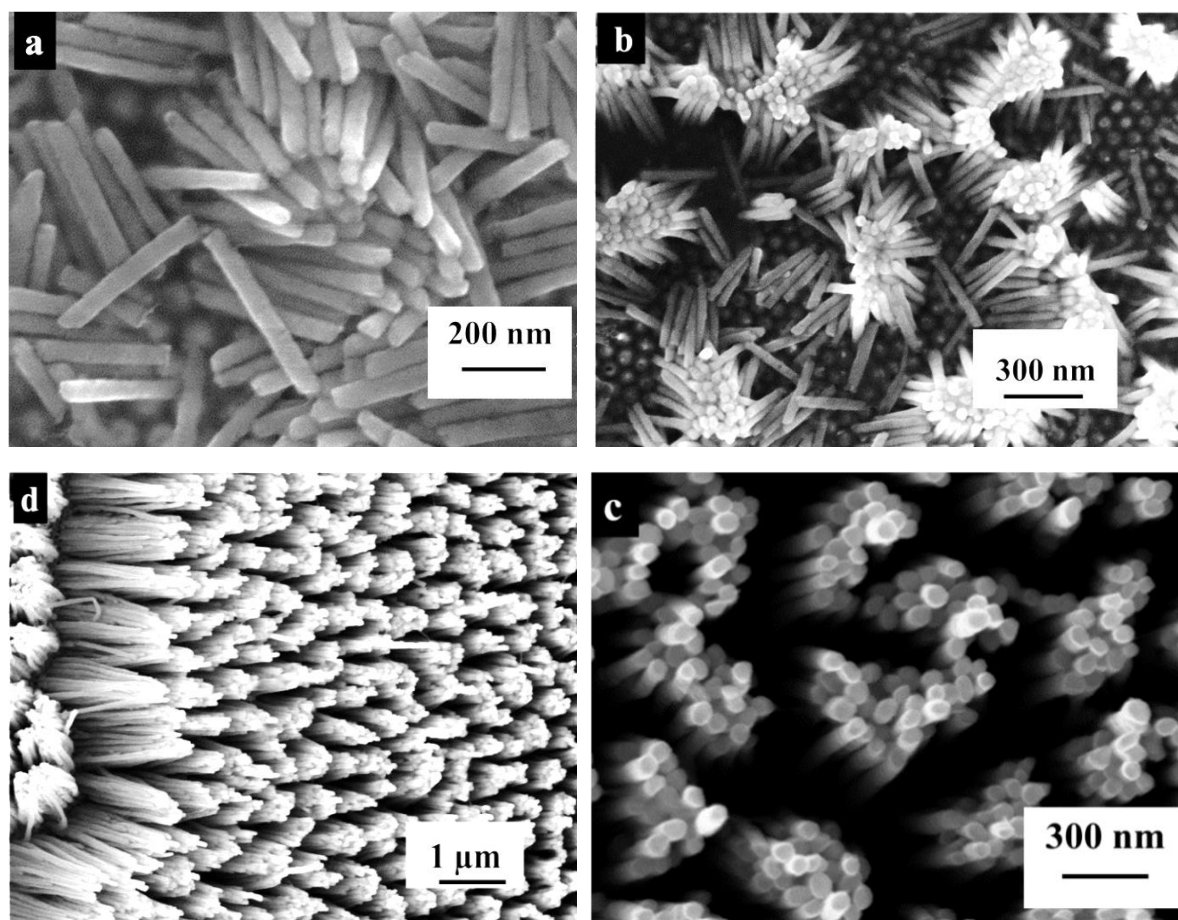

Figure 4.3. SEM images of synthesized Ni nanowires with different diameter and length after removing partially the membrane.

In Figure 4.4a) a TEM image of dispersed Ni nanowires on a carbon coated copper grid is shown. The corresponding energy dispersive X-ray (EDX) spectrum taken from the red area in Figure 4a) is shown in b). In addition, the EDX spectrum shows the existence of some contamination on the sample: Cr and P from chromic acid and phosphoric acid, respectively that were used for removing the membrane. The presence of Au can be referred to the remainder

of the Au electrode layer or to the formation of an alloy of Ni and Au for few angstrom at the beginning of the deposition process [106].
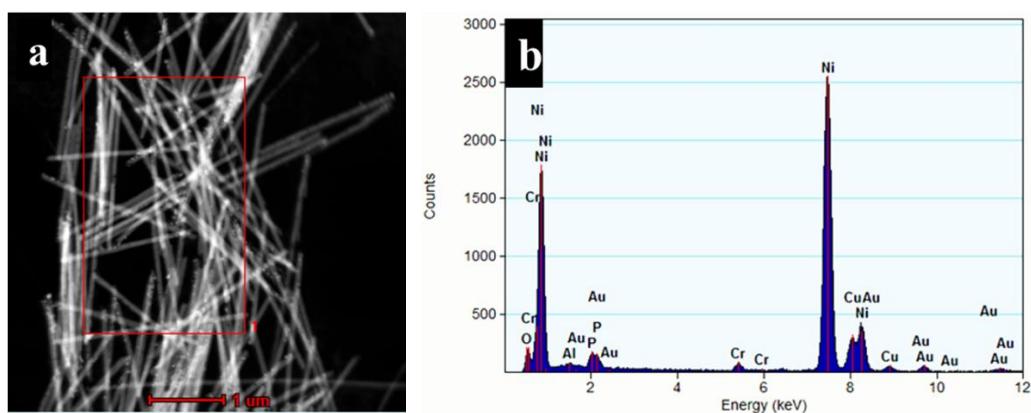

Figure 4.4. a) TEM image of dispersed Ni nanowires on a carbon coated copper grid and b) EDX analysis of Ni nanowires taken from the red area in a).

Figure 4.5 a) shows the TEM image of a single Ni nanowire with 80 *nm* diameter synthesized at -1.5 *V*. Figure 4.5 b) presents the HRTEM image of the Ni nanowire, the atomic planes with different orientations indicate the polycrystalline structure of the nanowire with crystal grain sizes ranging from 5 to 20 *nm*, and c) shows the electron diffraction pattern of Ni nanowires that can be indexed with FCC Ni with lattice parameter of $a_0 = 0.353$ *nm*.
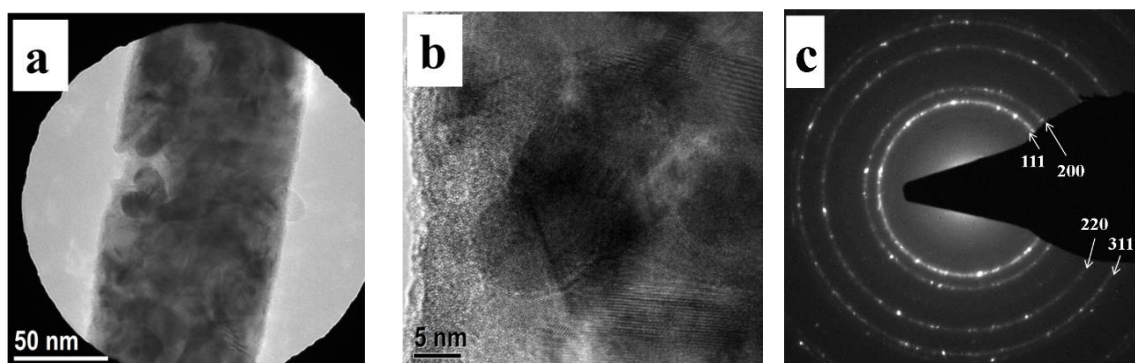

Figure 4.5. a) The TEM image of a single Ni nanowire with 80 *nm* diameter synthesized at -1.5 *V* vs the reference electrode and b) HRTEM image showing the polycrystalline structure of the nanowire. Electron diffraction pattern can be indexed with FCC Ni with $a_0 = 0.353$ *nm*.

As it was explained in section 2.4, the process of electrodeposition involved: charge transfer; diffusion; reaction; and adsorption on the substrate is complex and the mechanism of growth is not completely clear. However, the deposition parameters influence the structure of the nanowires. Many works have been done to investigate the effect of the electrolyte composition, *pH* value, temperature, and size as well as the deposition potentials [7-9,83,107-111] however, some results were in conflict. Here, the purpose is to improve the crystallinity of Ni nanowires by synthesizing the single crystalline structure or at least by increasing the grain sizes of the polycrystalline structure. The crystalline nanowires will grow if the size of an initial cluster exceeds the critical dimension, N_c (a cluster of N atoms) [7] in which the larger it is more favorable for a single crystal growth, and it can be expressed for two-dimensional-like nucleation/growth mechanism (epitaxially) as $N_c = \frac{bs\epsilon^2}{(Ze\eta)^2}$ where, s, ϵ, Z, η and *b* are the area occupied by one metallic atom on the surface of the nucleus, the edge energy, the effective electron number, the deposition potential and a constant, respectively. According to this formula, one possible alternative for growing nanowires with single crystal structure is the 2D-like nucleus [7,8] and the single crystal nanowires grow epitaxially. Reducing the deposition potential allows to increase N_c, then single crystal growth is more favorable.

In addition, the crystallographic orientation of the specimen is determined by the orientation of the first nuclei corresponding to the theory of the 2D nucleus [112]. The preferred growth orientations are adjusted by the principle of the minimum energy during the process of the electrodeposition [9]. The lower the surface energy needs the lower deposition potential to create a certain growth orientation.

The deposition potential influences not only the nucleation/growth mechanism but also the hydrogen evolution. At higher absolute values of the potential, the probability of hydrogen evolution increases and leads to polycrystalline structures because of the presence of bubbles inside the membranes resulting in secondary nucleation with different growth orientation of the metal. In addition, the higher the deposition potential, the faster is the nucleation rate resulting more likely in polycrystalline nanowires [109].

Consequently, to improve the mechanism of nucleation/growth the effect of deposition potential on the structure of Ni nanowires are studied as described in the next section.

4.1.1 Electrodeposition of Ni nanowires at different potentials

To investigate the effect of deposition potential on the structure of Ni nanowires as well as their magnetic properties, the synthesis was performed in the potential interval E = −0.8 to −1.5 *V* vs. saturated Ag/AgCl electrode. To estimate the rate of deposition at different potentials, the time of the deposition for each sample was 10 *min*. Except for the nanowires synthesized at -0.8 *V* vs. reference electrode, because of low growth rate at this condition, the duration of electrodeposition was 20 *min*. For these experiments, first commercially available porous anodic aluminum oxide membranes purchased from Smart Membrane Company were used, with a membrane thickness of 100 *μm* and an average pore diameter of 45 (±5) *nm* with interpore distance of 105 (±1) *nm*. Then, to measure the magnetic properties of the nanowires with different aspect ratios home-made membranes were used with thickness of 40 *μm*, interpore distance of 105 *nm* and tunable diameters (35-75 *nm*).

4.1.2 Morphology and crystalline structure

After synthesizing the nanowires at different potentials, they were released from the membrane and then dispersed on a substrate to characterize them. The steps of this process are explained in section 3.1.5. Figures 4.6(a-f) show SEM images of individual and bunched Ni nanowires on a TEM grid. They were synthesized at potentials a) -0.8 *V*, b) -0.9 *V*, c) -1.0 *V*, d) -1.1 *V*, e) -1.2 *V* and f) -1.5 *V*. During the deposition process the length of the nanowires is estimated by monitoring the charge passing through the working electrode. It is observed that the length of the nanowires strongly depends on the deposition potential.

The deposition rates of nanowires are plotted in Figure 4.7. It shows that the average growth rate of the deposition increases linearly by increasing the deposition potential. The error bars are estimated by considering the length distribution of nanowires in each sample. At lower deposition potentials (-0.8 and -0.9 *V* vs. the reference electrode) the length distribution is low. However, at the higher deposition potentials the distribution of lengths is larger which can be because of more H_2 evolution that occurs at higher applied potentials [93].
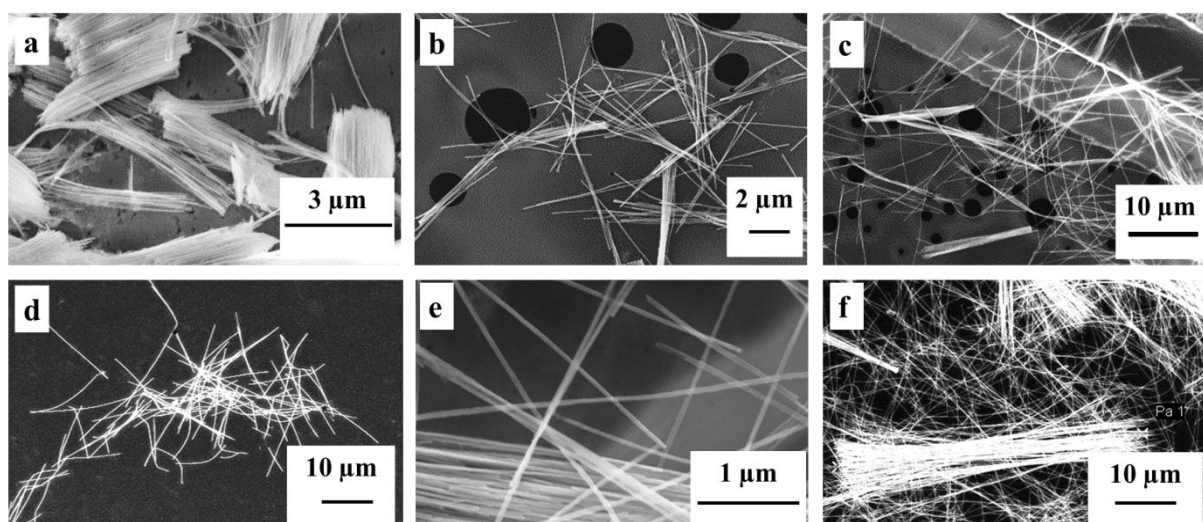
Figure 4.6. SEM images of released Ni nanowires after 20 *min* of deposition at constant potential vs. reference electrode of (a) -0.8 *V* (L~3.7µm); and after 10 min of deposition at potentials of (b) -0.9 *V* (L~6 µm); (c) -1*V* (L~16 µm); (d) -1.1*V* (L~18µm); (e) -1.2*V* (L~21µm), (f)-1.5*V* (L~ 50µm).
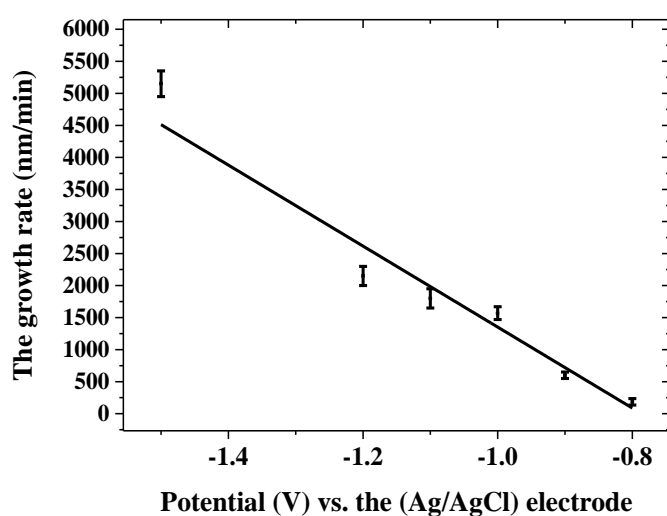

Figure 4.7. The growth rate of Ni nanowires synthesized at different deposition potentials. For each sample the error bar was estimated by considering the length distribution of nanowires.

Figure 4.8(a-d) presents the morphology and crystal structure of Ni nanowires. According to the TEM studies of the samples, the diameter of the nanowires is very close to the pore diameter ($45(\pm 5)$ nm). Figure 4.8a) presents a TEM image of Ni nanowires (synthesized at -1.1 *V*) with various crystalline grains displaying contrast due to different electron diffraction conditions and b) is the SAED pattern of Ni nanowires confirming the polycrystalline nature of nanowires. The synthesized nanowires with different deposition potentials are uniform and

mostly polycrystalline, however, among them single crystalline nanowires are found for all samples.

For samples synthesized at -1 *V* and -1.1 *V*, better crystallinity is observed. The grain size reaches up to 50 *nm*. In Figure 4.8c) the SAED pattern of one nanowire (see inset) confirms its single crystalline structure with <011> growth orientation. For all samples the same growth orientation is observed. In Figure 4.8d) a high resolution TEM (HRTEM) image proves the single crystalline nature of one nanowire. The d_{111} interplanar spacing is determined to be 0.206 *nm*, corresponds to the interplanar distance of {111} planes in face-centered cubic (FCC) Ni (lattice parameter of Ni $a_0 = 0.352$ *nm*).

Table 4.1 shows a summary of the TEM measurements of samples synthesized at voltages ranging from -0.8 to -1.5 *V* vs. the reference electrode.

In a previous study, it was reported that the textures of Ni nanowires are insensitive to the deposition conditions [7], as the higher binding energies of Ni lead to aggregation of atoms into 3D clusters. In contrast, in other studies, the effect of the different electrochemical potentials on the crystallinity and crystallographic properties of Ni nanowires were observed [8,9,83,93,113,114]. Here, despite polycrystalline nature of most the Ni nanowires, at potential ranges -1 *V* and -1.1 *V* vs. the reference electrode, the crystallinity of them is better: it was observed larger grain sizes in polycrystalline nanowires, as well as more single crystalline ones.

Here, the polycrystalline structure of the synthesized Ni nanowires at different deposition potentials indicates the influence of the other deposition parameters on the structure of the nanowires. In particular, the pore size of the membranes [115-117] as well as the *pH* value and the temperature of the electrolyte [110,118].
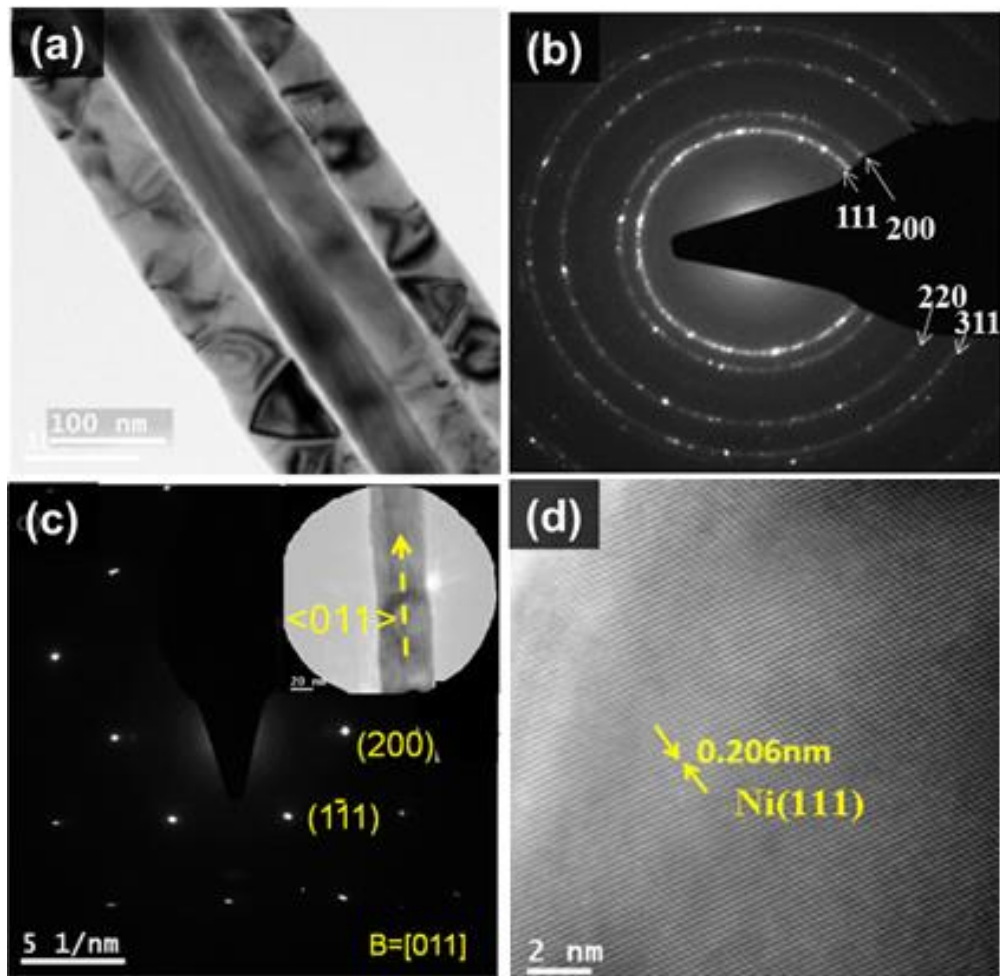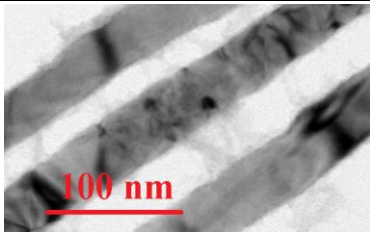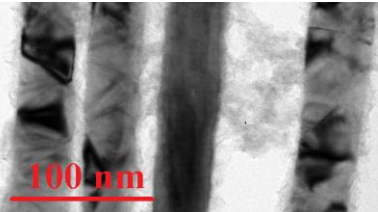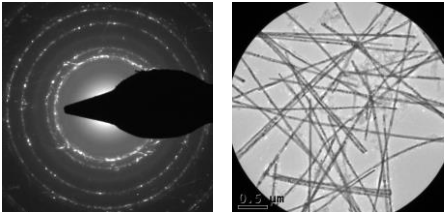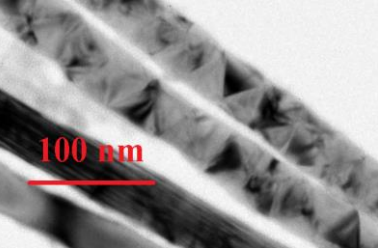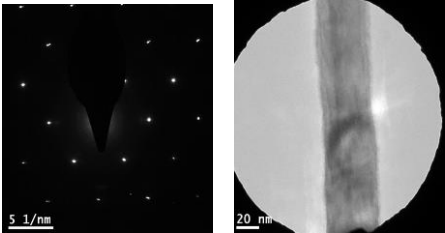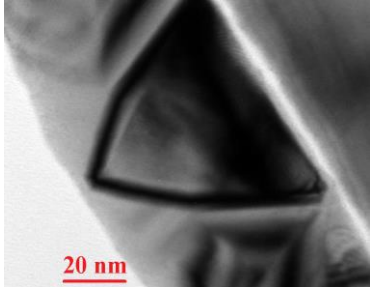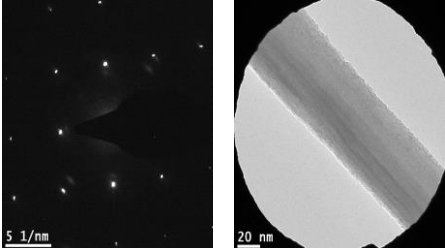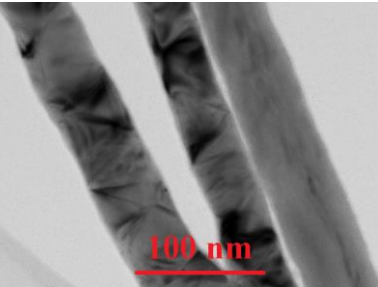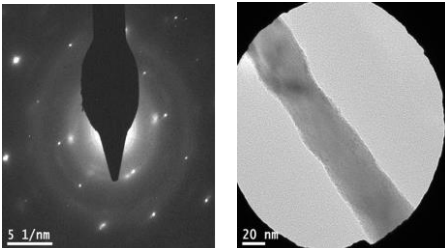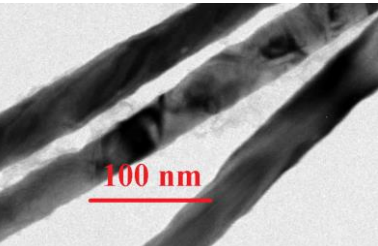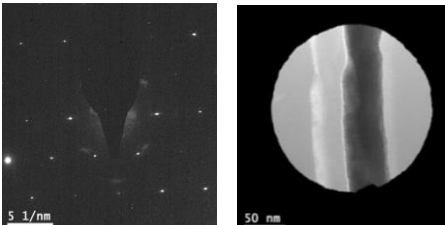
Figure 4.8. a) TEM images of Ni nanowires synthesized at -1.1 *V*. Various crystalline grains display different contrast due to different electron diffraction conditions. b) SAED pattern of Ni nanowires that indicate the polycrystalline nature corresponding to a FCC structure. c) SAED pattern of a single Ni nanowire (see inset). d) HRTEM image showing a crystallinity of a single Ni nanowire. The lattice spacing in (111) direction is 0.206 *nm* as indicated.

Xue Wei Wang et al. investigated that the probability for the formation of single crystals inside membranes with smaller diameter is higher [109]. The growth orientations are adjusted by the tendency of the minimization of the surface energy and for smaller diameters the interface energy between Ni and the wall of the alumina membrane can dominate the growth directions. In contrast, for bigger diameters, at the beginning of the growth mechanism, the area of the interface of the Ni and the electrolyte is bigger than that of the circumference side of the pore wall so the growth orientation is adjusted by minimizing the interface energy between Ni and the electrolyte. It means that the pore size effects not only the morphology of the nanowires but also on the crystalline structure of them.

Furthermore, Andrea Cortes et al. observed that at a certain deposition potential there is a critical pore diameter below which the mononuclear growth mode dominates resulting in the formation of single crystal nanowires [9]. The critical pore diameter for synthesized single-crystalline Ni nanowires is reported smaller than 50 nm [77]. In this work, the diameter of the nanowires was $45\ (\pm5)\ nm$ which is below the critical pore diameter. Within the error bar, however, it may still be too big and the reason for producing polycrystalline nanowires.

Additionally, it seems that the thickness of the membrane can influence the quality of the synthesized nanowires. For our $100\ \mu m$ thick membranes it is more difficult for hydrogen gas to escape of the channels than for $40\ \mu m$ membranes, that were typically used in the previous works. The hydrogen gas inside the pores creates vacancy or secondary nucleation with different growth orientation. In addition, the pH value (4.5) of the electrolyte can influence the crystallinity. At more acidic pH value, better crystallinity is obtained due to less hydroxide [119].

TABLE 4.1. Summary of the TEM data for Ni nanowires synthesized at different voltage.

Potential (V) vs. Ag/AgCl	Crystallinity	TEM images	Electron Diffraction Pattern
-0.8	-Polycrystalline		
-0.9	-Polycrystalline		
-1.0	-Polycrystalline With better crystallinity and the growth orientation<011>		
-1.1	-Polycrystalline with better crystallinity, the growth orientation is <011>		
-1.2	-Polycrystalline		
-1.5	-Polycrystalline		

4.2   Magnetic characterization of Ni nanowires

The magnetic measurements were performed using SQUID magnetometry at 300 *K* and a maximum magnetic field of ± 2.0 *T*. All the data have been normalized to the saturation magnetization and the diamagnetic signals from the Si substrates and GE-varnish glue were subtracted.

4.2.1   Role of geometry

To study the influence of the geometry of the nanowires on magnetic properties two different samples were considered. Samples were synthesized with the same conditions by choosing the deposition potential -1.5 *V* vs. Ag/AgCl as the reference electrode. The pore diameters of the samples were 40 *nm* and 60 *nm* with the length of 1400 *nm* and 600 *nm*, respectively. The samples are labeled *40 nm* and *60 nm* and their porosities P corresponding to the interpore distance of 105 *nm* were calculated to be 13% and 30%, respectively.

Figure 4.8 (a-b) shows the hysteresis loops of these Ni nanowires inside the membrane. The hysteresis loops were measured with the magnetic field applied parallel (∥) and perpendicular (⊥) to the nanowire axis at 300 *K*.

To determine the saturation magnetization, *Ms,* the volume fraction of nickel nanowires in the pores of the membrane was calculated. For both samples the saturation magnetization was $M_S = 474\ (\pm 10) \times 10^3\ \frac{A}{m}$, the error bar is given by the distribution of the length of the nanowires. This value is roughly in good agreement with previous works [38,120]. In fact, the defects and vacancies that usually occur during the electrodeposition can make a small difference between this value and the literature.

The hysteresis loops for sample *40 nm* in Figure 4.8 a) show a square-like shape when the applied field is parallel to the wire's axis and s-like shape when the applied filed is perpendicular to the wire's axis. The magnetic information from the hysteresis loops suggests an easy axis parallel to the nanowires ($H_s{}^{\parallel}$=230 *mT* < $H_s{}^{\perp}$=455 *mT*) and a hard axis oriented perpendicular to the wire's axis that exhibits a uniaxial anisotropy. Corresponding to the porosity of *P = 13%* it is expected that the easy axis is parallel to the nanowire axis because the shape anisotropy overcomes to the dipolar interactions among the nanowires [38, 121,122].

The hysteresis area is bigger when the applied field is parallel to the wire's axis that indicates a bigger coercive field (H_c) and normalized remanent magnetization (M_r/M_s). The hysteresis loop measured in parallel direction shows a coercive field of $\mu_0 H_c^{\parallel} = 96\ mT$ and the normalized remanent magnetization of $M_r/M_s = 70\%$. For perpendicular direction, the hysteresis loop presents a low coercive field of $\mu_0 H_c^{\perp} = 14\ mT$ and low normalized remanent of $M_r/M_s = 10\%$. These values for coercive fields are in good agreement with the data reported in previous works [121,123]. However, the values for the remanent magnetization are smaller than reported previously that indicates stronger dipolar interactions among nanowires [124].

To compare these experimental values with a theoretical approach, the coercive field for ideal case of isolated nanowires for homogeneous rotation, coherent magnetization reversal, [125] can be given by

$$\mu_0 H_c = \mu_0 H_A + \mu_0 H_{Mc}$$

In fact, the origin of the magnetic anisotropy of an array of the magnetic nanowires inside the membrane are: 1) The magnetocrystalline anisotropy field, $2K_u/M_S$ with K_u the uniaxial anisotropy constant; 2) The shape anisotropy field, H_A, given by $\mu_0(N_\perp - N_\parallel)\,M_S$; and 3) The dipolar interactions among the nanowires given by $-\,{}^{3}\!/_{2}\ \mu_0 M_S P$ [38,120].

For sample *40 nm* the magnetocrystalline anisotropy and the dipolar interactions are estimated about $\mu_0 H_{MC} = 21\ mT$ and $-3/2\mu_0 M_S P = -0.11\ T$, respectively.

The shape anisotropy of a single wire is obtained as $\mu_0 H_A = 0.29\ T$ by calculating the demagnetizing factors perpendicular and parallel to the wire axis $N_\parallel = 0.00327$ and $N_\perp = \frac{1-N_\parallel}{2} = 0.498$ from the aspect ratio 35. As the result, the contribution of shape anisotropy dominates favoring the magnetic easy axis to be parallel to the wire's axis.

By neglecting magnetocrystalline anisotropy and considering isolated nanowires the coercive field $\mu_0 H_c = 0.29\ T$ is significantly bigger than the coercive field taken from the hysteresis loop. As the magnetization reversal modes have a large influence on the coercivity of nanowires, it might be more likely that domain walls nucleate at the ends of the nanowires and propagate along the nanowires instead of coherent rotation [125-128]. For isolated cylindrical nanowires three main reversal modes exist included: 1) coherent rotation, 2) vortex domain wall and 3) transverse domain wall that they depend on the geometry, material, and crystalline structure [31,125].

Figure 4.7 b) shows the measured hysteresis loops for sample *60 nm*. It is a s-like shape. The saturation magnetization was obtained roughly at the same external field for parallel and

perpendicular applied magnetic field ($H_s^{\parallel} \sim H_s^{\perp} = 200\ mT$). It seems that this sample does not have a preferential magnetic orientation [38]. However, because the area of the hysteresis loop is bigger when the applied field is parallel to the wire axis there is an easy axis oriented along the wire axis. The hysteresis loop measured in parallel direction shows a coercive field of $\mu_0 H_c^{\parallel} = 48\ mT$ and the normalized remanence of 40%. For perpendicular direction, the hysteresis loop shows a coercive field of $\mu_0 H_c^{\perp} = 7\ mT$ and the normalized remanence of 1%.

The shape anisotropy of sample "60 nm" with the aspect ratio 10 and the demagnetization factors $N_{\parallel} = 0.0141$ and $N_{\perp} = \frac{1-N_{\parallel}}{2} = 0.492$ is $\mu_0 H_A = 0.28\ T$.

According to the porosity $P = 30\%$ of sample 60 nm, the effective magnetization is estimated $-{}^3/_2\ \mu_0 M_S P = -0.26\ T$.

As the result, close packing nanowires inside the membrane leads to large magnetostatic interactions which reduce the individual shape anisotropy field [129,130] of the wires. The effective anisotropy field arising from the shape anisotropy and dipolar interaction among the nanowires can be estimated by [49,131]:

$$\mu_0 H_D = \mu_0(N_{\perp} - N_{\parallel})M_S - {}^3/_2\ \mu_0 M_S P = \mu_0 M_s\left((N_{\perp} - N_{\parallel}) - {}^3/_2\ P\right)$$

For nanowires with large aspect ratio the demagnetizing factors are $N_{\perp} = \frac{1}{2}$ and $N_{\parallel} = 0$ in good approximation [132] so

$$\mu_0 H_D = \frac{1}{2}\mu_0 M_s(1 - 3P)$$

For sample 60 nm,

$$\mu_0 H_D = 20\ mT$$

If magnetostatic interaction cancels the shape anisotropy, the direction of the easy axis depends on the magnetocrystalline anisotropy. For nanowires with porosity more than $35 - 38\%$ [47,49,133] the magnetostatic interaction that favours an alignment of the magnetization perpendicular to the wire axis overcomes the shape anisotropy as well as the magnetocrystalline anisotropy so there is a reversal of the orientation of the easy axis from parallel to perpendicular to the wire axis.

The coercive field and the normalized remanent magnetization of both samples are summarized in Table 4.2. It shows that by increasing the diameter of the nanowires the coercive field decreases in the case of magnetic field applied parallel and perpendicular to the wire axis

that is in good agreement with theoretical prediction [125]. For these two studied samples the difference of coercive field of about 50% indicates that the magnetization reversal process for them is not similar.

By increasing the diameter of the nanowires, the normalized remanent magnetization decreases that it is in good agreement with theoretical predictions [125]. The formation of an open vortex structures at the ends of the nanowires, resulting in minimizing the magnetostatic energy, can describe the decrease of the remanence [134].

a)

b)
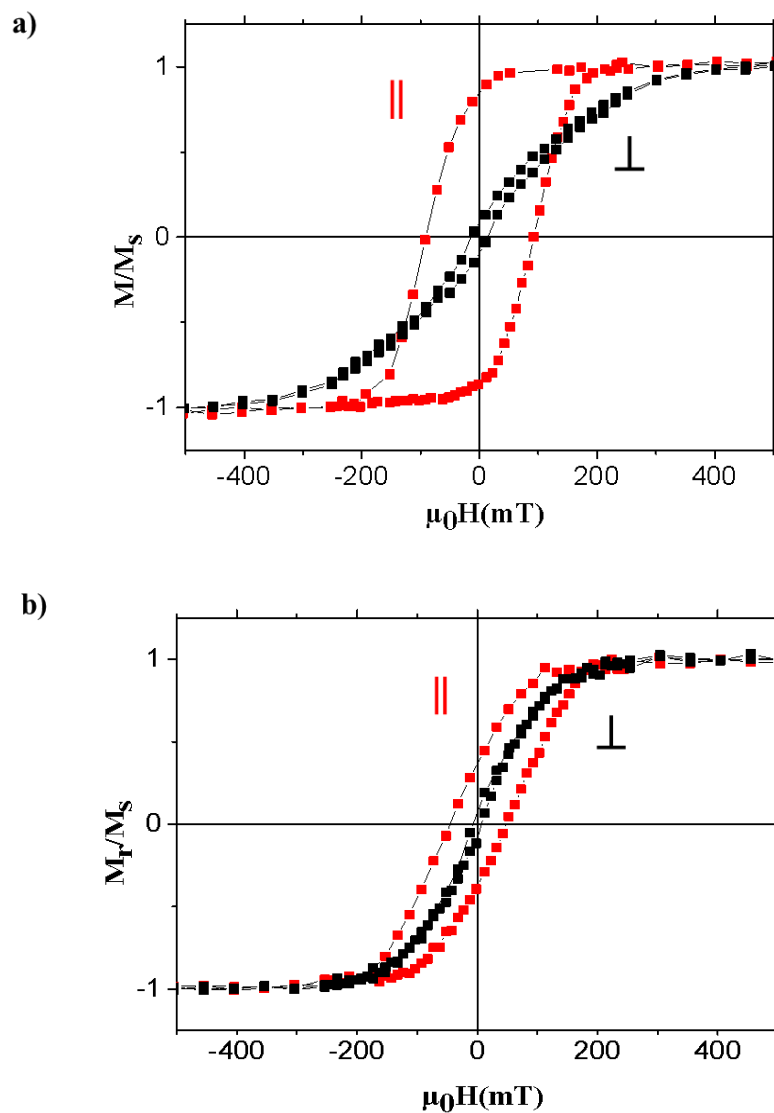
Figure 4.8. Selected hysteresis loops of Ni nanowires with a) diameter 40 *nm* and length 1.4μm and b) diameter 60 *nm* and length 600 *nm*. Magnetic properties were measured by SQUID magnetometry at 300 *K* with the magnetic field applied parallel (∥ red squares) and perpendicular (⊥black squares) to the nanowire axis.

TABLE 4.2. Summary of the magnetic data (coercivity and the normalized remanent magnetization) for Ni nanowires with different diameter and aspect ratio. The error bars show the distribution of length and diameter of Ni nanowires.

Sample	Length(nm)	Aspect ratio (l/d)	Porosity	Coercivity (mT)		M_r /M_s	
				∥	⊥	∥	⊥
60 nm	600±100	10	30%	48	7	0.4	0.01
40 nm	1400±150	35	13%	96	14	0.7	0.1

In the following, to tune the magnetic properties of Ni nanowires by modifying the crystal growth direction [135,136] the Ni nanowires were synthesized at different applied potentials. The purpose of this experiment is to study the influence of the deposition potential on the crystalline structures subsequently, the magnetic properties. Three samples were prepared with the diameter 40 *nm* and interpore distance of 105 *nm* and with the length of 1.4 *μm* synthesized at different deposition potentials -1*V*, -1.2 *V* and -1.5 *V* vs. the reference electrode. According to TEM measurements (Table 4.1) the growth orientation of Ni nanowires did not change for these samples and it was < 011 > .

The hysteresis loops of these three studied samples were measured at 300 *K*. According to the results, listed in Table 4.3, by applying external field parallel and perpendicular to the wire's axis similar magnetic properties are roughly observed. Since for Ni nanowires the magnetocrystalline anisotropy is negligible in comparison with the shape anisotropy, the magnetic properties of the synthesized Ni nanowires at the different deposition potentials are similar. However, in previous works, it was reported that the coercive field of Ni nanowires with single crystalline structure is larger than for polycrystalline [93].

TABLE 4.3. Summary of the magnetic data (coercivity and the normalized remanent magnetization) for Ni nanowires with similar diameter and aspect ratio but synthesized at different deposition potentials, -1, -1.2, -1.5 *V* Vs. the reference electrode. The error bars show the distribution of length and diameter of Ni nanowires.

Applied voltage(V)	Length(nm)	Diameter(nm)	Aspect ratio (l/d)	Porosity	Coercivity (mT)		M_r / M_s	
					∥	⊥	∥	⊥
-1.5	1400±150	40±5	35	13%	96	14	0.7	0.1
-1.2	1400±150	40±5	35	13%	92	14	0.8	0.1
-1.0	1400±100	40±5	35	13%	96	15	0.9	0.1

4.2.2 Temperature dependent magnetic properties

The hysteresis loops were measured for the sample labeled with *40 nm* with the magnetic field parallel to the nanowires long axis in the range of temperatures 10, 25, 75, 100, 150 and 300 *K*. In Figure 4.9 (a-b), the saturation magnetization and the coercive field as a function of temperature were plotted. The error bar for the saturation magnetization was estimated by

considering the distribution of diameter and length of nanowires. The error bar of the coercive field is given by the field steps chosen for the hysteresis loops in Figure 4.9. It is observed that at room temperature the samples still show almost full magnetization. These results are expected, at temperatures below 50% of the Curie temperature only slight decrease of the saturation magnetization is observed [31]. The Curie temperature of Ni is 613 K and the saturation magnetization doesn't change significantly in the temperature range of 10-300 *K*.

In addition, in Figure 4.10 the dependence of a) the saturation magnetization and b) the coercive field of the sample on temperature are plotted. There is a slight decrease (linearly) for both with increasing temperature between 10 *K* and 300 *K*.
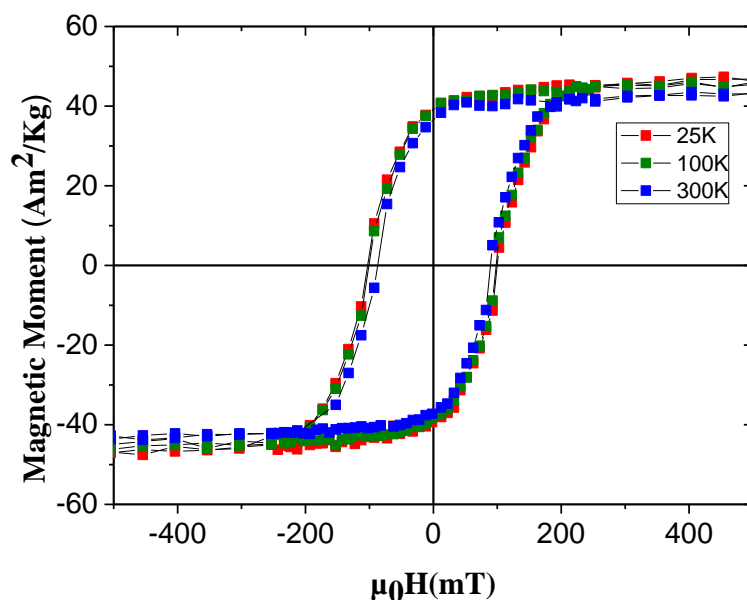

Figure 4.9. Hysteresis loops of Ni nanowires synthesized at -1.2*V* vs. (Ag/AgCl) with diameter 40 *nm* and length 1.4*μm* at different temperatures with the magnetic field applied parallel to the nanowires axis.
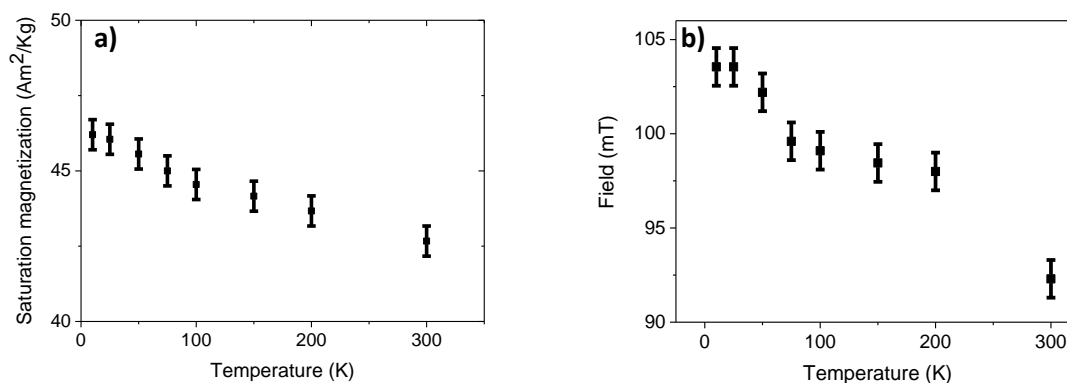

Figure 4.10. a) Magnetic saturation and b) coercive field as a function of temperature for Ni nanowires.

61

4.2.3 Role of thermal treatment

Crystallite sizes and orientation as well as stress of Ni nanowires in the membrane may lead to significant variation of the magnetic properties. In this experiment, we investigated the influence of annealing process on crystallinity so on the magnetic properties of Ni nanowires.

According to the recrystallization temperature for nickel ($600°$ C) [137] for annealing of Ni nanowires T = $650°$ C was chosen. The thermal expansion coefficient of AAO is very small *($8.8\times10^{-6}K^{-1}$),* so the pore diameter does not change during the thermal treatment. On the other hand, at higher temperature the pore walls of the membrane may produce a radial stress on the nanowires due to the different thermal expansion coefficients of Ni ($13\times10^{-6}K^{-1}$) and alumina. So, for supplying the adequate energy for crystallite growth and possible reorientation instead of increasing the temperature of the annealing process the time of the annealing process was considered 24 *h* under Ar atmosphere. The magnetic properties of as-prepared and annealed nanowires with diameter 40 *nm* and a length of 1.4 *μm* were measured at room temperature by applying the external field parallel and perpendicular to the wire's axis (Figure 4.11a-b).

The thermal treatment causes to 55% decrease of coercive field indicating sufficient reduction of the effective magnetic anisotropy for the sample. Decreasing coercivity supports the prediction that by annealing the defects and vacancies of the nanowires will be decreased. For interpreting such behavior, as it was mentioned previously the coercive field of nanowires strongly depends on the mechanism of the reversal modes. In fact, the domain wall nucleation occurs at the vacancies and defects so pins the magnetization and will effectively increase the coercive field.

In addition, the thermal treatment improves the crystallinity of the nanowires but for Ni case with very low magnetocrystalline anisotropy, improvement of the crystallinity can hardly be the reason of such decreasing the effective anisotropy. Moreover, as the saturation magnetization of nanowires after annealing was not changed so the shape anisotropy and the dipolar interactions among the nanowires remained unaltered. Another contribution to the effective anisotropy that should be taken into account is the magnetoelastic anisotropy. During the thermal treatment, the Ni nanowires are exposed to the stress due to the mismatch between the thermal expansion coefficient of Ni and alumina. The Ni nanowires tend to expand more than the membrane result in the lateral compressive stress.
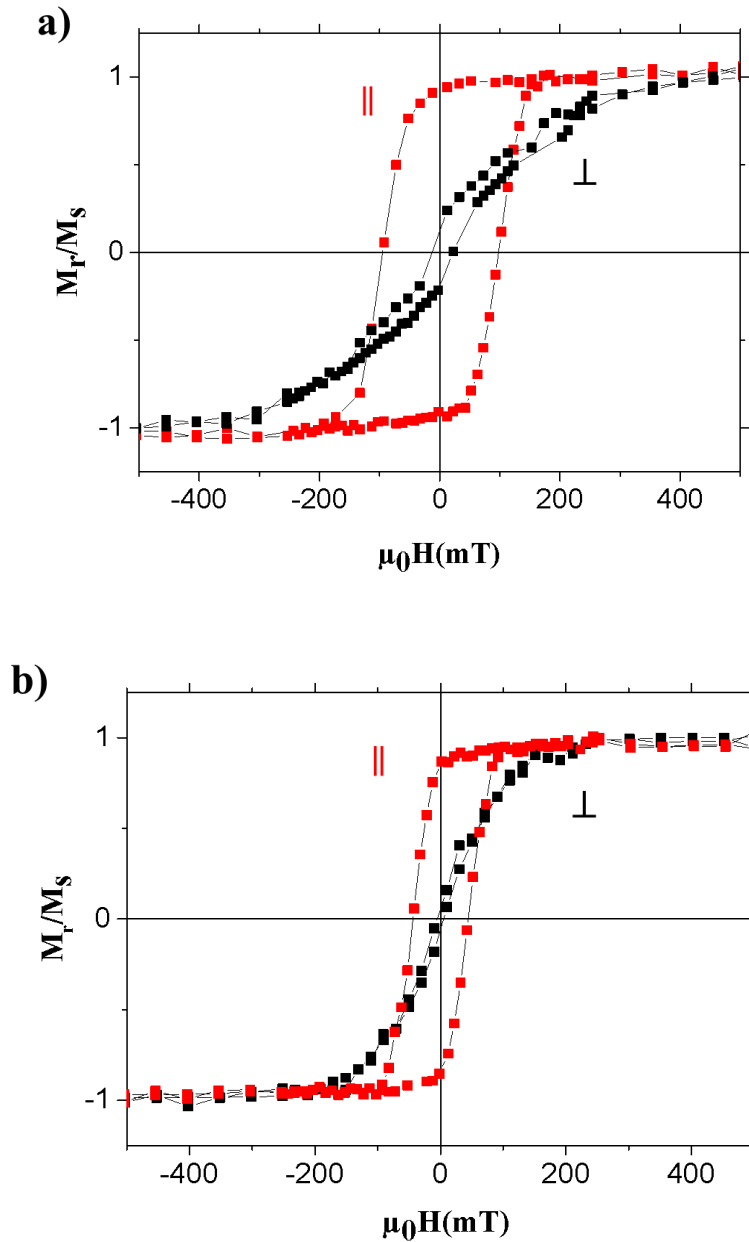
Figure 4.11. Hysteresis loops of (a) as-prepared and (b) annealed samples (annealed at 650$^{°}$C under Ar atmosphere for 24h) for a hexagonally ordered Ni nanowire arrays synthesized at -1V vs.(Ag/AgCl) with a constant interwire distance of 105 nm, length of ~1.4μm, and pore diameter of ~ 40 nm measured with an applied field parallel and perpendicular to the wires at 300K.

TABLE 4.4. Summary of the magnetic data (coercivity and the normalized remanent magnetization) for as prepared and annealed Ni nanowires with diameter 35nm, interpore distance 105nm, and length 1.4 μm.

Sample	$\mu_0 H_c$(mT) $\parallel$	Mr/Ms $\parallel$	$\mu_0 H_c$(mT) $\perp$	Mr/Ms $\perp$
As-prepared	98	0.9	22	0.2
Annealed	45	0.8	5	0.05

4.2.4 Magnetic anisotropy and the effect of dipolar interaction

To characterize the effective anisotropy field H_{eff} for Ni nanowires embedded in the membrane, ferromagnetic resonance (FMR) is used. For this study two samples of Ni nanowires with the length of ~1.6 μm, center to center separation of 105 nm and with the diameters of 45 nm and 35 nm were produced. FMR measurements were performed by using the conventional FMR X-band set-up at microwave excitation frequency 9.77 GHz. A goniometer has been used for angular dependent measurements. FMR spectra were recorded by sweeping the external magnetic field from perpendicular to parallel to the nanowires axis.

Figure 4.12 a) shows the angular dependence of Ni nanowires with diameter 45 nm with the best fit. The hysteresis curves were measured for the same sample by applying the external field parallel and perpendicular to the nanowires axis at room temperature (Figure 4.12b). From these results, coercive field and magnetization are determined and summarized in Table 4.5.

It is observed that the resonance field (H_r) obtained from the FMR measurement is minimum when the orientation of the applied field is parallel to the nanowires's axis, H_r= 140 mT, indicated the direction of the easy axis is parallel to the nanowires's axis.

Figure 4.12. a*)* Observed angular dependence resonance field at 9.77 *GHz* at room temperature for pure Ni nanowires with interwire distance of 105 *nm* and pore diameter 45 *nm*, the constant length of Ni segment~ 1.6 *μm* and the best fit. b) corresponding hysteresis loops measured with an applied field parallel (∥) and perpendicular (⊥) to the wires at 300*K*.

The resonance frequency is given as explained in section 2.2. According to the FMR spectra, the effective anisotropy fields can be estimated according to equations (2.20) and (2.21) and the effective field is obtained from equation (2.19).

According to the saturation magnetization value for the studied sample ($M_s = 474 \times 10^3 \, ^A/_m$), the second term of equation (2.19) is calculated 21 mT that is negligible in comparison with the first term that is estimated 160 mT.

By taking g = 2.2 [45,49,138] the values of the effective field is calculated and the results are summarized in Table 4.5 for the sample with diameter 45 nm.

TABLE 4.5. Summary of the magnetic parameters for the sample investigation in Figure 4.12. The coercivity and remanence were obtained from the SQUID measurements, the resonance fields, the effective fields and magnetocrystalline uniaxial anisotropy constants were obtained from FMR measurements.

P	$\mu_0 H_c$(mT)	M_r/M_S	H_r (mT)	H_{eff}(mT)	$\mu_0 H_c$(mT)	M_r/M_s	H_r (mT)	H_{eff}(mT)	½$\mu_0 M_S$ (1-3P) (mT)
	Applied field parallel to the axis of NWs				Applied field perpendicular to the axis of				
16%	65	0.87	150	166±10	7.1	0.05	410	166±10	160±10

According to the results, H_{eff} from FMR measurements for both orientations are equal and larger than the estimated from the formula (2.19). This deviation is attributed to a small additional second-order uniaxial anisotropy contribution (because the nanowires are not perfectly aligned, a general expression would include uniaxial magnetocrystalline anisotropy up to the second order). One contribution may arise through effects of magneto-elastic distortion produced by the membrane [42,139]. In addition, this deviation can be because of uncertainty in determining the line position. Because of the distribution of the diameter, the uncertainty of estimating porosity is considered for calculating the equation (2.19).

The FMR and SQUID measurements have been performed for Ni nanowires with the length of ~1.6μm and diameter 35 nm (Figure 4.13 a-b). The results from FMR measurement and estimated from the formula are summarized in Table 4.6. According to the results for the effective field from the measurements and from the formula a small deviation is observed. These results are in good agreement with previous works. Hysteresis curves were measured for the same sample by applying the external field parallel and perpendicular to the nanowires axis at room temperature (Figure 4.13b).
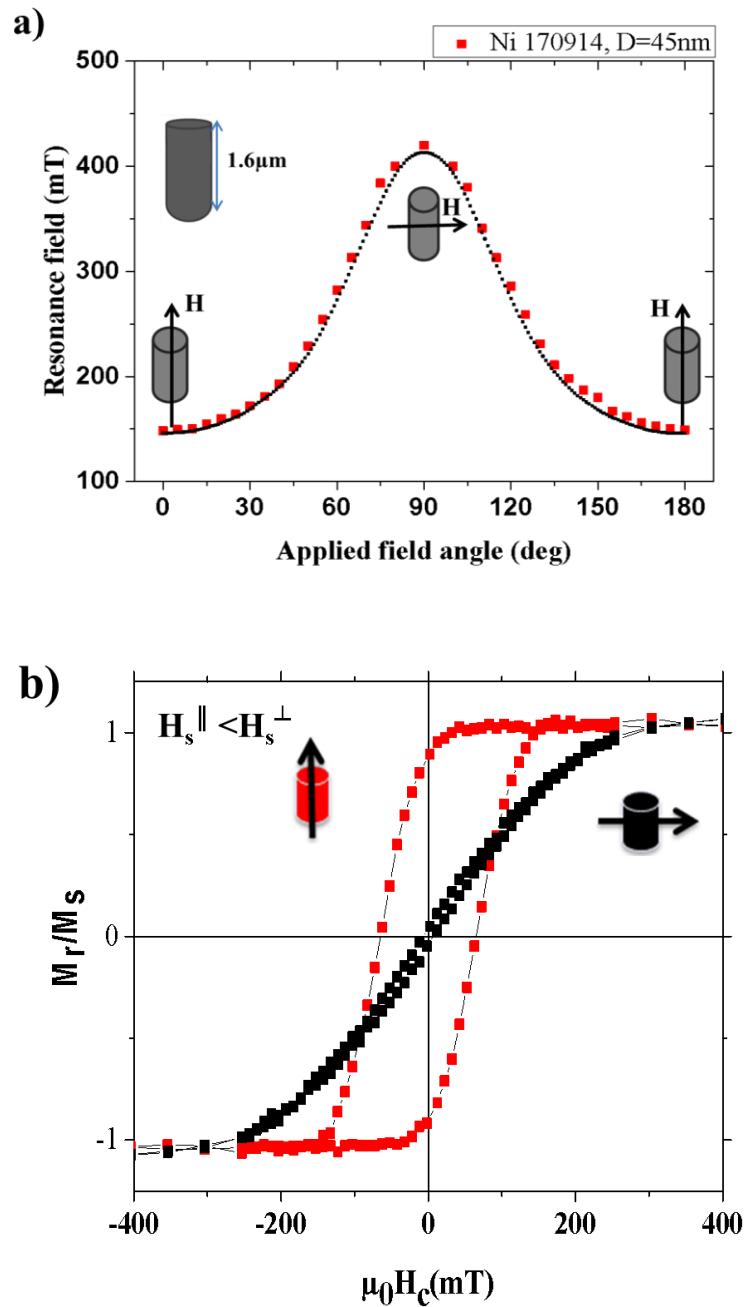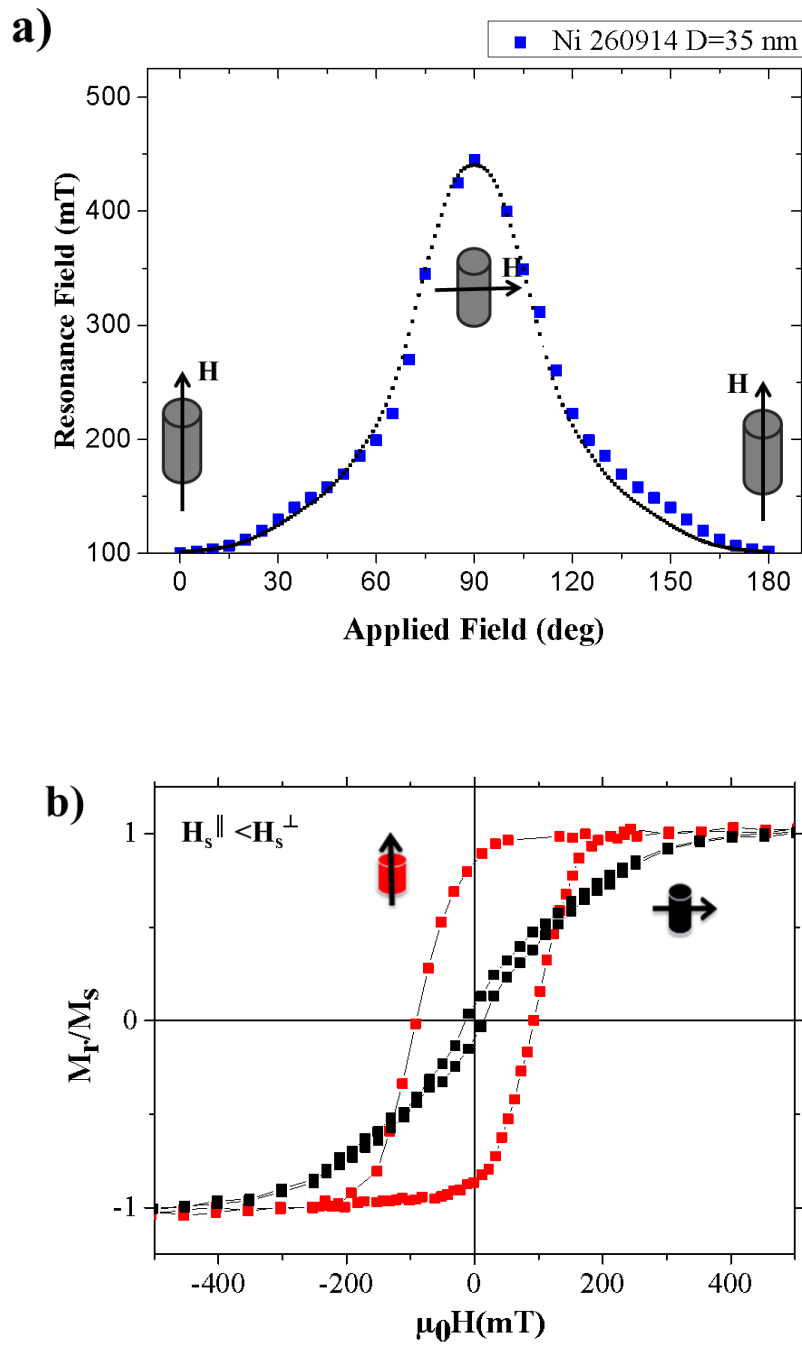
Figure 4.13 a) Angular dependence of the resonance field at 9.77 *GHz* at room temperature for pure Ni nanowires with interwire distance of 105*nm*, pore diameter 35*nm*, and with the length of ∼ 1.6*μm* and its best fit. b) Corresponding hysteresis loops measured with an applied field parallel (∥) and perpendicular (⊥) to the wires at 300*K*.

TABLE 4.6. Summary of the magnetic parameters for the sample investigated in Figure 4.13. The coercivity and the remanence were obtained from the SQUID measurements, the resonance fields, the effective fields and magnetocrystalline uniaxial anisotropy constants were obtained from FMR measurements.

P	Applied field parallel to the axis of NWs				Applied field perpendicular to the axis of				
	$\mu_0 H_c$(mT)	M_r/M_s	H_r(mT)	H_{eff}(mT)	$\mu_0 H_c$(mT)	M_r/M_s	H_r(mT)	H_{eff}(mT)	$\frac{1}{2}\mu_0 M_s(1-3P)$(mT)
10%	98	0.9	100	216±10	22	0.2	445	220±10	215±10

By comparing the results of FMR measurements for both samples, it is observed that the effective anisotropy field increases by decreasing the diameter the nanowires.

In conclusion, by increasing the porosity of the nanowires, the dipolar field increases that causes to decrease of the effective anisotropy field along the nanowires. The hysteresis loops correspond to these samples also confirm that by increasing the porosity and the dipolar interaction the coercivity and the remanence decrease. These hysteresis loops show that when the external field is applied parallel to the wires there is a low saturation field and high remanence. Whereas when the applied field is perpendicular to the wires the hysteresis loops show anisotropic behavior, a high saturation magnetization and low remanence.

4.3 Conclusions

Ni nanowires with diameters from 35 *nm* to 75 *nm* were fabricated in anodic alumina membranes by electrodeposition. SEM, TEM, EDX, SQUID magnetometry and FMR were used to analyze morphology, structure, and composition as well as their magnetic properties.

Ni nanowires with 45 *nm* diameter were synthesized as a function of the deposition potential range from -0.8 *V* to -1.5 *V* vs the reference electrode Ag/AgCl. The growth rate and the crystallinity of the nanowires were investigated. It was observed that the growth rate depends on the deposition potentials and by increasing the potentials it increases linearly, reaching 5*μm min*$^{-1}$ for -1.5 *V*. However, the length distribution for a deposition potential below -1.1 *V* was found to be smaller because of less hydrogen reduction. The synthesized Ni nanowires indicated mostly the polycrystalline nature but the crystallinity of the nanowires synthesized at -1 *V* and -1.1 *V* vs the reference electrode was better with bigger crystal grain size reached up to 50 *nm*. The crystal grain sizes for nanowires synthesized at -1.5 *V* vs the

reference electrode were in the range from 5 to 20 nm. The growth orientation of the single crystal nanowires for all samples is <011>.

In the following, the magnetic properties (the coercivity and the remanence) of the Ni nanowires embedded in the AAO membrane with interpore distance of 105 nm, with the same aspect ratio, as a function of the deposition potentials were investigated. The similar magnetic properties suggest that for Ni nanowires with fcc structure the shape anisotropy dominates on the magnetocrystalline anisotropy so the magnetic properties strongly depend on the aspect ratio, in other words on the shape anisotropy, and the magnetic dipole-dipole interactions between the nanowires. For close packing nanowires, the dipole-dipole interaction among the nanowires reduces the shape anisotropy field.

The coercivity and the magnetic saturation as a function of temperature were investigated. With increasing temperature, both decrease roughly linearly.

The magnetic properties of Ni nanowires after annealing process at $650°$ C under Ar atmosphere for 24 h were investigated. The thermal treatment caused to 55% decrease of the coercivity indicating sufficient reduction of the effective magnetic anisotropy. The coercivity of the Ni nanowires after annealing decreases due to the decrease of the vacancies and the defects inside the nanowires. Because the domain wall nucleation occurs at the vacancies so pins the magnetization and increase the coercivity. Another reason can be attributed to the contribution of magnetoelastic anisotropy of the sample due to the mismatch between the thermal expansion coefficient of Ni and alumina. The Ni nanowires during the annealing tend to expand more than the membrane result in the lateral compressive stress.

The FMR measurements of Ni nanowires embedded inside the AAO membrane, with diameters 35 nm and 45 nm (length of 1.6 μm and the interpore distance of 105 nm) were investigated. The angular dependence of the resonance field at 9.77 GHz at room temperature reveals that for both samples with different porosity the easy axis is along the wire axis. Theoretically, the value of the effective anisotropy field for an isolated Ni nanowire is given by ½$\mu_0 M_S$ with $M_s = 474{\times}10^3 \, A/m$ that is bigger than observed experimentally. The main difference arises from the dipolar interactions between the nanowires corresponding to the porosity of the membrane. Consequently, the effective anisotropy field is given by ½$\mu_0 M_S(1 - 3P)$. This leads to $\mu_0 H_{eff} = 215mT$ for Ni nanowires with 35 nm diameter and porosity 10% and $\mu_0 H_{eff} = 160 \, mT$ for Ni nanowires with 45 nm diameter and porosity 16%. Therefore, for Ni nanowires with the same interpore distance and length, by increasing the diameter, the dipolar interactions increase suggests the decrease of the effective anisotropy field.

5 Hybrids of Ni-Ag and Ni-Ag-Ni nanowires

Hybrid Ni/Ag nanowires are synthesized by potentiostat electrodeposition in porous anodic alumina templates. The process is optimized to produce a very sharp interface between the segments. The structural, magnetic, and optical properties are analyzed. The TEM study shows the optimization of the deposition process to produce very sharp interface of the segments. It is described a modification of the localized surface plasmon resonance of Ag based on coupling to ferromagnetic Ni. It is demonstrated that higher order transverse plasmon modes of the Ag segment can clearly be identified for the segmented coupled nanowires rather than for individual Ag nanowires. In addition, one high intensity plasmon peak corresponding to Ni segments is observed. At the end of the chapter, the FMR results on Ni/Ag nanowires are compared with pure Ni nanowires.

5.1 Synthesis bimetallic nanowires

For this experiment, hybrid segmented nanowires were synthesized by sequential electro-deposition using alternating baths of Ni and Ag ions [86,140]. This strategy avoids contamination from one metal into the other.

Prior to describe the details of synthesizing the hybrids of two and three segmented nanowires, synthesizing of pure Ag nanowires is described.

5.1.1 Synthesize Ag nanowires

Ag nanowires were synthesized inside the alumina templates combined with DC electrodeposition in potentiostatic mode. The electrolyte water based solution for growing Ag nanowires contains $0.03M$ $AgNO_3$ and $0.18M$ Na_2SO_3 in water [141,142].

Prior to Ag potentiostatic electrodeposition inside the membrane, linear sweep voltammetry measurement was performed to find the reduction potential for synthesizing Ag nanowires that depends on the agitation conditions, electrolyte composition, its *pH* value, and the temperature of the deposition process.

The linear voltammetry was performed at room temperature on a Ni substrate and a platinum wire was used as a counter electrode and Ag/AgCl (in 4 M KCl) as the reference electrode. Figure 5.1 represents the linear sweep voltammetry curve obtained during Ag deposition inside the membrane. In this Figure, a cathodic and an anodic peak corresponding to the deposition and dissolution of Ag are observed. Ag deposition occurred from -0.1 to -1.0 *V* where the reduction potential happened, illustrates a combination of charge and diffusion controlled processes with the nucleation of H_2 gas bubbles at high negative cathodic potentials. At less negative reduction potential the rate of the deposition is so low, while at more negative reduction potential the probability of H_2 gas evolution increases during the electrodeposition process. Consequently, there is a small interval of applied potential for the deposition of Ag nanowires. In this range of reduction potential, Ag nanowires were synthesized at -0.8 *V* vs. the Ag/AgCl as the reference electrode. Figure 5.2 shows the SEM images of the densely-released Ag nanowire arrays synthesized at -0.8 *V* vs. the reference electrode at room temperature.
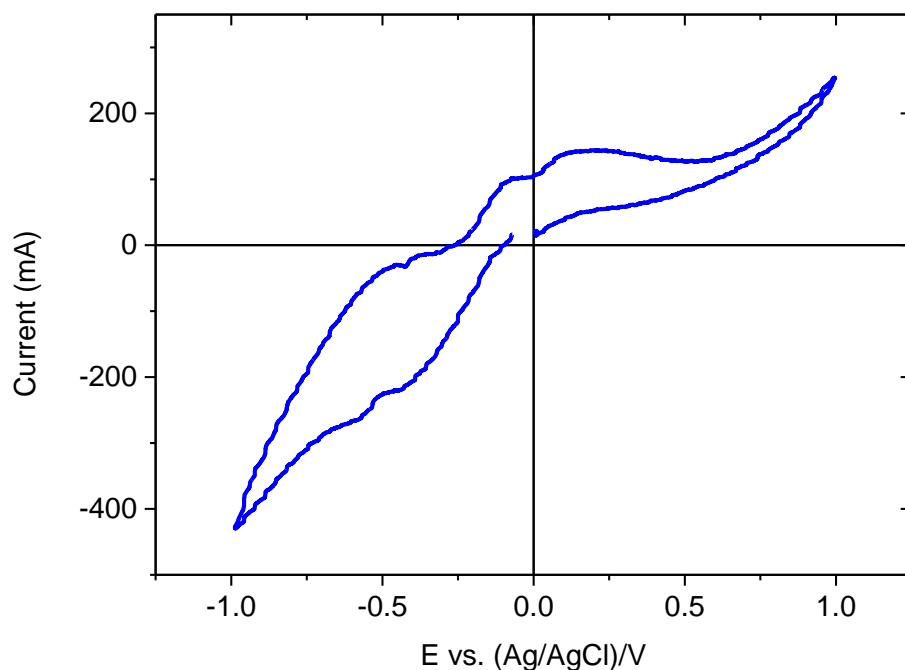

Figure 5.1. The linear sweep voltammetry curve obtained during Ag deposition on a Ni substrate. The reduction of Ag ions occurred from -0.1 to -1.0 *V*.
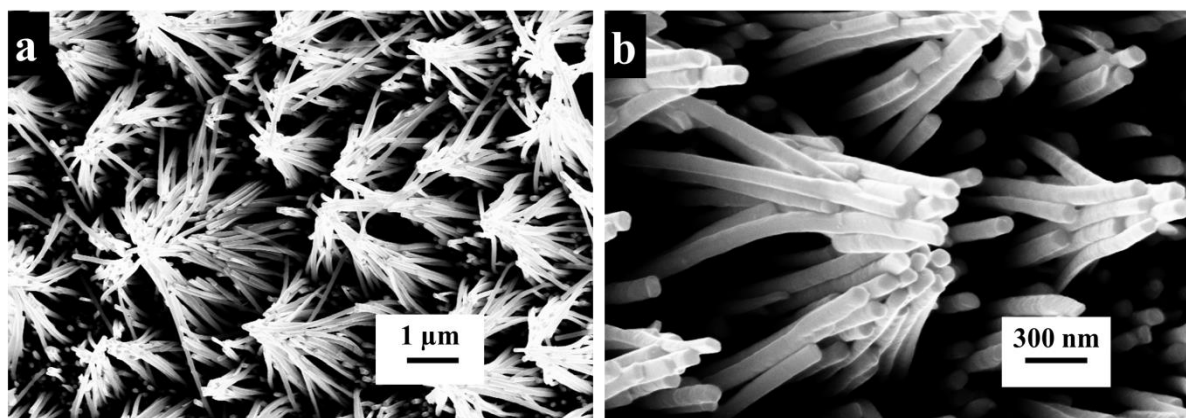
Figure 5.2. a-b) SEM images of silver nanowires after removing the AAO membrane.

Then for controlling the length of the nanowires corresponding to the formula of Faraday (eq. 2.43) and by considering the density of Ag, $\rho_{Ag} = 10.5 \ g/cm^3$, and molar mass, M_{Ag}=107.868 *g/mol,* adequate charge for desired length was calculated and by controlling the charge passed through the channels during the potentiostatic electrodeposition it was possible to synthesize nanowires with certain length. Figure 5.3 a-b) shows the SEM images of the top view of the released Ag nanowires with length 430 *nm*. It reveals a precise control on the length of the Ag nanowires that is desired for synthesizing the hybrids of Ni and Ag nanowires with a short length of Ag.

Figure 5.3. a-b) The top view SEM images of released Ag nanowires with length 430 *nm* and pore diameter 75 *nm* on Si substrate.

The synthesized Ag nanowires were characterized using XRD analysis. In Figure 5.4 XRD measurement confirms the presence of the Ag nanowires embedded inside the membrane. The pattern shows distinct diffraction peaks corresponding to a face-centered cubic (fcc)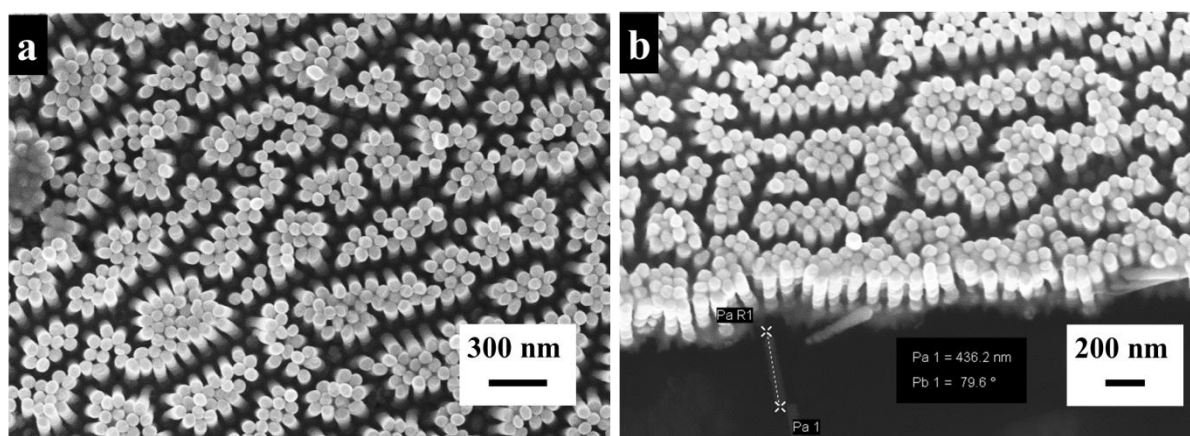 structure oriented along [111], [200] and [220] directions so reveals a polycrystalline nature of the nanowires with preferential orientation in <110>.
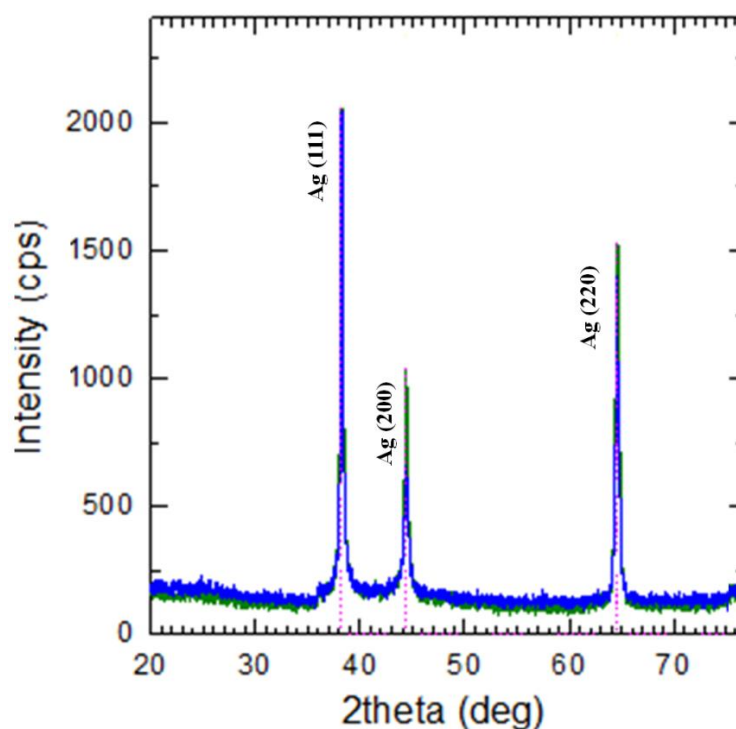
Figure 5.4. The XRD pattern of Ag nanowires. The pattern shows distinct diffraction peaks corresponding to a single-phase face-centered cubic (fcc) structure with preferential orientation in <110>.

5.1.2 Synthesis of hybrids Ni-Ag nanowires

Hybrids of Ni-Ag nanowires were successfully synthesized using two separate electrolyte baths for Ag and Ni at -0.8V and -1 V vs the reference electrode, respectively, into the pores of anodized aluminum oxide membrane. In these experiments, the membranes with a pore length of 40 μm and adjustable pore diameter between 35 nm and 80 nm were used.

Figure 5.5 illustrates the whole process for synthesizing segmented nanowires and development of releasing nanowires. First, the bath of one metal was used to synthesize the first segment. Then the sample was completely rinsed to prevent the presence of the contamination from previous precursor for the next step. It is worth nothing that for obtaining sharp interface

of different segments, using an AAO membrane with shorter thickness (less than 40 μm) is more suitable for avoiding of any trace of the metal in the next segment. It should be taken into account that rinsing the sample after every step of electrodeposition leads to oxidation the tip of each segment but even with a thin layer of oxide the nanowires are synthesized with very well interface.

A main challenge of releasing the segmented nanowires is that upon the process of dissolution of the membrane and dispersing the nanowires some of the interfaces of the bimetallic nanowires are broken.
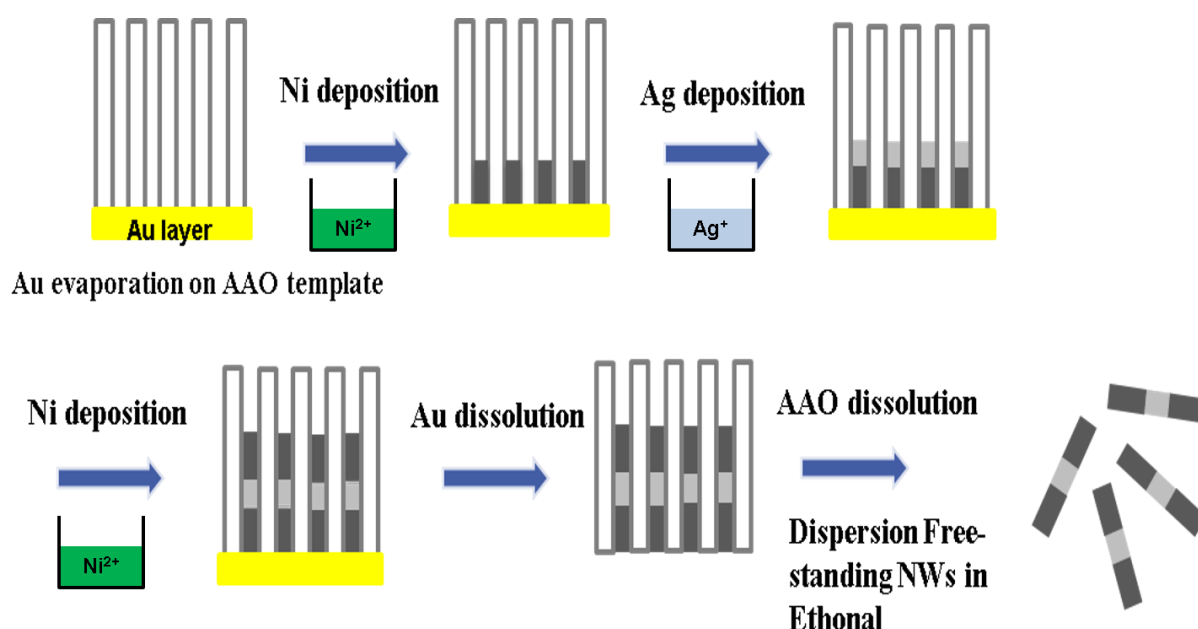
Figure 5.5. Schematic representation of the synthesis of bimetallic nanowire arrays by sequential electrodeposition of Ni and Ag metals into porous alumina membrane and the development of releasing nanowires.

5.2   Morphology and crystalline structure

Scanning Electron Microscopy (SEM) and transmission electron microscopy (TEM) were used to characterize the morphology and the crystallinity of the synthesized nanowires. Figure 5.6 a) shows the SEM image of the cross-section of the released three segmented Ag-Ni-Ag nanowire arrays after removing the membrane that are identified by their dark and light contrast and b) EDX spectrum of the interface of Ag and Ni that confirms the present of them.
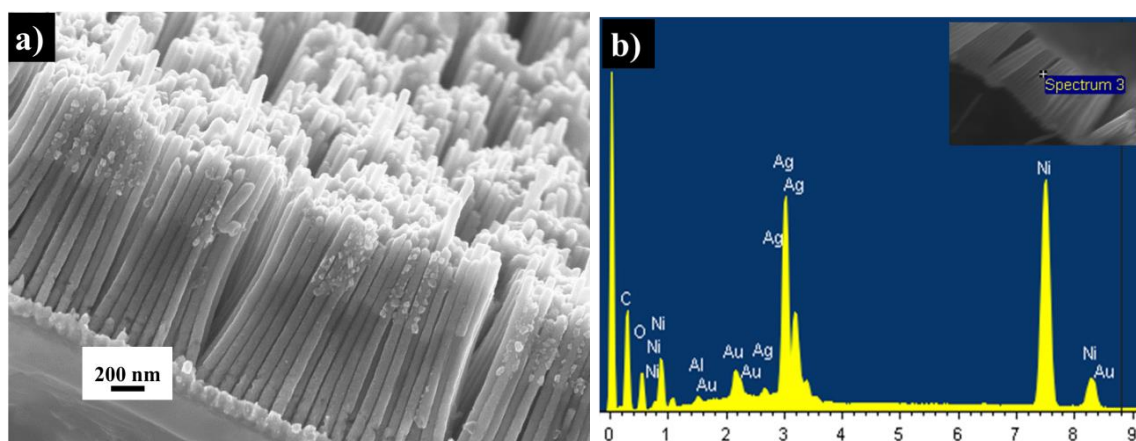
Figure 5.6. a) and b) SEM image of released three segmented Ag-Ni-Ag nanowires and EDX spectrum of one area (the inset presents the area for EDX spectrum), respectively.

To analyze the nanowires with TEM, the released nanowires were dispersed on the surface of the TEM grid. Figure 5.7 a) shows a TEM image of Ni-Ag-Ni nanowires in which Ag and Ni segments are identified by their light and dark contrast, respectively due to different scattering strength for Ni and Ag. In addition, TEM image of Ni segments shows dark-light contrast to different electron diffraction conditions displays various crystalline grains. In Figure 5.7 b) HRTEM image focuses on one junction of three segmented Ni/Ag with three regions of Ni (1), junction of Ag-Ni (2), and Ag (3). Region (1) is not exactly in diffraction position. A 2-3 nm thick surface layer is visible that can be ascribed to oxide self-passivating the metal cores for both Ni and Ag. The SAED patterns of these three regions are shown on the right side of Figure 5.7 b). The SAED pattern shows two fcc structures with different lattice parameters, which can be ascribed to Ni (1) and Ag (3). Most interesting, the interface (2) shows two sets of diffraction patterns of both Ag, and Ni. Those have a lattice mismatch of $(0.4086-0.3525$ $nm)/0.4086$ $nm = 13.7\%$ fitting to bulk Ag and Ni, respectively, which can be respectively indexed to pure Ag and Ni. However, in generally the SAED pattern indicates the polycrystalline nature for Ni segments with a grain size ranging from 5 to 50 nm.

Figure 5.7 c) presents distribution of elements along a nanowire (see inset) consists of Ni and Ag parts with a very sharp interface by considering a transition region of at most 5 nm. Figure 5.7 d) shows the overall elemental distribution of the sample that is measured by EDX. Besides some C arising from the C-coated TEM grid as indicated by the peak around 0.28 keV, spectral lines from Ag and Ni provided the success of the electrodeposition and complete removal of the membrane.
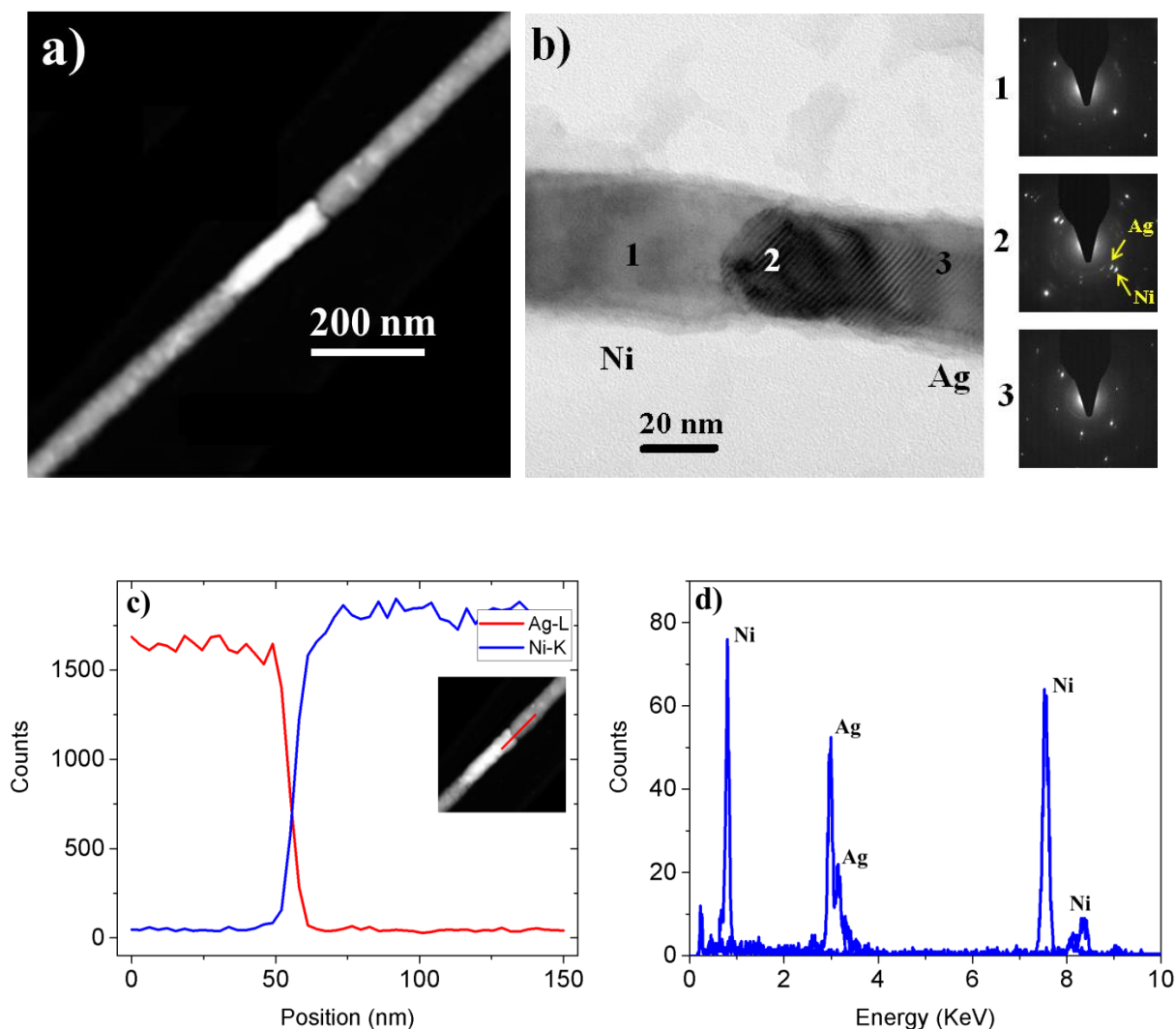
Figure 5.7 a) STEM image of heterostructure section of Ag-Ni-Ag nanowires and Ag and Ni segments are identified by their light and dark contrasts, b) HRTEM image of interface of single Ag-Ni nanowire; insets: SAED patterns present the crystallinity of the segments with FCC structures and the SAED pattern of the interface shows two sets of diffraction patterns (4.0862-3.525)/4.0862=13.7%) which can be respectively indexed to Ag and Ni. c) and d) EDX spectrum of the Ag-Ni nanowires, the inset presents the area for EDX spectrum.

5.3   Optical characterization

The optical spectroscopy was used to characterize the optical properties of the synthesized nanowires. We measured the optical spectra of the nanowires after release from the AAO membrane and dispersion in ethanol. Figure 5.8 presents the absorbance spectrum of the Ag NWs with the length of 2 μm and diameter 40 ($\pm$5) nm, after normalization to a reference

spectrum of the identical cuvette filled with pure ethanol. This spectrum displays a single peak at wavelength 400 *nm* that can be ascribed to the transverse resonance described in detail in section 2.2.5. The longitudinal resonance mode appears at a longer wavelength that is not observable within this range of the investigated spectral window. Many works have been done to investigate the effect of the shape of silver nanostructures [16,61,140-148] on optical properties. Therefore, the investigation of optical properties of Ag nanowires as a function of aspect ratios was not interested.
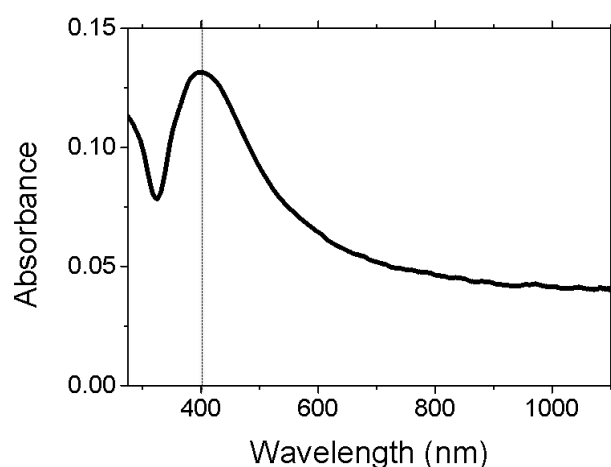
Figure 5.8. Optical absorption spectra of Ag nanowire arrays with the length of 2 µm and diameter 40 (±5) *nm* in ethanol solution.

In this thesis, the aim is to investigate the effect of Ni as a ferromagnetic metal on optical properties of Ag nanowires. In this study, the length of Ni segments has been chosen asymmetric due to the possibly achieve a direction dependent optical properties. Figure 5.9 shows the SEM image of hybrid of Ni-Ag-Ni nanowires with 75 (±5) *nm* diameter. Besides some agglomerates, the Ni-Ag-Ni junctions are clearly visible in the two central NWs. The length of the first and the second segment of Ni are 560 (±50) *nm* and 1150 (±150) *nm*, respectively. The length of the Ag segment is short 210(±20) *nm* probably for longer segment the effect of Ni is not significant. The error bars are estimated by measuring the length of some nanowires.
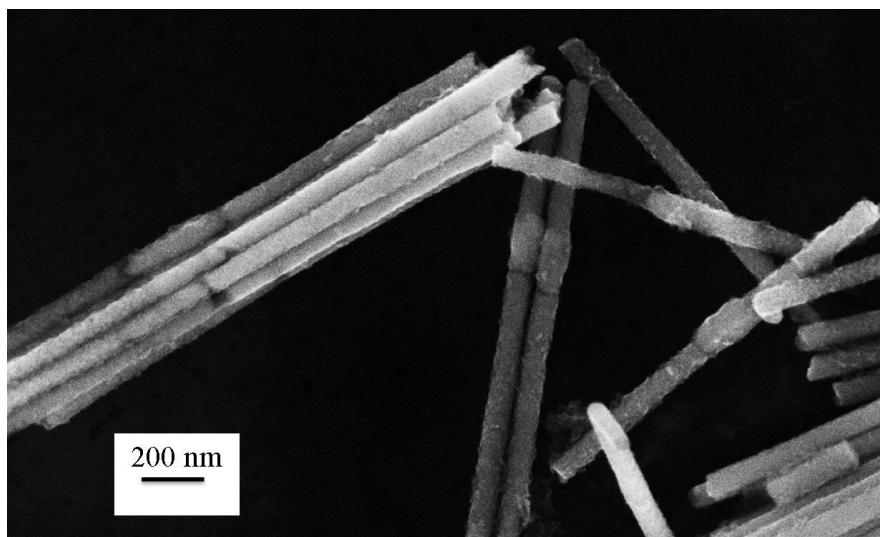
Figure 5.9. SEM image of hybrid of Ni-Ag-Ni nanowires with 75 *nm* diameter. The length of Ag segment is 210(±20) *nm* and the first and the second segments of Ni are 560 (±50) *nm* and 1150 (±150) *nm*, respectively.

Then, the optical spectra of these hybrid nanowires were measured to investigate the effect of Ni segments on LSPR properties of Ag segment (Figure 5.10). Three distinct peaks are observed at 313 *nm*, 366 *nm*, and 438 *nm* in the optical spectra. Some small jumps appear in the spectrum due to the switching the filters of the device as indicated by red lines. The LSPR transverse dipole mode of Ag is found at 438 *nm*. One noticeable peak at 366 *nm* is observed corresponding to the higher order of transvers LSPR mode. According to the previous work of the optical spectra of single component Ag nanorods (with diameter 75 (±5) *nm* and the length between 130 *nm* to 393 *nm*), the transverse mode was appeared at 450 *nm* and the higher order of the transverse mode appeared as a very small shoulder at 375 *nm* [143].

Consequently, it is demonstrated that the transverse localized surface plasmon resonance mode of the Ag segment changes by 12 *nm* due to the contact to ferromagnetic Ni. It is also revealed that higher order transverse plasmon modes of the Ag segment can clearly be identified as a distinct peak at 366 *nm* in the hybrid of Ag/Ni nanowires rather than for individual Ag nanowires that appeared as a shoulder. The higher-order LSP modes in general can be observed for nanorods with dimensions larger than L ≥ 250 *nm*, when D ≈ 80 *nm* [14]. Therefore, it seems that coupling Ni as ferromagnetic material with Ag modifies the optical response of Ag.

The longitudinal dipole mode is not observable within this range of the investigated spectral window.

Another interesting outcome of this study is the narrow LSPR mode with high intensity at 313 *nm* which is related to Ni segments [15]. A broad peak for Ni is expected due to the high damping in Ni whereas a narrow peak with high intensity is observed. It may be because of the Ag segment as noble metal on optical properties of Ni parts. Consequently, the Ag segment participates in the surface plasmon coupling between two Ni end-parts. This combination of ferromagnetic metals and noble metals can be useful for a novel magneto optical surface plasmon resonance sensor [149].
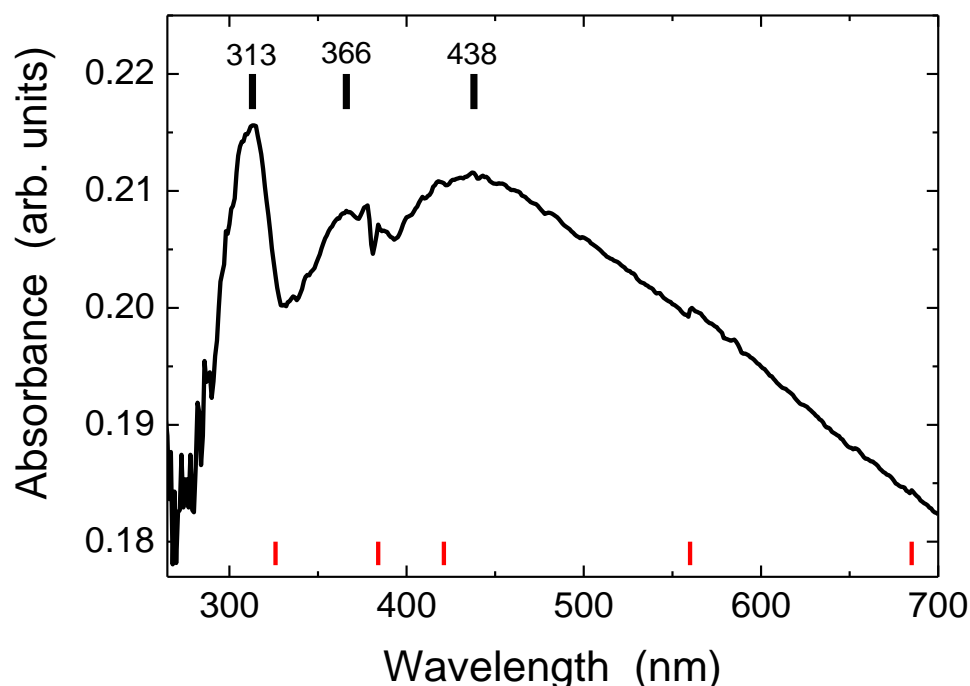
Figure 5.10. Optical absorption spectra of Ni- Ag-Ni nanowires in ethanol solution. The peak appears at 383 *nm* is related to the instrument.

In this work, it is demonstrated that higher order transverse plasmon modes of the Ag segment can be identified clearly in the Ag/Ni coupled nanowires rather than for individual Ag nanowires. In addition, a narrow peak with high intensity of Ni segments is observed which for long Ni nanowires is not visible.

In previous works, Sridharan et al. reported that the effective nonlinear absorption in Ni-Ag and Fe-Ag bimetallic nanoparticles is higher than that of pure Ag [150]. In addition, Wang et al. demonstrated that the optical absorption peaks in core-shell Co-Ag nanoparticles appear blue-shifted with increased Co core size by keeping the nanoparticle size constant [151].

5.4 Magnetic characterization

5.4.1 SQUID and FMR measurements

The purpose of these measurements is to compare the magnetic properties of pure Ni and hybrid of two segmented Ni-Ag nanowires to investigate the effect of Ag as nonmagnetic part on magnetic properties of Ni. In these experiments, the membranes with 40 μm thickness and 45 nm pore diameter were used. In general, first Ni was synthesized inside two membranes. Then, after removing one sample, the process of depositing Ag electrochemically was continued. The process of preparing the samples for magnetic measurements is described in detail in chapter 3.

Figure 5.11 shows the SEM images of high density released nanowires with diameter 45 nm a) pure Ni nanowires with the length of 1600 (±200) nm and b) hybrids of Ni/Ag nanowires with the length of 1600 (±200) nm and 200 (±50) nm for Ni and Ag, respectively. Figure 5.11 c) presents the SEM image of cross section of hybrid of Ni/Ag nanowires embedded in the membrane with low distribution of length, indicated the high quality of the synthesizing the nanowires.
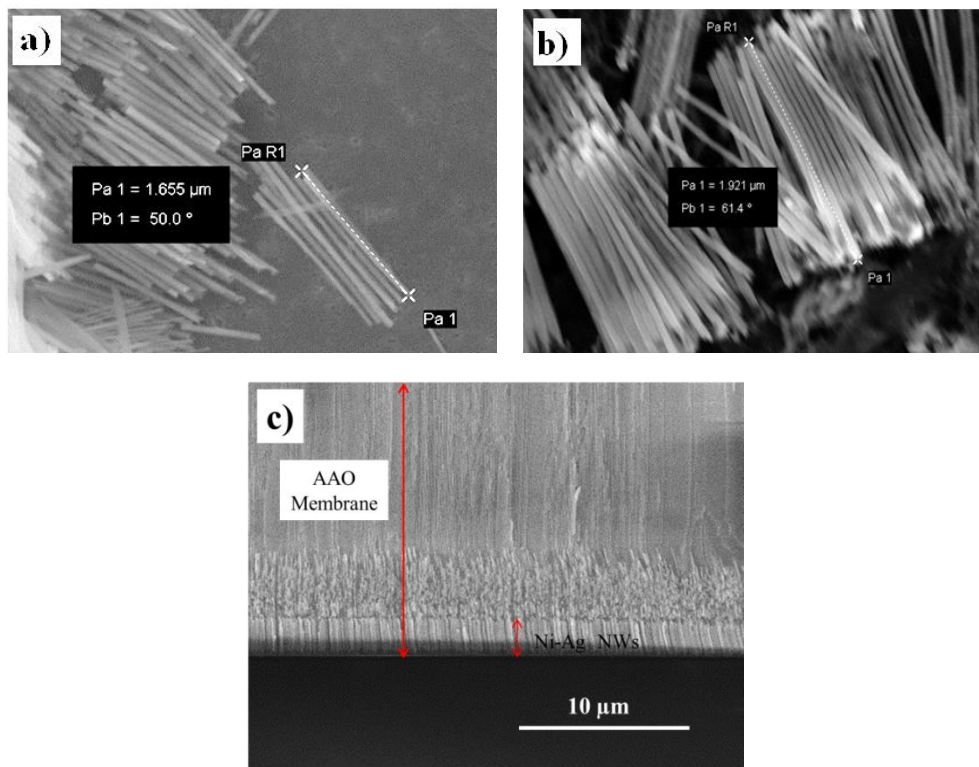
Figure 5.11. a) SEM image of released Ni nanowire arrays. SEM images of hybrid of two segmented Ni-Ag nanowire arrays   b) dispersed on a Si substrate and   c) embedded inside the membrane with low distribution of length.

SQUID and FMR measurements were performed for the hexagonally-ordered nanowires embedded inside the membrane. Figure 5.12 a) and b) shows the angular variation of the FMR signal at 9.77 *GHz* at room temperature of hybrids of Ni/Ag nanowires and pure Ni nanowires, respectively. The angular variation of these spectra is characteristic of an easy axis along the wire length for both samples. It is observed that for both samples the minimum of the resonance filed is occurred when the external magnetic field is parallel to the wires's axis. In addition, the maximum values for the resonance filed for both samples are occurred when the applied field is perpendicular to the wire's axis. According to the FMR spectra, the effective anisotropy fields can be estimated using equations (2.21) and (2.22). In theoretical approach, the effective field is obtained from equation (2.20). The results are summarized in Table 5.1.

It is observed that the effective anisotropy field from two samples are not the same and there is a big deviation between them. When the applied field is parallel and perpendicular to the wires's axis, the effectvie field for sample of Ni-Ag nanowires and for sample of Ni nanowires are 90 *mT* and 166 *mT*, respectively.

Figure 5.12 c) and d) shows the hysteresis loops of sample Ni-Ag and Ni nanowires, respectively that there is slightly difference between their coercivity and their remanance.
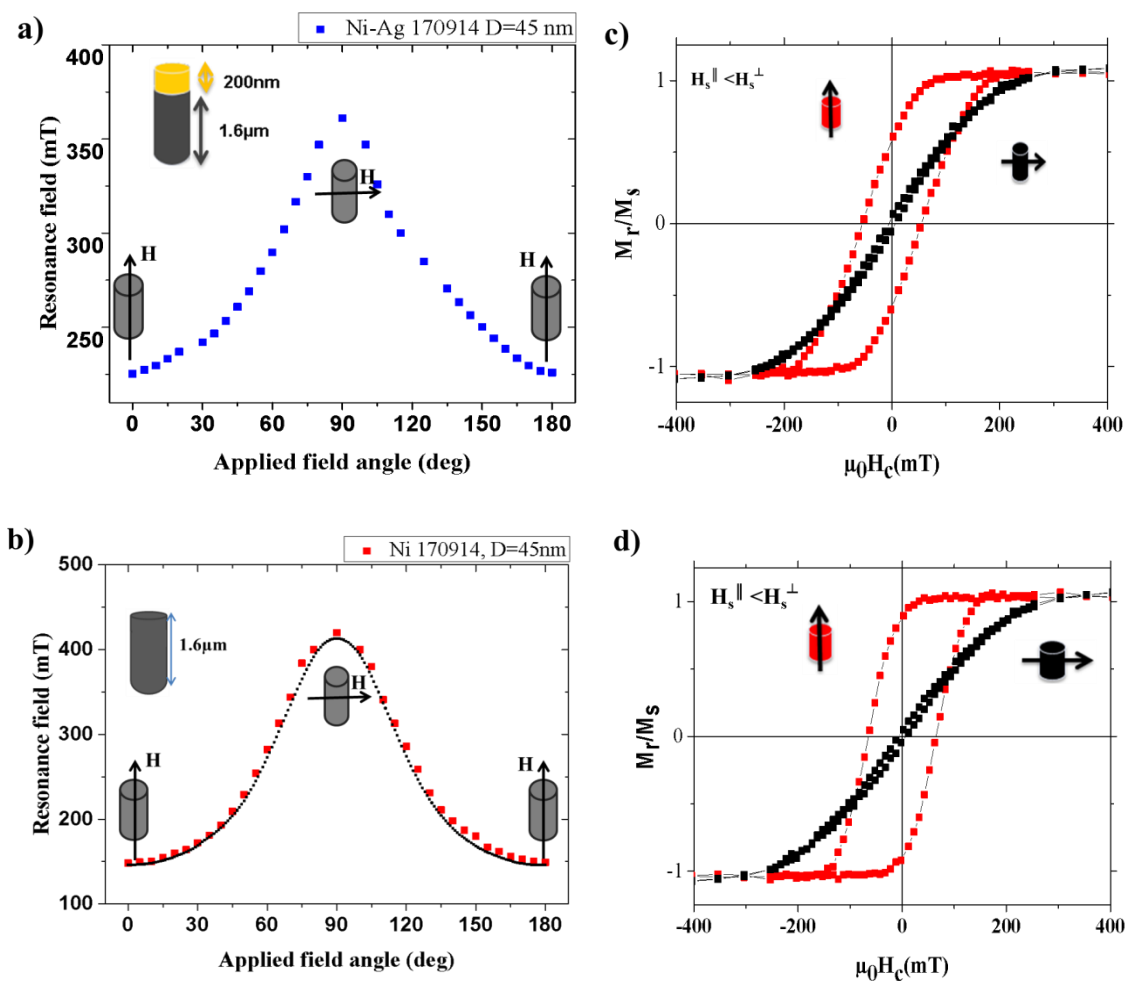
Figure 5.12. Observed angular variation of the FMR signal at 9.77 *GHz* at room temperature for   a) hybrid of Ni/Ag nanowires and   b) pure Ni nanowires with interwire distance of 105 *nm* and pore diameter 45 *nm*, the constant length of Ni segment~ 1.6 *μm* and the length of Ag segment ~ 200 *nm*. SQUID hysteresis loops of the same samples; c) hybrids of Ni/Ag nanowires and   d) Ni nanowires, measured with an applied field parallel and perpendicular to the wires at 300*K*.

TABLE 5.1. Summary of the magnetic parameters for two samples described in Figure 5.12.

	P	$\mu_0 H_c$(mT)	M_r/M_S	H_r (mT)	H_{eff}(mT)	$\mu_0 H_c$(mT)	M_r/M_S	H_r (mT)	H_{eff}(mT)	$\frac{1}{2}\mu_0 M_S$ (1-3P) (mT)
		Applied field parallel to the axis of nanowires				Applied field perpend. to the axis of nanowires				
Ni-Ag	16%	55	0.6	220	90±10	6.3	0.05	360	90±10	160±10
Ni	16%	65	0.87	150	166±10	7.1	0.05	410	166±10	160±10

In addition, FMR and SQUID measurements were performed for another two samples of two segmented of Ni-Ag nanowires and pure Ni nanowires with diameter 35 *nm* and the interwire distance of 105 *nm*. The length of the synthesized nanowires was similar with two previous samples, Ni nanowires were synthesized with the length of 1600 (±200) *nm* and Ni-Ag nanowires were synthesized with the length of 1600 (±200) *nm* and 200 (±50) *nm* for Ni and Ag, respectively. Figure 5.13 a-b) shows SEM images of high density released Ni and Ni-Ag nanowire arrays on Si substrate, respectively.
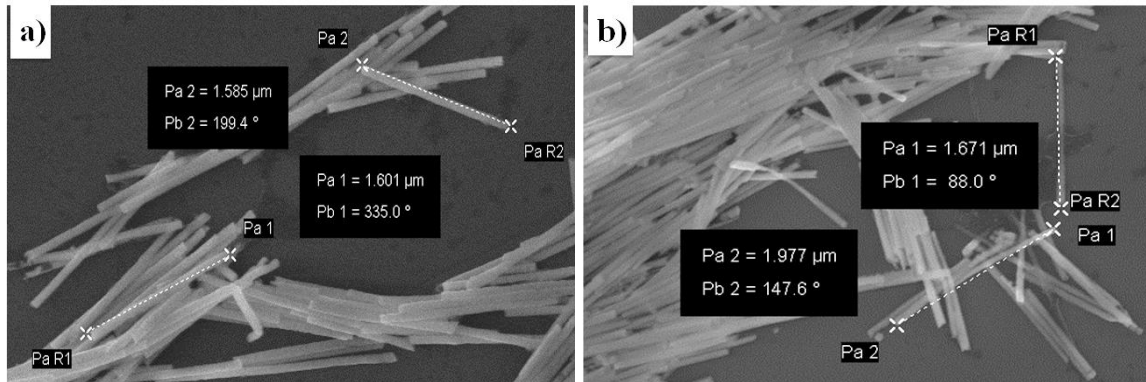
Figure 5.13. SEM images of released a) Ni 271014 and b) Ni-Ag 271014 nanowires on Si substrate, respectively.

Figure 5.14 a-b) shows the angular variation of the FMR signal at 9.77 *GHz* at room temperature for these two samples: Ni-Ag and Ni nanowires, respectively. The angular variation of these spectra is characteristic of an easy axis along the wire length for both samples.

It is observed that the value of the effective field H_{eff} for the sample of Ni-Ag nanowires is around 80 *mT*, while for the sample of Ni nanowires is around 215 *mT*. For both samples the minimum of the resonance filed was occurred when the external magnetic field was parallel to the wires's axis. The FMR results were summarized in Table 5.2. The decrease of the resonance frequency in the hybrid of Ni-Ag indicates the reduction of the effective uniaxial anisotropy field.

Since the angular variation of Ni-Ag nanowires is not fit to the equation considered for Ni nanowires so this deviation can be attributed to an additional higher order uniaxial anisotropy contribution (up to the forth order).

It is likely that for bimetallic of Ni-Ag nanowires, the presence of Ag as a diamagnetic material effects on the dipole interactions among the nanowires results in reduction of the effective uniaxial anisotropy field. Additionally, this deviation may arise through effects of strain produced by Ag atoms on the interface of Ni and Ag. However, very small fraction of the total Ni atoms is involved with Ag nanowires.

Morever, it is important to point out that the mechanism of Ni nanowires growth followed by Ag nanowires growth in the AAO membrane is complex and any explanation mechanism can be speculative. During the process of Ag deposition, electromigration inside the Ni segment might occur which may change the crystallinity and consequently the magnetism of the Ni part. According to the initial current density during electrodeposition for the sample with 45 nm diameter, 315 A/m^2, that influences the crystallinity of the Ni nanowires. However, the magnetocrystalline anisotropy of Ni nanwoires is very low.
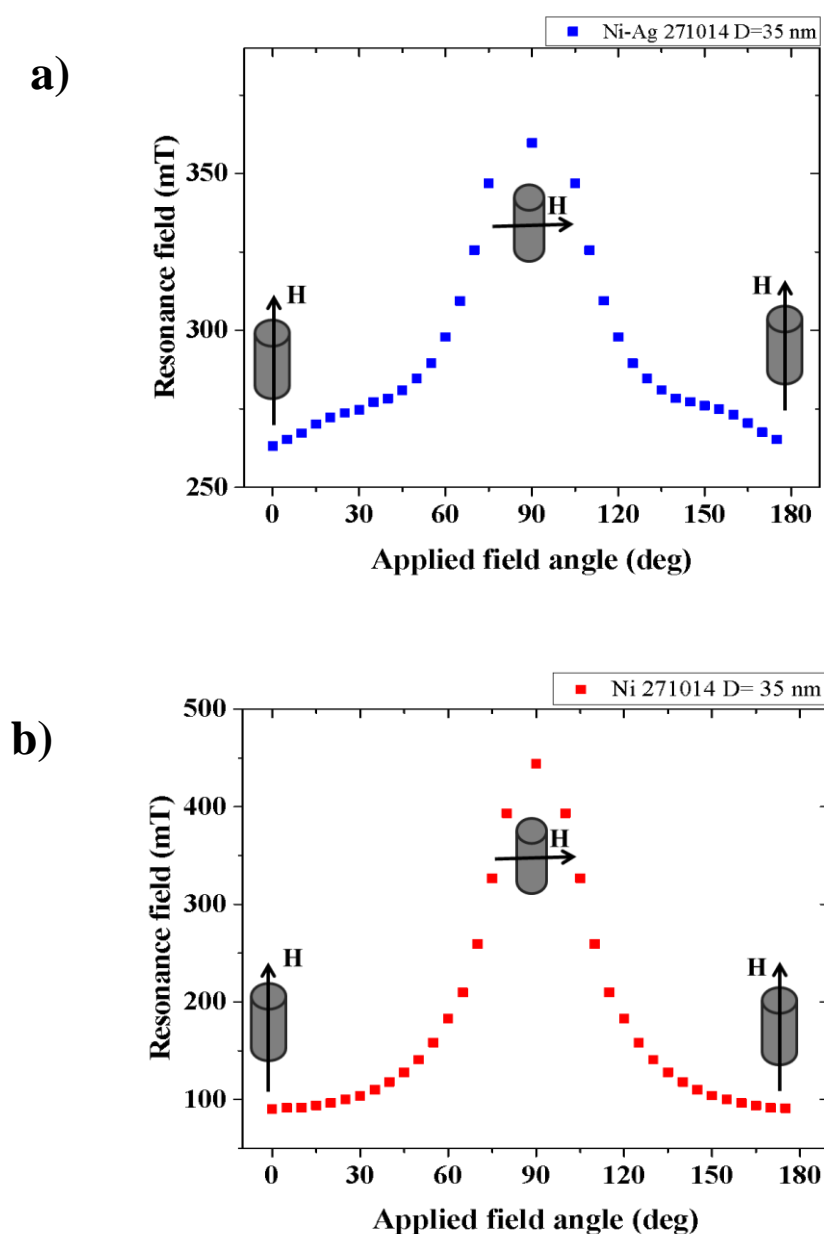

Figure 5.14. Observed angular variation of the FMR signal at 9.77 GHz at room temperature for two samples hybrid of Ni-Ag NWs and pure Ni NWs with interwire distance of 105 nm and pore diameter 35 nm, the constant length of Ni segment~ 1.6 μm with length of Ag segment ~ 200 nm.

TABLE 5.2. Summary of the magnetic parameters for two samples that were described in Figure 5.14.

Sample	P	Applied field parallel to the axis of NWs		Applied field perpendicular to the axis of NWs		$\frac{1}{2}\mu_0 M_s(1\text{-}3P)$ (mT)
		H_r (mT)	H_{eff} (mT)	H_r (mT)	H_{eff}(mT)	
Ni-Ag	**10%**	255	60±10	360	80±10	215±10
Ni	**10%**	100	215±10	450	225±10	215±10

In order to investigate the effect of dipolar interaction on FMR measurements, hybrid of Ni-Ag nanowires with diameter 75 *nm* and interpore disance 105 *nm* were synthesized with the same length of the previous samples, 1.6 *μm* for Ni part and 200 *nm* for Ag part. Figure 5.16 shows the angular variation of the FMR signal at 9.77 *GHz* at room temperature for the sample. The angular variation of the spectra is characteristic of an easy axis perpendicular to the wire's axis because the minimum of the resonance field was occurred when the external magnetic field was perpendicular to the wire's axis (265 *mT*) while the maximum of the resonance field was occurred when the external magnetic field was parallel to the wire's axis (395 *mT*).

In fact, upon increasing the porosity of the membrane, the nanowires are brought closer to each other, the decrease of the resonance field in the parallel case and the corresponding increase in the perpendicular case represents that the effective anisotropy field is reduced as the dipolar interactions among the nanowires increases. In addition, the dipolar interaction among the nanowires overcomes on the shape anisotropy so the easy axis is expected to be perpendicular to the wires axis.

The calculated magnetic parameters are summarized in Table 5.3. The estimated effective anisotropy fields from FMR measurements were -77 *mT* and -118 *mT* when the applied field was parallel and perpendicular to the wire's axis, respectively. The sign of negative for the effective field confirms that the direction of the easy axis is perpendicular to the wire's axis.
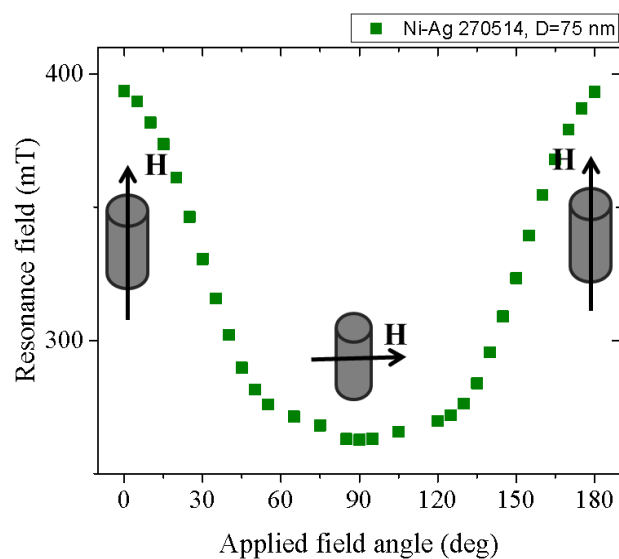
Figure 5.15. Observed angular variation of the FMR signal at 9.77 *GHz* at room temperature for hybrid of Ni-Ag nanowires with interwire distance of 105 *nm* and pore diameter 75 *nm*, the constant length of Ni segment~ 1.6 *μm* with length of Ag segment ~ 200 *nm*.

TABLE 5.3. Summary of the magnetic parameters for two samples that were described in Figure 5.15.

Sample	P	$H_r^{\parallel}$ (mT)	$H_{eff}^{\parallel}$ (mT)	$H_r^{\perp}$ (mT)	$H_{eff}^{\perp}$ (mT)	$2\pi M_s$ (1-3P) (mT)
Ni-Ag	46%	395	-77	265	-118	-118±10

Corresponding to the results for three samples of Ni/Ag nanowires it seems that by increasing the diameter, the deviation between the experimental values and the calculated values is less. Since the initial current densities during the process of Ag deposition for the samples of Ni/Ag nanowires with 45 *nm* diameter and 75 *nm* were 315 A/m^2 and 60 A/m^2, respectively so it might be proved the speculation of the effect of electromigration on the crystallinity of the Ni part [152].

5.5   Conclusions

In this work hybrid of Ni/Ag nanowires were successfully fabricated in anodic alumina membranes by electrodeposition. SEM, TEM and spectrometer are applied to analyze morphology, structure, and composition as well as their optical properties.

According to the optical properties of the hybrid of Ag and Ni nanowires, the transverse localized surface plasmon resonance mode of Ag shiftes by 12 *nm* at wavelength 438 *nm*. It is observed that higher order transverse plasmon modes of the Ag segment can be identified as a distinct peak at 366 *nm* in the Ag/Ni nanowires than for individual Ag nanowires that a small shoulder is appeared at 375 *nm*. In addition, a narrow peak with high intensity of Ni segments at 313 *nm* is observed that is not visible for Ni with long length.

The magnetic properties of Ni/Ag nanowires embedded inside the membrane with the same length and different diameters so different porosity have been investigated using FMR measurement. It is observed that the uniaxial anisotropy effective fields estimated experimentally for pure Ni and hybrid of Ni/Ag nanowires are different and by decreasing the nanowire diameter this deviation is more. It is likely that for bimetallic Ni-Ag nanowires, Ag as a diamagnetic material effects on the dipole interactions among the nanowires results in the reduction of the effective magnetic anisotropy of the Ni-Ag nanowires. Another assumption arises from the effect of electromigration inside the Ni part during the deposition of Ag part that might be changes the crystallinity of the Ni part. In addition, this deviation can be attributed to an additional higher order anisotropy contribution (up to the fourth order).

6   Ni capped Ag nanohybrids

Here, an innovative and reproducible fabrication method for synthesizing and designing of complex multicomponent nanostructure, Ni capped Ag nanohybrids, is investigated. Using a multi-step process combining electrocehmical deposition and partly removal of the AAO membrane. Well-aligned and free-standing Ag nanowires are achieved by the partly removal of the AAO membrane, subsequently, the free-standing Ag nanowires are capped by Ni electrochemically. In the following, the morphology of such nanohybrids will be discussed.

6.1   Introduction

In general, several methods are used for synthesizing heterojunctions, particularly, core/shell from different materials [86, 94]. Multicomponent nanostructures have been shown to reveal increased catalytic activity and more plasmonic tunability than their single structures [153,154].

In this thesis, it is focused on synthesizing core/ shell heterojunctions based on membranes by combining electrochemical process using two different approaches [86]. In one approach, synthesizing nanowires inside the pores electrochemically and then chemically functionalizing the nanowires with a shell [155-157]. In the second approach, the inner walls of the pores are coated layer by layer and then electrochemically filled [158-164].

Particularly, K. Sridharan et al. [150] reported synthesizing of the Ag-Ni bimetallic using chemical method. S. Senapati et al. [13] synthesized Ni/Ag core-shell nanostructure using a microemulsion template with wet chemical reduction.

In addition, Ag/Ni core/sheath nanowires have been synthesized using an anodic aluminum oxide template method and combined with electrochemical deposition of Ni [165] as

well as using a polyol-based method [166]. However, after synthesizing Ag nanowires and removing the membrane completely, the Ag nanowires agglomerated.

In this work, by synthesizing Ag nanowires followed by partial removal of the AAO membrane, free-standing Ag nanowires above the membrane are obtained. Consequently, the released nanowires above the membrane can be coated by Ni electrochemically. This method leads to a new geometry of heterojunctions of two different metals. One of the advantages of using this approach is to synthesize bimetallic core/shell wires with a pure bottom. In this case, one can compare the plasmonic properties of silver with the part that covered with Ni to obtain the effects of Ni on optical properties of silver. It would be possible to tune the magnetic properties of Ni and optical properties of Ag with such structure. The synthesized partial core-shell nanowires were analysed with SEM and EDX.

6.2   Synthesis of Ni capped Ag nanohybrids

This experiment includes three main procedures: 1) synthesizing Ag nanowires inside the membrane with desired length and diameter; 2) obtaining free-standing Ag nanowires after the partial removal of the anodic alumina membrane while the rest of the nanowires remain inside the membrane; 3) coating the free-standing Ag nanowires above the membrane by Ni electrochemically (Figure 6.1). The first step, synthesizing Ag nanowires inside the membrane electrochemically, is completely described in chapter 5 and here, the focus is on procedures 2) and 3).
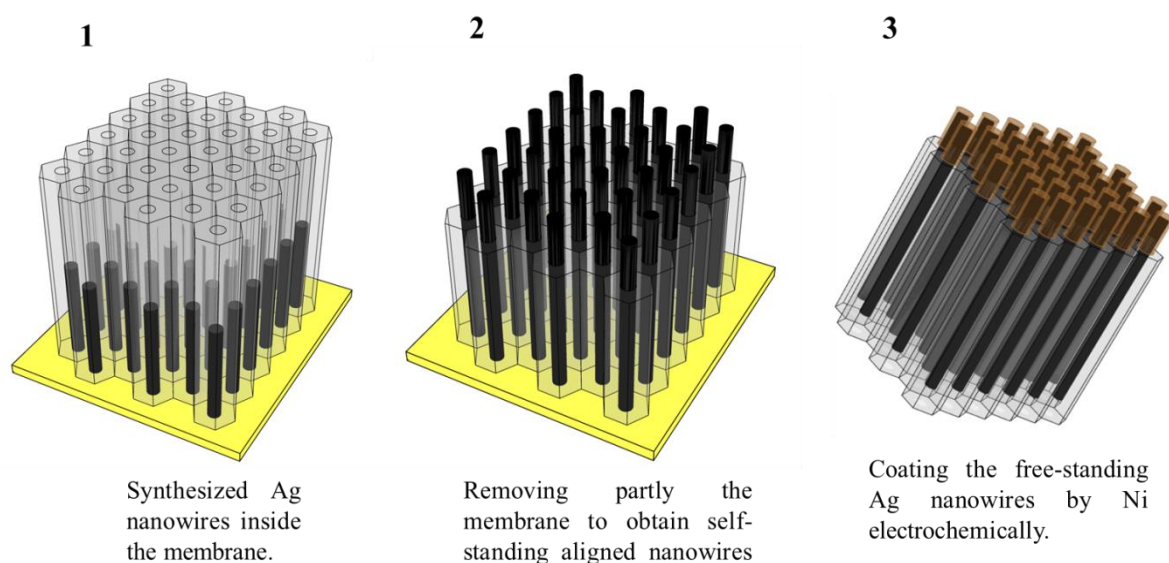
Figure 6.1. 3D schematic representation of the process of the synthesizing Ni capped Ag nanohybrids, including of 3 steps. Step (1) shows the synthesized Ag nanowires inside the membrane [schematic 1 from PhD thesis of Sara Liébana-Viñas, 2015]. Step 2 represents the partial removal of the membrane to obtain aligned Ag nanowires. Step 3 illustrates the sample after coating the released part of the Ag by depositing Ni.

6.2.1 Partial removal of the AAO membrane

The aim of this process was to obtain aligned and free-standing nanowires by etching the membrane partially until a part of the nanowires with desired length appeared above the membrane. For starting this process from top side (opposed to the gold layer), first, several micrometers of the membrane should be etched to obtain the free-standing nanowires. Second, this process should be continued very precisely, several 100 *nm*, to get the free-standing nanowires with desired height. It is new process which has not been described in the literature to the best of my knowledge.

As it was mentioned in section 3.1.1 for removing the alumina membrane, the so-called orange solution is used.

In general, a membrane with 40 *μm* thickness and pores (diameter 75 *nm*) filled with Ag nanowires (length 1.5 *μm*) is used.

At the first attempt, for the partial removal of the alumina membrane, a carbon tape was attached on the backside of the sample, on the surface of the gold layer, as supporting layer to stabilize nanowires. Then the whole sample was immersed inside the orange solution at 60℃ for several min. Figure 6.2 a) shows the SEM image of top side of this sample, the formation

of the alumina filaments on the top of the nanowires are observed.

For solving this problem, a setup was designed (Figure 6.3) included: 1) a heating magnetic stirrer; 2) a bath warm water; 3) a sample holder with tunable height inside the so-called orange solution for keeping the sample on the surface of the orange solution and adjusting the distance between the sample on the surface of the solution and the bottom of the cell (Figure 6.3 b,c); and 4) digital thermostat with accuracy 0.01℃ for controlling precisely the temperature of the solution.

During the process of the partial removal of the membrane a magnetic stirrer is used below the sample to remove the alumina filaments. The distance between the sample and the bottom of the cell and the velocity of the magnetic stirring are crucial parameters. The SEM images of top view of the samples in Figure 6.2 b-d) represent the progress of this process. In fact, the free-standing nanowires with high quality are achieved when the magnetic stirrer is adjusted to 150 *rpm/min* while the distance between the sample and the bottom of the cell is 15 *mm*.

In this experiment, there are limitations for the diameter and the length of the nanowires inside the membrane as well as the length of the free-standing nanowires with respect to the AAO membrane surface after the partial removal of it. First, the length of the nanowires for this process should be at least 1 µm. Otherwise during the process of the dissolution, the membrane of the sample will be lost.

Second, many works have been done to indicate the dependence of the bending stiffness and the Young's modulus to the nanowire diameter and aspect ratio [167]. Xian-Fang Li et al. provided an adequate description based on the classic strain-gradient theory to prove that the effective Young's modulus and bending stiffness exhibit the size effect of the nanowires [168]. In this work, as the diameter is tunable in the range from 35 to 85 *nm*, for a smaller diameter a shorter length of the nanowires above the membrane should be released to prevent agglomeration of them. In contrast, nanowires with bigger diameter have more stiffness for free standing and a longer part of the nanowires can be released without agglomeration. There is a limitation for the diameter of the nanowires to have enough space around the nanowires for covering them with another metal. For example, Figure 6.2c shows free-standing nanowires with diameter 85 *nm* but without enough space around them.
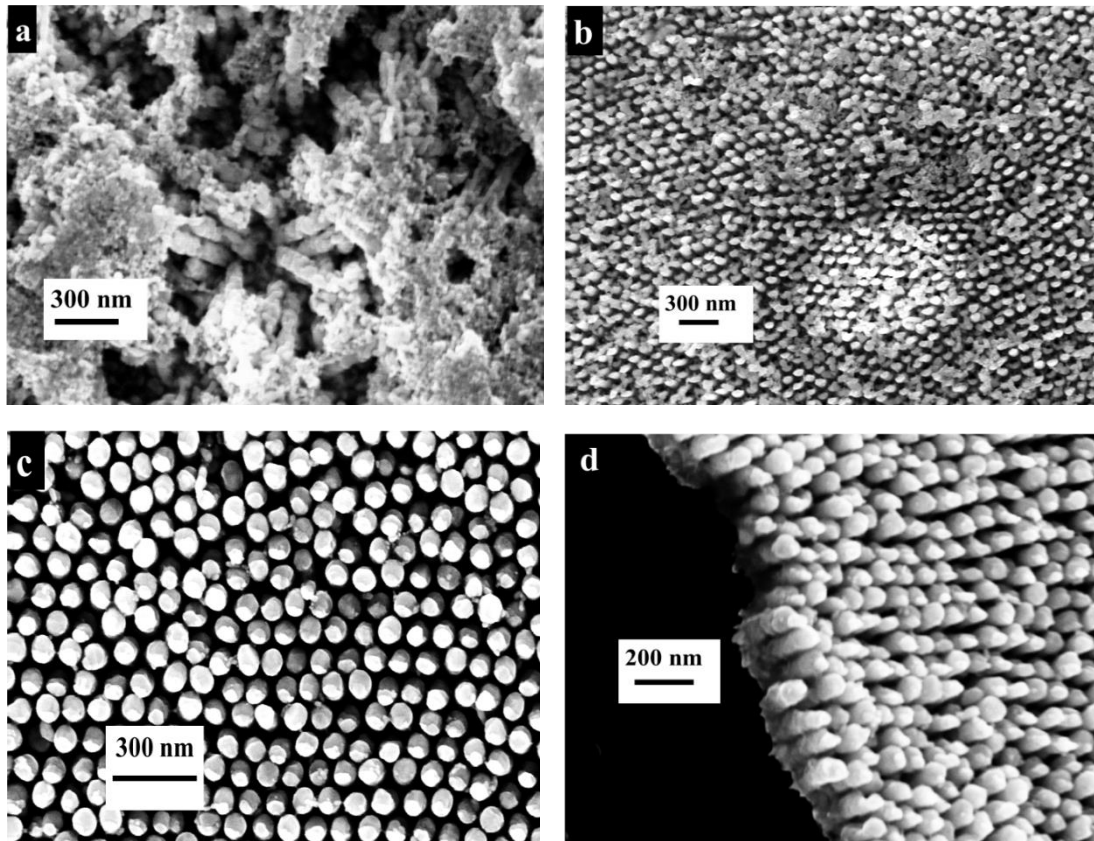
Figure 6.2. SEM images show the progress of the process of dissolving membrane partially to obtain aligned nanowires with diameter 60 *nm*. a) Covering nanowires by alumina filaments after dissolving the membrane, b-d) using a magnetic stirrer and keeping the sample above it and achieving free-standing aligned nanowires by modifying the conditions of removing partly the membrane.
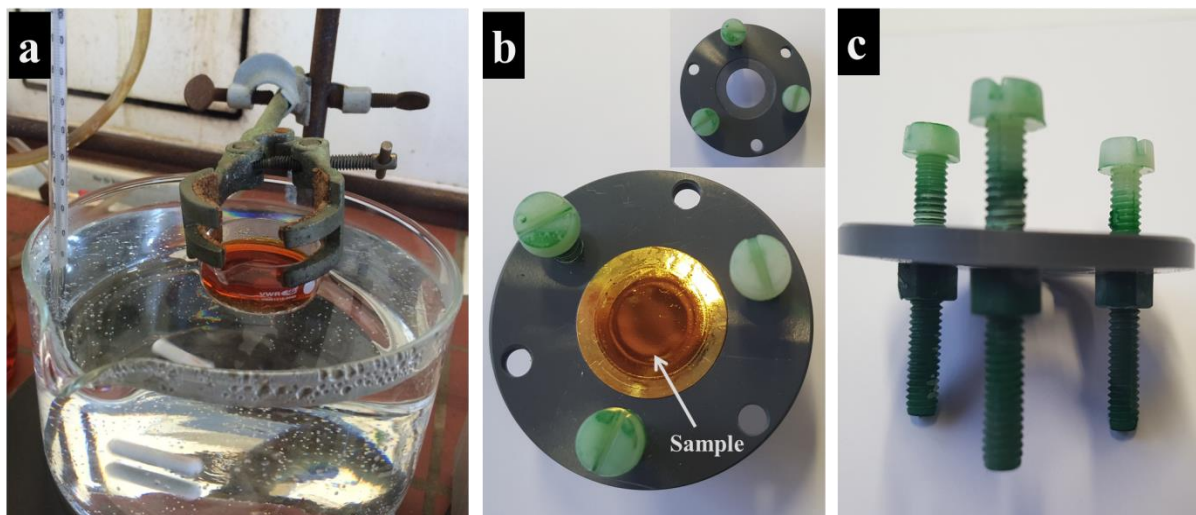
Figure 6.3. a) The setup for the partial removal of the anodic alumina membrane contained: 1) a heating magnetic stirrer; 2) a bath warm water; 3) a sample holder inside the so-called orange solution and 4) digital thermostat. b) and c) The top view and cross-section of the sample holder, respectively with tunable height.

The desired diameter for such experiment was in the range from 65 to 75 *nm* because it provides to obtain free-standing nanowires with the length of about 300 *nm* corresponding to the surface of the membrane. In previous works, an upper length limit of 300 *nm* for well-aligned Ni nanowires on the substrate by removing the AAO membrane was reported [6,169].

The length variation of the free-standing nanowires originates from (1) the distribution of the length of the nanowires synthesized electrochemically inside the membrane and (2) the inhomogeneous dissolution process. In this case, the length of the free-standing nanowires in comparison to the whole length of the nanowires, $1\mu m$, is adequate to reveal the effect of Ni, which caps the free-standing Ag nanowires, on the optical properties of Ag nanowires. Figure 6.4 shows the SEM images of free-standing Ag nanowires with a diameter 75 *nm* and the length of about 300 *nm* with respect to the membrane surface while the whole length of the Ag nanowires is about 1.4 μm.

Figure 6.4. a- c) SEM images of top view of free-standing aligned Ag nanowires with the length of 1.4 μm after removing partly the membrane.

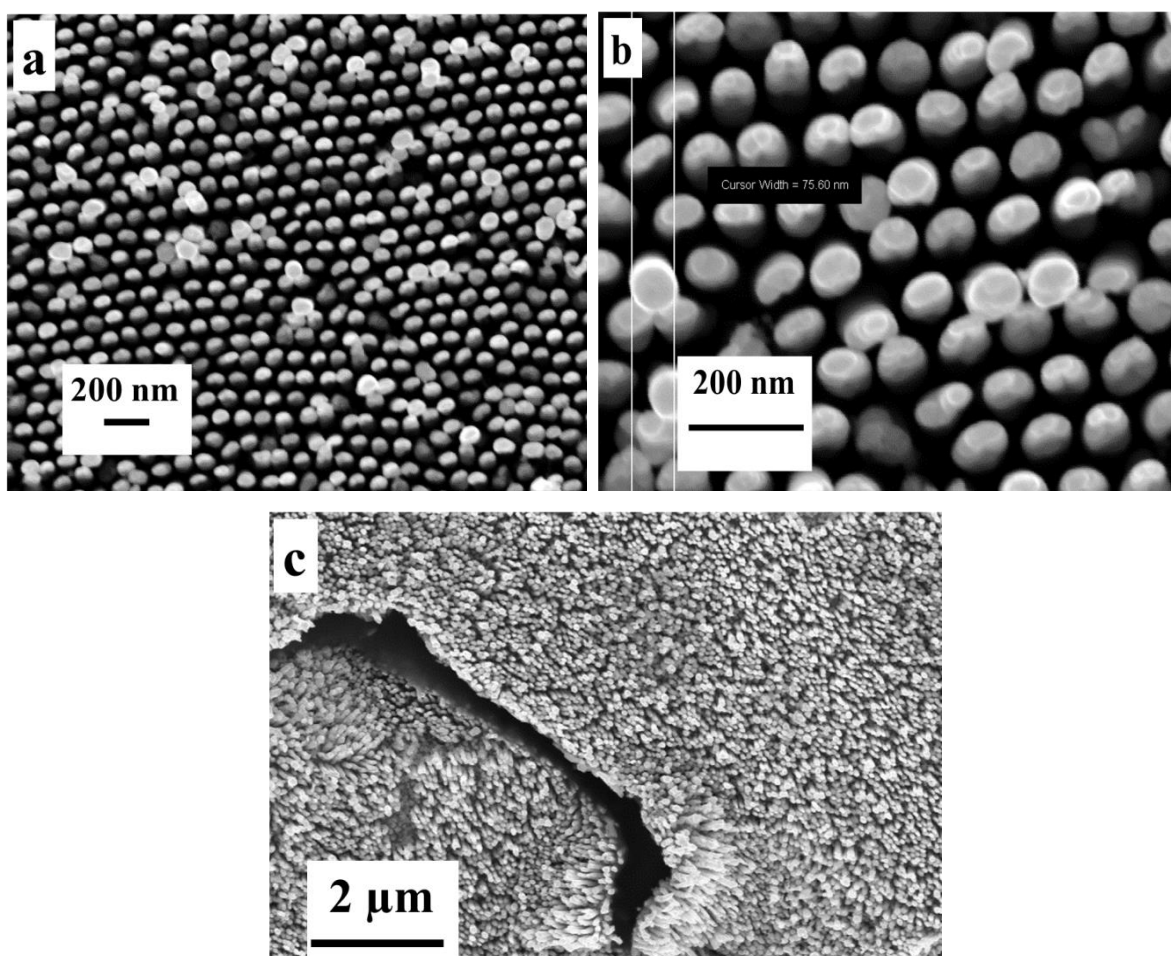Similarly, by using this strategy, the partial removal of a membrane from the backside (the gold layer side) was successfully carried out. A membrane with thickness 40 *μm* and pore diameter 40 *nm* filled with nanowires with the length of 6-7 *μm* was used for removing partially the membrane. For magnetic pinning at the tips of the nanowires, only few nanometer of the membrane from the backside was etched.

The process of etching partially from the backside included: 1) the top side of the sample (opposed the gold layer side) was glued, using G-varnish, onto a silicon substrate for better stability; 2) removing the gold layer using an aqueous of potassium iodine and iodine described in detail in chapter 3; 4) removing partially the AAO membrane for several tens of nanometers with the same strategy that was mentioned by keeping the sample for 4 min at 60°C in the so-called orange solution.

Figure 6.5 a) shows the SEM image of the backside of the membrane after removing the gold layer, and subsequently, Figure 6.5 b) represents the sample after the partial removal of the membrane. The free-standing nanowires tips and the surface of the membrane are identified by their light and dark contrasts, respectively. The length of the tips (about 40-70 *nm*) above the membrane was estimated by using Atomic Force Microscopy (AFM). This variation of tip length arises from the thickness variation of the evaporated gold layer inside the pores as well as the inhomogeneous etching process.

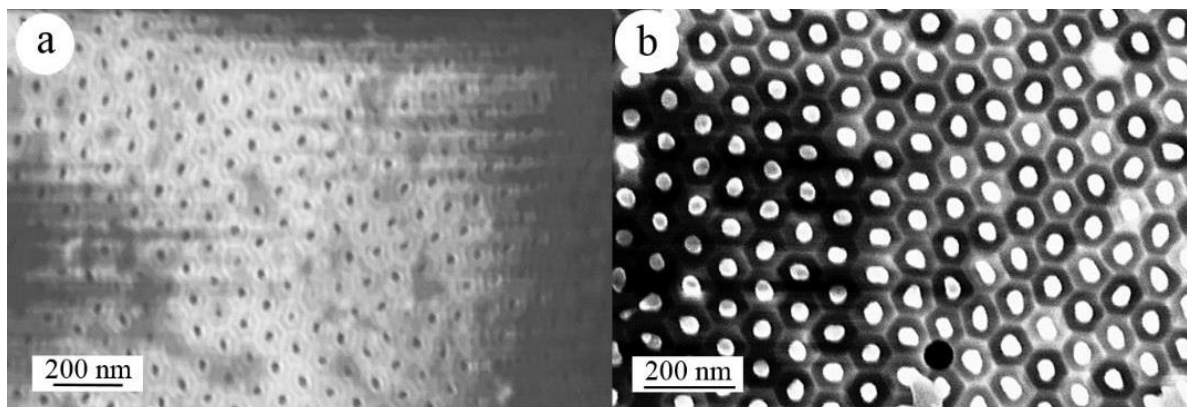**Figure 6.5.** a-b) SEM image of top view of a AAO membrane with pore diameter 40 *nm* filling with FeCo nanowires a) before and b) after partial removal of the AAO membrane. (b) The free-standing nanowires tips and the surface of the membrane are identified by their light and dark contrasts, respectively. The charging of the non-conductive membrane while scanning leads to different background contrast [170].

It seems that the partial removal of the membrane from the backside (the gold layer side) is easier where only few nanometers of the membrane should be removed, while from top side several micrometers should be removed to obtain free-standing nanowires.

6.2.2   Coating the free-standing Ag nanowires with Ni

In the following, coating the free-standing Ag nanowires with Ni electrochemically is described. As mentioned previously, AAO membranes are fragile so for handling during the process of the partly removal a supporting layer was needed. In addition, this supporting layer should have enough conductivity for using it as a part of the working electrode. In this case, the conductivity of the working electrode included: 1) Ag nanowires, 2) gold layer, and 3) the supporting layer.

Several options were investigated: (1) *Carbon tape* but its conductivity was low; (2) an alternative possibility to increase the conductivity was to use *silver paint* to cover homogeneously the gold layer side by spin coating. Despite the advantages of using silver paint, high conductivity and easily dissolving it at the end of the process for releasing the nanowires, it has been observed that the strength of the silver paint was not enough to support the sample, especially during the electrochemical deposition process. (3) Finally, a *copper tape* from company 'Plano GmbH' with conductive adhesive and high strength served as a supporting layer as well as a working electrode.

Figure 6.6 a) and b) shows a membrane filled with Ag nanowires before and after removing partially the membrane, respectively. Prior to etching of the membrane, a copper tape was attached on the gold layer side. The aluminum around the membrane is usually separated during the process of etching, consequently, the other side of the copper tape is attached on an Al foil for better stability.
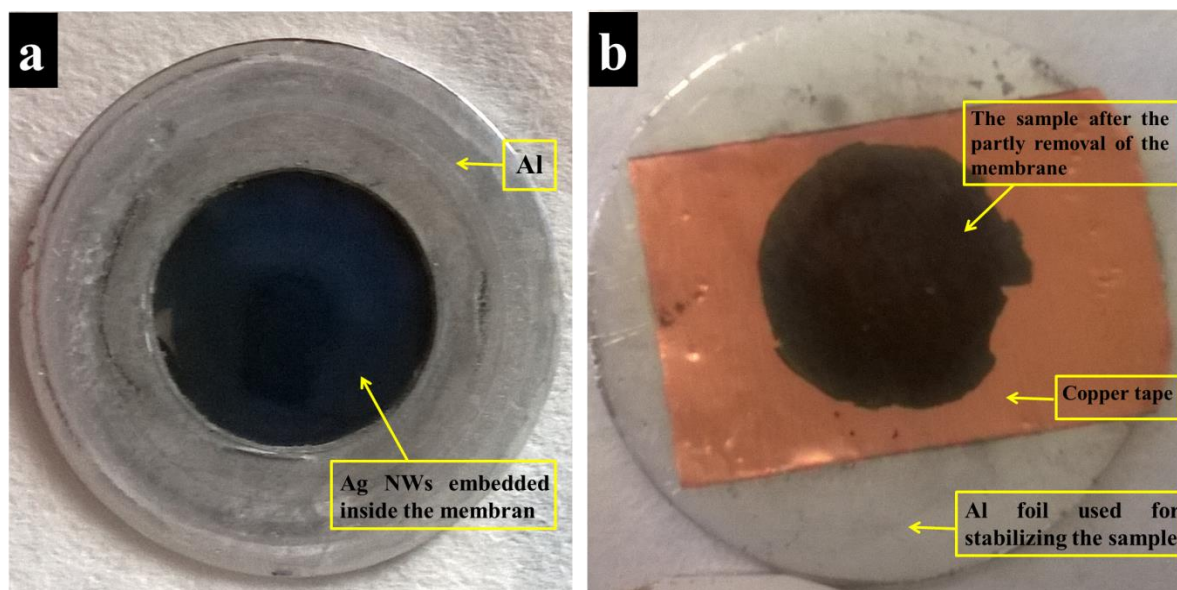
Figure 6.6. Synthesized Ag nanowires inside a membrane a) before and b) after removing partially the membrane. A copper tape with high conductivity attached on the backside (the gold layer side) of the sample is served as a supporting layer and a working electrode. The aluminum around the membrane is separated during the etching process so the other side of the copper tape is attached on an aluminum foil for better stability.

It is expected that by putting such sample into an electrolyte and applying a certain potential, ions inside the electrolyte migrate towards the silver nanowires and form a layer around them. For the first attempt, a sample included not well-aligned Ag nanowires was considered to cover them with Ni electrochemically and the aim was to ensure if it is possible to follow such innovative method for achieving new design of nanohybrids.

The conditions for deposition of Ni were described in details in chapter 4. In this experiment, the working electrode was a combination of Al, the copper tape, Au layer and Ag nanowires. The applied potential between the working electrode and the reference electrode was -1 *V*. It is worth noting that the estimation of the whole free area of the aligned nanwoires was so complicate because of the distribution of the length and diameter as well as agglomeration of nanowires in some parts. Subsequently, estimating the rate of deposition was difficult so for the first attemp the time of deposition was considered for a short time, 4 *s*.

Figure 6.7 represents the result of EDX spectra for this sample that proves the presence of Ni on Ag nanowires. It was not expected that the Ag nanowires were coated homogeneously because they agglomerated. Corresponding to the EDX spectra some contaminations from the

orange solution (Cr and P) on the sample exist. Oxygen and carbon exist inside the chamber of the SEM system.

Consequently, copper tape was a good alternative used as a supporting layer and conductive layer, however, the disadvantage of using copper tape is the difficulty for separating it from the sample for releasing and dispersing the nanowires at the end of the process.
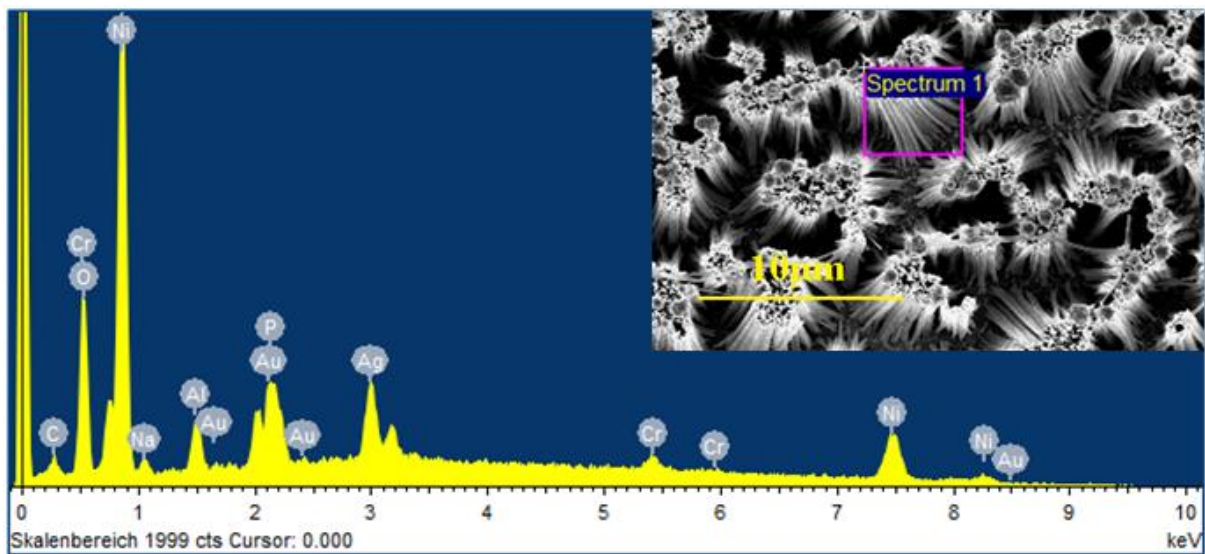
Figure 6.7. EDX analysis of agglomerated and released Ag nanowires covered with Ni. The spectra also show the presence of some contamination on the sample from the orange solution (Cr and P); oxygen and carbon exist inside the chamber of the system.

The next step was to improve this process by coating the free-standing well-aligned Ag nanowires homogeneously. The process was repeated for the well-aligned Ag nanowires introduced in Figure 6.4 with $75(\pm 5)\ nm$ diameter and the length of $300\ nm$ above the membrane. After coating the nanowires with Ni, the sample was analyzed by using SEM to investigate the morphology of nanohybrids described in the following section.

6.3 Morphology of Ni capped Ag nanohybrids

After coating aligned Ag nanowires by Ni, the sample was prepared (details were described in section 3.1.5) for characterizing. Figure 6.8 shows the top view SEM images of the sample. One observes a variation of the diameter of Ni capped Ag nanowires, roughly in the range from 90 to 180 nm, due to the distribution of the diameter and the length of the nanowires. In SEM images the longer and shorter nanowires are identified by their light and dark contrasts. For longer Ag nanowires with enough space around them the diameter of the nanowires after coating Ni increased dramatically, from 75 nm to about 180 nm. In contrast, for short length nanowires, no significant difference in the diameter is observed. It increased from 75 nm to about 90 nm.
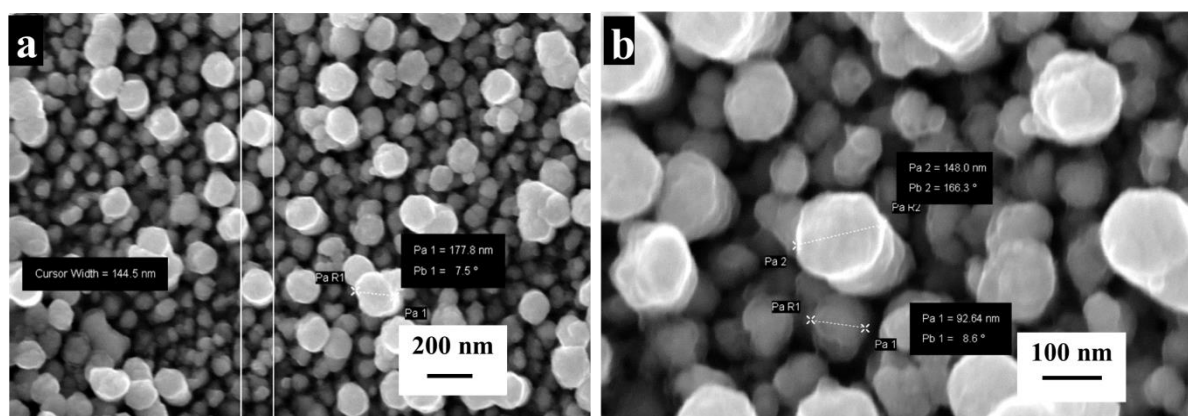
Figure 6.8. a-b) The top view SEM images of free-standing Ag nanowires (diameter 75 nm) coated with Ni. The diameter of Ni capped Ag nanowires is roughly in the range from 90 to 180 nm. The longer nanowires are identified with their light contrast and the diameter of longer nanowires has increased significantly because of enough space around them while for short length nanowires no significant difference in the diameter of nanowires is observed due to lack of space around the nanowires.

After tilting the sample inside the SEM, the cross section of Ni-capped Ag nanohybrids above the membrane indicates a conical shape of such hybrid (Figure 6.9 a-c). Figure 6.8 c reveals that the released part of the nanowires was not coated homogeneously and the diameter of the hybrid nanostructures on the tip is the biggest, 105 nm, and it gradually reduces to reach to the lowest point of the hybrids, 85 nm.

These structures indicate that during the deposition, the reduction of Ni ions takes places more on the tip of the free-standing nanowires before reaching the bottom of the wires. It may be because of higher charge distribution at the tip of the nanowires due to the inhomogeneous surface on the tip which leads to more reduction of the ions.
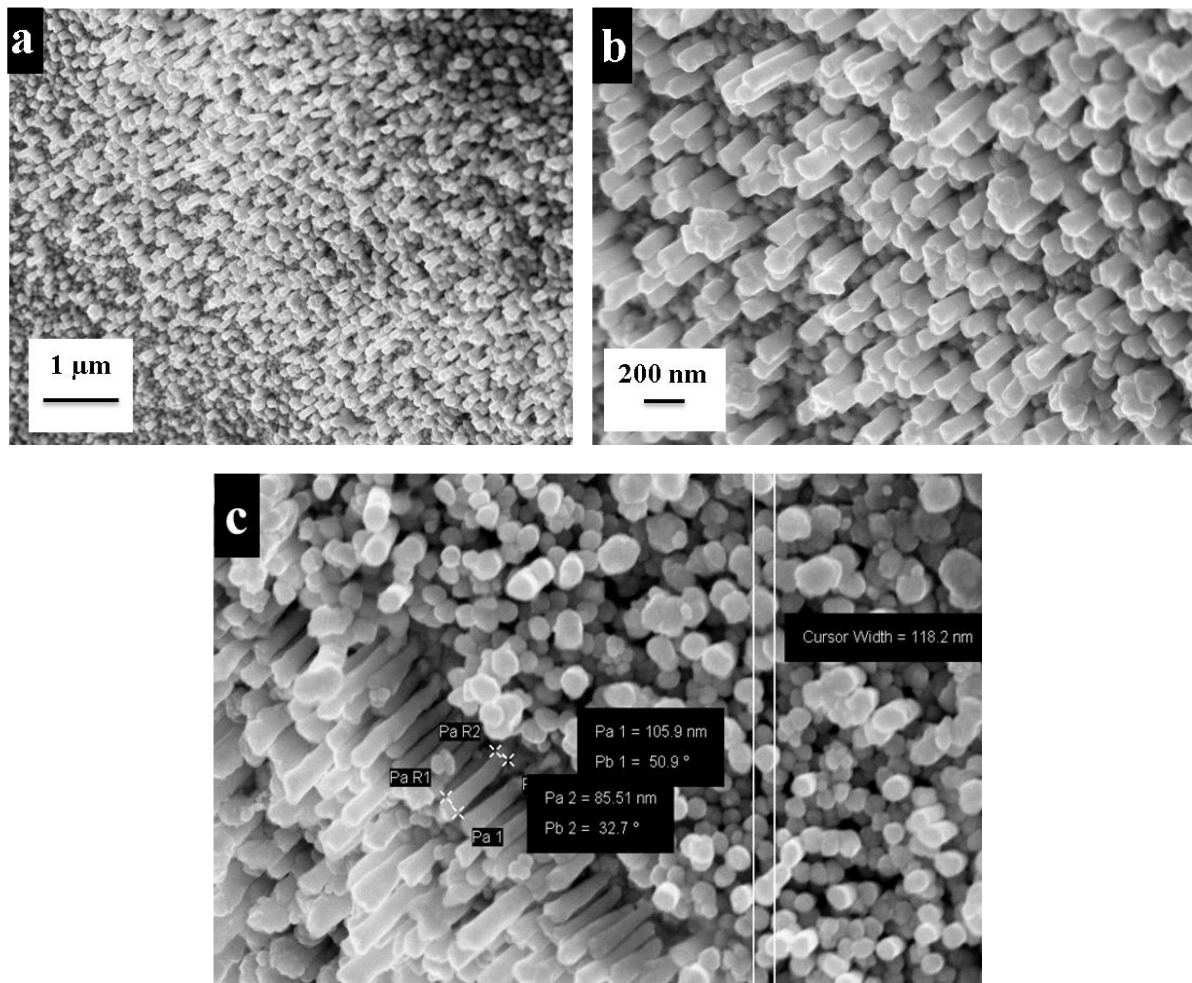
Figure 6.9. a-c) The SEM images of cross section of Ni capped Ag nanohybrids with conical shape above the membrane. The diameter of pure Ag nanowires is 75 *nm* and the diameter of the hybrid nanostructures on the tip is the biggest, 105 *nm*, and it gradually reduces to reach to the lowest point of the hybrids, 85 *nm*, above the membrane.

For better understanding of the shape of such nanohybrids, Figure 6.10 illustrates the 2D cross section of Ni capped Ag nanohybrids with a trapezius shape above the membrane, while pure Ag nanowires embedded inside the membrane.
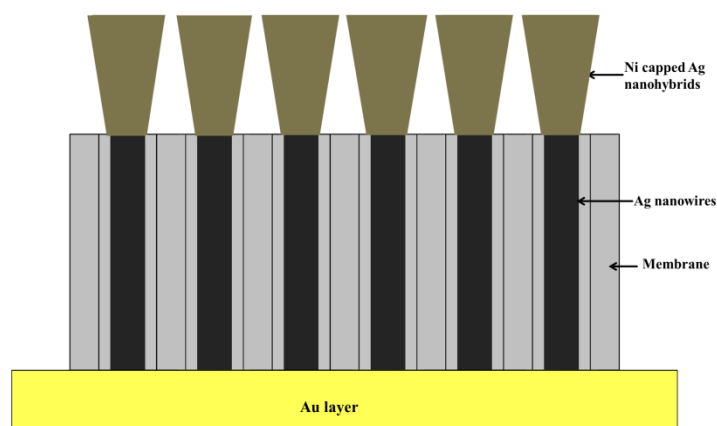
Figure 6.10. The 2D schematic of cross section of Ni capped Ag nanohybrids above the membrane.

It should be considered that analyzing the short nanowires is more complicate issue as by using SEM, only the top view of such nanowires is observable even when tilting the sample. However, the SEM images reveal that the diameter of such nanowires increased, described in Figure 6.8 but there is a probability of connecting such nanowires together by coating them. As it was mentioned, the copper tape used as supporting layer on the back side of the sample makes it complicate to release the nanowires, consequently, characterizing the nanowires by using TEM was not possible.

6.4 Conclusions

The synthesis and the innovative design of complex multi component of two metals, Ni, and Ag, have been performed successfully using a multi-step process of fabrication contained electrochemical deposition for two steps and the partly removal of the AAO membrane. A single multicomponent includes a pure Ag and Ni capped Ag nanohybrids with conical shape. This complex design of the heterojunctions allows the investigation of the plasmonic properties of pure silver capped with nickel in a single hybrid that can often give access to innovative properties.

Summary

Ni nanowires are synthesized as a function of the deposition potential ranging from -0.8 V to -1.5 V vs the reference electrode Ag/AgCl to improve their crystallinity. It is observed that the growth rate depends on the deposition potentials and increases nearly linearly by increasing the potentials, reaching 5µm min^{-1} for -1.5 V. Despite polycrystalline nature of most the Ni nanowires synthesized at such range of the potential, at potential ranges -1 V and -1.1 V vs. the reference electrode the crystallinity of them is better. In other words, it is observed larger grain sizes in polycrystalline nanowires as well as more single crystalline ones with growth orientation <011>.The grain size of Ni nanowires synthesized at -1V and -1.1 V reached up to 50 nm, however, for nanowires synthesized at -1.5 V was in the ranging from 5 to 20 nm.

 The magnetic properties (the coercivity and the remanence) of the Ni nanowires with the same aspect ratio, and with interpore distance of 105 nm, as a function of the deposition potentials were studied. The similar results suggest that for Ni nanowires with fcc structure the shape anisotropy overcomes on the magnetocrystalline anisotropy. Consequently, the magnetic properties strongly depend on the aspect ratio, and the magnetic dipole-dipole interactions between the nanowires. For close packing nanowires, the dipole-dipole interactions among the nanowires reduce the shape anisotropy field.

To compare the experimental values of the coercive field of Ni nanowires (40 nm diameter, and with the length of 1.4 $µm$) with a theoretical approach, the coercive field for ideal case of isolated nanowires for coherent magnetization reversal is estimated. Very big difference between the values of the coercive fields theoretically ($\mu_0 H_c = 0.29\ T$ by neglecting the magnetocrystalline anisotropy, $\mu_0 H_{MC} = 21 mT$), and experimentally ($\mu_0 H_c = 96\ mT$) can be attributed to different magnetization reversal mode. Because the magnetization reversal modes have the main influence on the coercivity. It might be more likely that domain walls nucleate at the ends of the nanowires and propagate along the nanowires instead of the coherent rotation.

To improve the magnetic properties of Ni nanowires, they are annealed at 650°C under Ar atmosphere for 24 h. The decreasing of the coercivity of the Ni nanowires after annealing process offers the decrease of the vacancies inside the nanowires.

For studying the magnetic anisotropy and the effect of the magnetic dipole-dipole interactions between the nanowires, the FMR measurements are carried out for two samples of Ni nanowires with different diameters, 35 *nm* and 45 *nm*, but with the same length (1.6 *μm*) and interpore distance of 105 *nm*. The angular dependence of the resonance field at 9.77 *GHz* at room temperature reveals that for both samples the easy axis is along the wire axis. There is a big deviation between the values of the effective anisotropy fields theoretically and experimentally for both samples. The main difference arises from the dipolar interactions between the nanowires corresponding to the porosity of the membrane, while theoretically, the effective field is calculated for an isolated nanowire. Consequently, the effective anisotropy field is given by $\frac{1}{2}\mu_0 M_S(1-3P)$ that this leads to $\mu_0 H_{eff} = 215\ mT$ for Ni nanowires with 35 *nm* diameter and porosity 10% and $\mu_0 H_{eff} = 160\ mT$ for Ni nanowires with 45 *nm* diameter and porosity 16%. Consequently, close packing nanowires inside the membrane leads to large dipolar field result in the decrease of the effective anisotropy field.

In the second study, hybrid nanowires consisting of Ni and Ag segments have been successfully synthesized and optimized to create Ni-Ag nanowires with sharp interfaces. They are characterized by structural, magnetic and optical techniques.

It is demonstrated that the transverse localized surface plasmon resonance mode of Ag with the length of 210(±20) *nm*, and 75(±5) *nm* diameter in three-segmented Ni-Ag-Ni nanowires changes by 12 *nm* at wavelength 438 *nm* rather than the pure Ag nanowires. The higher order transverse plasmon modes of the Ag segment can be identified as a distinct peak at 366 *nm*, while for individual Ag nanowires a very small shoulder is appeared at 375 *nm*. In addition, a narrow peak with high intensity of Ni segments at 313 *nm* is observed that is not visible for Ni with long length (the length of the first and the second segments of Ni are 560 (±50) *nm* and 1150 (±150) *nm*, respectively).

In the following, the magnetic properties of Ni/Ag nanowires with the same length and different porosity have been investigated using FMR measurement. The values of the uniaxial anisotropy effective fields for pure Ni and hybrid of Ni/Ag nanowires are different. It is more likely that The Ag part as a diamagnetic material effects on the dipole interactions among the Ni/Ag nanowires that leads to the reduction of the effective magnetic anisotropy of the sample. Another assumption arises from the effect of electromigration inside the Ni part during the deposition of Ag segment that might be influenced on the crystallinity of the Ni segment, however for Ni case the magnetocrystalline anisotropy is very low.

In the third work, the innovative design, and the synthesis of complex multi component of Ni and Ag have been done successfully. A single multicomponent includes a pure Ag and Ni capped Ag nanohybrids with conical shape. The synthesis of such multi component has been achieved by using a multi-step process of fabrication contained electrochemical deposition for two steps and the partly removal of the AAO membrane. The process of the partly removal of fragile AAO membrane requires a precise control on the free length of the nanowires above the membrane.

This complex design of the heterojunctions allows the investigation of the plasmonic properties of pure silver capped with nickel in a single hybrid that can often give access to innovative properties.

Bibliography

1. T. M. Whitney, J.S. Jiang, P. C. Searson and C. L. Chien; Fabrication and Magnetic Properties of Arrays of Metallic Nanowires; Science 261, 1993**,** 1316

2. J. I. Yeh and H. Shi; Nanoelectrodes for biological measurements ; Wiley Interdiscip. Rev.: Nanomed.Nanobiotechnol. 2, 2010, 176

3. T. Thurn-Albrecht , J. Schotter , G. A. Kästle, N. Emley, T. Shibauchi, L. Krusin-Elbaum , K. Guarini, C. T. Black, M. T. Tuominen and T. P. Russell; Ultrahigh-density nanowire arrays grown in self-assembled diblock copolymer templates; Science 290, 2000**,** 2126

4. C. Ross; Patterned magnetic recording media; Annu. Rev. Mater. Res. 31, 2001, 203

5. X. Kou, X. Fan, H. Zhu and J. Xiao; Tunable ferromagnetic resonance in NiFe nanowires with strong magnetostatic interaction; Appl. Phys. Letts. 94, 2009, 112509

6. Nina Winkler, Jörn Leuthold, Yong Lei and Gerhard Wilde; Large-scale highly ordered arrays of freestanding magnetic nanowires; J. Mater. Chem. 22**,** 2012, 16627-16632

7. Mingliang Tian , Jinguo Wang , James Kurtz , Thomas E. Mallouk , and M. H. W. Chan; Electrochemical Growth of Single-Crystal Metal Nanowires via a Two-Dimensional Nucleation and Growth Mechanism; Nano Letters, 2003, 3 (7), pp 919–923

8. Hui Pan, Han Sun, Cheekok Poh,Yuanping Feng and Jianyi Lin; Single-crystal growth of metallic nanowires with preferred orientation; Nanotechnology16, 2005, 1559–1564

9. Andrea Cortés, Gonzalo Riveros, Juan L. Palma, Juliano C. Denardin, Ricardo E. Marotti, Enrique A. Dalchiele, and Humberto Gómez; Single-Crystal Growth of Nickel Nanowires: Influence of Deposition Conditions on Structural and Magnetic Properties; J. Nanosci. Nanotechnol. 9, 2009, No. 3

10. T. W. Ebbesen, H. J. Lezec, H. F. Ghaemi, T. Thio, P. A. Wolff, Extraordinary optical transmission through sub-wavelength hole arrays, Nature 391, 1998, 667

11. Antonella Gentile, Francesco Ruffino, and Maria Grazia Grimaldi, Complex-Morphology metal- based nanostructures: fabricaion, characterization and applications, Nanomaterials 6, 2016, 110

12. Maureen McKiernan, Jie Zeng, Sunzida Ferdous, Steven Verhaverbeke, Kurtis S. Leschkies, Roman Gouk, Christopher Lazik, Miao Jin, Alejandro L. Briseno, and Younan Xia, Facile Synthesis of Bimetallic Ag/Ni Core/Sheath Nanowires and Their Magnetic and Electrical Properties, small 6, 2010, No. 17, 1927–1934

13. Samarpita Senapati, Suneel K. Srivastava, Shiv B. Singh and Hari N. Mishra; Magnetic Ni/Ag core-shell nanostructure from prickly Ni nanowire precursor and its catalytic and antibacterial activity, J. Mater. Chem. 22, 2012, 6899-9606

14. Sungwan Kim, Seong Kyu Kim, and Sungho Park, Bimetallic Gold-Silver Nanorods Produce Multiple Surface Plasmon Bands, J. AM. CHEM. SOC. 131, 2009, 8380-8381

15. Zhaleh Pirzadeh, Tavakol Pakizeh, Vladimir Miljkovic, Christoph Langhammer, and Alexandre Dmitriev, Plasmon-Interband Coupling in Nickel Nanoantennas Acs photonic 1, 2014, 158-162

16. Jörg P. Kottmann, Olivier J. F. Martin, David R. Smith, and Sheldon Schultz, Plasmon resonances of silver nanowires with a nonregular cross section, Physical review B, 64, 2001, 235402

17. Francesco Pineider, Giulio Campo, Valentina Bonanni, César de Julián Fernández, Giovanni Mattei, Andrea Caneschi, Dante Gatteschi, and Claudio Sangregorio, Circular Magnetoplasmonic Modes in Gold Nanoparticles, Nano letters 13, 2013, 4785-4789

18. Valentina Bonanni, Stefano Bonetti, Tavakol Pakizeh, Zhaleh Pirzadeh, Jianing Chen, Josep Nogues,r Paolo Vavassori, Rainer Hillenbrand, Johan Åkerman and Alexandre Dmitriev, Circular Magnetoplasmonic Modes in Gold Nanoparticles, Nano letters 11, 2011, 5333-5338

19. V.V. Temnov, C. Klieber, K.A. Nelson, G. Armelles, A. Garcia-Martin, A. Cebollada, J.M. Garcia-Martin, D. Martin-Becerra, J.B. Gonzalez-Diaz, M. Ujue-Gonzalez, T. Thomay, A. Leitenstorfer, D. Makarov, M. Albrecht and R. Bratschitsch, Active

magneto-plasmonics in hybrid metal-ferromagnet structures, Nature Photonics 4, 2010,107-111

20. Xiaobin Xu , Huifeng Li , Dihan Hasan , Rodney S. Ruoff , Alan X. Wang , and D. L. Fan, Near-Field Enhanced Plasmonic-Magnetic Bifunctional Nanotubes for Single Cell Bioanalysis , Adv. Funct. Mater. 23, 2013, 4332–4338

21. Juan B. Gonzlez-Diaz, Antonio Garcia-Martin, Jose M. Garcia-Martin, Alfonso Cebollada, Gaspar Armelles, Borja Sepffllveda, Yury Alaverdyan, and Mikael Käll, Plasmonic Au/Co/Au Nanosandwiches with Enhanced Magneto-optical Activity, small 4, 2008, No. 2, 202 – 205

22. Sheng Peng, Changhui Lei, Yang Ren, Russell E. Cook, Yugang Sun, Plasmonic/Magnetic Bifunctional Nanoparticles, Angew. Chem.Int. Ed. 50, 2011, 3158

23. L. Wang, C. Clavero, Z. Huba, K.J. Carroll, E.E. Carpenter, D.F. Gu, R.A. Lukaszew, Plasmonics and Enhanced Magneto-Optics in Core-Shell Co-Ag Nanoparticles, Nano Letters 11, 2011, 1237-1240.

24. Jiaojiao Hua, Fan Wu, Fengru Fan, Wenhui Wang, Zhongfeng Xu and Fuli Li, Synthesis and surface plasmonic properties of ultra-thick silver nanowires, J. Phys. Condens. Matter 28, 2016, 254005

25. C. S. Levin , C. Hofmann , T. A. Ali , A. T. Kelly , E. Morosan , P. Nordlander , K. H. Whitmire , N. J. Halas , Magnetic-plasmonic core-shell nanoparticles, ACS Nano 3, 2009, 1379

26. X. Wang, X. Ren, K. Kahen, M. A. Hahn, M. Rajeswaran, J. Silcox, G. E. Cragg, A. L. Efros, T. D. Krauss, Non-blinking semiconductor nanocrystals, Nature 459, 2009, 686

27. E. C. Cho, P. H. C. Camargo, Y. Xia, Synthesis and characterization of noble-metal nanostructures containing gold nanorods in the center, Adv. Mater. 2010 , 22 , 744

28. J. Zhang , Y. Tang, K. Lee, M. Ouyang, Nonepitaxial Growth of Hybrid Core-Shell Nanostructures with Large Lattice Mismatches, Science 327, 2010, 1634
pack

29. J. Zeng, J. Huang, C. Liu, C. Hao, Y. Lin, X. Wang, S. Zhang, J. Hou, Y. Xia, Gold-

Based Hybrid Nanocrystals Through Heterogeneous Nucleation and Growth, Adv. Mater.22, 2010, 1936

30. C. Kittel, Introduction to solid state physics, 7th ed., New York, John Wiley & sons, 2006, p. 446-450

31. B. D. Cullity and C. D. Graham, Introduction to magnetic materials, Hoboken, New Jersey, 2009

32. C. Binns, Nanomagnetism: fundamentals and applications, Poland, 2014

33. N. W. Ashcroft and N. D. Mermin, Solid state physics, New York,1976

34. J. Stöhr and H. C. Siegmann, Magnetism, from fundamentals to nanoscale dynamics, Berlin and Heidelberg, 2006

35. M. Farle, Magnetic nanoparticles (Magnetism goes Nano), Jülich, Forschungszentrum Jülich GmbH, 2005, p. C4

36. R. C. O´Handley, Modern magnetic materials, principles and applications, New York, 2000

37. Ulf Wiedwald, Interface magnetism in Co/CoO core-shell nanoparticles and their transformation to pure metallic nanoparticles; PhD thesis, Duisburg-Essen University, 2004

38. K. Nielsch, R. B. Wehrspohn, J. Barthel, J. Kirschner, U. Gösele, S. F. Fischer and H. Kronmüller, Hexagonally ordered 100 nm period nickel nanowire arrays, Apply Physics letters 79, 2001, 1360

39. J. Lindner and M. Farle, Magnetic Anisotropy of Heterostructures, in Advances and Perspectives in Spinstructures and Spintransport, edited by H. Zabel and S. D.Bader, vol. 227 of Series: Springer Tracts in Modern Physics, Springer 2008

40. M. Jamet, W. Wernsdorfer, C. Thirion, V. Dupuis, P. Mlinon, A. Prez and D. Mailly, Magnetic anisotropy in single clusters, Physical Review B 69, 2004, 024401

41. E. Klokholm and J. Aboaf, The saturation magnetostriction of thin polycrystalline films of iron, cobalt, and nickel, J. Appl. Phys. 53, 1982

42. Mircea Chipara, Ralph Skomski, Roger Kirby, and David J. Sellmyer; Ferromagnetic resonance on Ni nanowire arrays; J. Mater. Res., Vol. 26, No. 17, 2011

43. S. Dubois and J. Colin, J. L. Duvail, L. Piraux, Evidence for strong magnetoelastic effects in Ni nanowires embedded in polycarbonate membranes, Physical review B, 61, number 21, 2000

44. Paulo S. Branı´cio and Jose´-Pedro Rino, Large deformation and amorphization of Ni nanowires under uniaxial strain: A molecular dynamics study, Physical review B, 62, number 24, 2000

45. Michael Farle; Ferromagnetic resonance of ultrathin metallic layers; Rep. Prog. Phys. 61 (1998) 755–826

46. Orhan Yalcin; Ferromagnetic resonance-Theory and Applications; 2013; printed in Croatia

47. G. KartopuO Yalçın, KL Choy, R Topkaya, S Kazan, B Aktaş, Size effects and origin of easy-axis in nickel nanowire arrays, J. Appl. Phys. 109, 2011, 033909

48. M. Sharma, Sachin Pathak and Monika Sharma; Ferromagnetic Resonance - Theory and Applications, book edited by Orhan Yalcin , ISBN 978-953-51-1186-3, 2013

49. A. Encinas-Oropesa, M. Demand, L. Piraux, I. Huynen, and U. Ebels; Dipolar interactions in arrays of nickel nanowires studied by ferromagnetic resonance; Physicsl review B, 63, 2001, 104415

50. Stephan Link and Mostafa A. El-Sayed; Optical properties and ultrafast dynamics of metallic nanocrystals, Annu. Rev. Phys. Chem. 2003. 54:331–66

51. S. Link and M. A. El-Sayed; Shape and size dependence of radiative, non-radiative and photothermal properties of gold nanocrystals; Int. Reviews in Physical Chemistry 19; 2000; No. 3

52. Andreas Trügler; Optical properties of metallic nanoparticles; PhD Thesis, Karl–Franzens–Universität Graz, 2013

53. E. Margapoti; Plasmonics: Fundamentals and Applications; 2012; TU München

54. Michael I. Mishchenko, Larry D. Travis, Andrew A. Lacis; Scattering, absorption and emission of light by small particles; Nasa 2002; Cambridge University Press

55. Carsten Sönnichsen; Plasmons in metal nanostructures; PhD thesis; Ludwig-Maximilians-Universität München; 2001

56. Teri W. Odom, and George C. Schatz, Introduction to plasmonics, Chem. Rev. 111, 2011, 3667–3668

57. S. A. Maier, Plasmonics: Fundamentals and applications, Speringer 2007

58. S. Jung et al., J. Phys. Chem. C 2013, 117, S. A. Lee et al., J. Phys. Chem. C 116, 2012, 18388-18393

59. Yong Chen, Hai Ming, Review of surface plasmon resonance and localized surface plasmon resonance sensor, Photonic Sensors 2, 2012, No. 1, 37–49

60. E. A. Coronado, G. C. Schatz, Surface plasmon broadening for arbitrary shape nanoparticles: A geometrical probability approach, J. Chem. Phys. 119, 2003

61. Jagmeet Singh Sekhon, S. S. Vermaand; Tunable plasmonic properties of silver nanorods for nanosensing applications, J. Mater. Sci. 47, 2012, 1930–1937, 30

62. M. Hu, C. Novo, A. Funston, H. Wang, H. Staleva, S. Zou, P. Mulvaney, Y. Xia, G. V. Hartland, J. Mater. Chem. 18, 2008

63. G.C. Papavassiliou, Optical Properties of Small Inorganic and Organic Metal Particles, Prog. solid st. Chem., 12, 1979, 185

64. M. Kerker, The Scattering of Light and Other Electromagnetic Radiation (New York: Academic Press), 1969

65. C.F. Bohren and D.R. Huffman, Absorption and Scattering of Light by Small Particles (New York: Wiley), 1983

66. Y. Yu, S. Chang, C. Lee and C.R.C. Wang, Gold Nanorods: Electrochemical Synthesis and Optical Properties, J. phys. Chem. B, 101, 1997, 34, 6661

67. B. M. I. Vanderzandeh , M. R. Bohmer, L. G. J. Fokkink and C. Schonenberger, Aqueous gold sols of rod-shaped particles, J. phys. Chem. B, 101, 1997, 852

68. H. Okamoto, and K. Imura, Near-field imaging of optical field and plasmon wavefunctions in metal nanoparticles, J. Mater. Chem.16, 2006, 3920–3928

69. Yong Lei, Weiping Cai, Gerhard Wilde; Highly ordered nanostructures with tunable size, shape and properties: A new way to surface nano-patterning using ultra-thin alumina masks; Progress in Materials Science 52, 2007, 465–539

70. Vazquez, M; Pirota, K; Torrejon, J; Magnetic behavior of densely packed hexagonal arrays of Ni nanowires: Influence of geometric characteristics; Journal of magnetism and magnetic materials 294, 2005, 174-181

71. Pirota, KR; Vazquez, M; Arrays of electroplated multilayered Co/Cu nanowires with controlled magnetic anisotropy; Advanced Engineering Materials 7, 2005, 1111-1113

72. G. E. Thompson, R. C. Furneaux, G. c. Wood, J. S. Goode, Nucleation and growth of porous anodic films on aluminium; Nature 272, 1978, 433 – 435

73. Masuda H., Fukuda K.; Ordered metal nanohole arrays made by a two-step replication of honeycomb structures of anodic alumina; Science 268, Issue 5216, 1995, 1466-1468

74. J. Oh, Porous Anodic Aluminum Oxide Scaffolds, Formation mechanisms and Applications, Massachusetts Institute of Technology, 2010

75. Manuel Vazquez; Magnetic nano and microwires: design, synthesis, properties and application; 2015, Woodhead publishing

76. F. Zhou, A. Baron-Wieche´c, S.J. Garcia-Vergara, M. Curioni, H. Habazaki, P. Skeldon, G.E. Thompson; Effects of current density and electrolyte temperature on the volume expansion factor of anodic alumina formed in oxalic acid; Electrochimica Acta 59 (2012) 186– 195

77. A. P. Li, F. Müller, A. Birner, K. Nielsch, and U. Gösele; Hexagonal pore arrays with a 50–420 nm interpore distance formed by self-organization in anodic alumina; J. Appl. Phys. 84, No. 11, 1998

78. Kornelius Nielsch, Jinsub Choi, Kathrin Schwirn, Ralf B. Wehrspohn, and Ulrich Go1sele, Self-ordering Regimes of Porous Alumina: The 10% Porosity Rule, Nano Lett. 2, No. 7, 2002

79. O. Jessensky, F. Muller, U. Gosele, Self-organized formation of hexagonal pore arrays in anodic alumina, Applied Physics Letters 72 (10),1998, 1173-1175

80. Mariana P. Proenca, Celia T. Sousa, Joao Ventura, Manuel Vazquez, Joao P. Araujo; Ni growth inside ordered arrays of alumina nanopores:Enhancing the deposition rateElectrochimica Acta 72 , 2012, 215– 221

81. Diana Leitao; Micro and Nano Patterned Magnetic Structures; PhD thesis, Porto University, 2010

82. Chang Huang, Pangpang Wang,Wen Guan, Sen Yang, Lumei Gao, Liqun Wang, Xiaoping Song , Ri-ichi Murakami; Improved microstructure and magnetic properties of iron-cobalt nanowire via an ac electrodeposition with a multistep voltage; Materials Letters 64, 2010, 2465–2467

83. Rosalinda Inguanta, Salvatore Piazza, Carmelo Sunseri; Influence of electrodeposition techniques on Ni nanostructures; Electrochimica Acta 53, 2008, 5766–5773

84. Kornelius Nielsch, Frank Müller, An-Ping Li, and Ulrich Gösele; Uniform Nickel Deposition into Ordered Alumina Pores by Pulsed Electrodeposition; Adv. Mater. 12, 2000, No. 8

85. Célia Tavares de Sousa, Development of Nanoporous Alumina Templates for Biotechnological Applications PhD thesis, University of Do Porto, 2011

86. Aneta J. Mieszawska, Romaneh Jalilian, Gamini U. Sumanasekera, and Francis P. Zamborini; The Synthesis and Fabrication of One-Dimensional Nanoscale Heterojunctions; small 3, 2007, No.5, 722-756

87. Guofeng Hu, Haiming Zhang, Wenwen Di and Tingting Zhao, "Study on wet etching of AAO template," Appl. Phys. Research1, No. 2, 2009

88. Guojun Song, Dong Chen, Zhi Peng, Xilin She, Jianjiang Li and Ping Han, Quantificational Etching of AAO Template, J. Mater. Sci. Technol. 23, No.3, 2007

89. Jinsub Choi; Fabrication of monodomain porous alumina using nanoimprint lithography and its applications; PhD thesis 2003; der Martin-Luther-Universität Halle-Wittenberg

90. L. Sun, Y. Hao, C.-L. Chien and P. C. Searson, Tuning the properties of magnetic nanowires, IBM J. RES. & DEV. 49, No. 1, 2005

91. Jiewu Cui, Yucheng Wu, Yan Wang, Hongmei Zheng, Guangqing Xu, Xinyi Zhang, A facile and efficient approach for pore-opening detection of anodic aluminum oxide membranes, Applied Surface Science 258, 2012, 5305– 5311

92. T. M. Whitney, J. S. Jiang, P. C. Searson, C. L. Chien, Fabrication and magnetic properties of arrays of metallic nanowires, Science 261, 1993

93. Kirill S. Napolskii, Ilya V. Roslyakov, Andrey A. Eliseev, Dmitry I. Petukhov, Alexey V. Lukashin, Shu-Fang Chen, Chuan-Pu Liu, Galin A. Tsirlin; Tuning the microstructure and functional properties of metal nanowire arrays via deposition potential, Electrochimica Acta 56, 2011, 2378–2384

94. S. J. Hurst, E. K. Payne, L. Qin and C. A. Mirkin; Multisegmented one-dimensional nanorods prepared by hard-template synthetic methods; Angew Chem Int Ed Engl. 45(17), 2006, 2672-92

95. Joon-rak Choi, Sang Jun Oh, Honglyoul Ju, and Jinwoo Cheon, Massive Fabrication of Free-Standing One-Dimensional Co/Pt Nanostructures and Modulation of Ferromagnetism via a programmable Barcode Layer Effect, Nano Lett. 5, No. 11, 2005

96. Daniele Perego, Silvia Franz, Massimiliano Bestetti, Laura Cattaneo, Stefano Brivio, Grazia Tallarida and Sabina Spiga; Engineered fabrication of ordered arrays of Au–NiO–Au nanowires; Nanotechnology 24, 2013, 045302

97. Guofeng Hu, Haiming Zhang, Wenwen Di & Tingting Zhao; Study on Wet Etching of AAO Template; Applied Physics Research 1, 2009

98. Ian M. Watt, The principles and practice of Electron microscopy, 2nd. ed., Cambridge, 1997

99. W. C. Nixon, The general principles of scanning electron microscopy, Phil. Trans. Roy. Soc. Lond. B. 261, 1971

100.   J. W. Edington, Practical electron microscopy in materials science, Herndon (India), 1976

101.   I. M. Watt, The principles and practice of electron microscopy, 2nd. ed., Cambridge, 1997

102.   D. B. Williams and C. B. Carter, Transmission electron microscopy: a textbook for material science, New York, 1996

103.   Mike McElfresh; Fundamentals of magnetism and magnetic measurements featuring qauntum design's magnetic propery measurement system, Quantum Design 1994

104.   M Sawicki, W Stefanowicz and A Ney, Sensitive SQUID magnetometry for studying nanomagnetism, Semiconductor Science and Technology 26 (6), 2011

105.   C. P. Poole, Electron Spin Resonance, Intercience Publishers, NewYork, 1967

106.   M. Paunovic and M.Schlesinger; Fundamentals of electrochemical deposition; Wiley: New York, 1998; pp 108-109

107.   Orinakova, R. Turonova, A. Kladekova, D. Galova, M. Smith, R. M; Recent developments in the electrodeposition of nickel and some nickel-based alloys; Journal of Applied Electrochemistry 36, 2006, 957

108.   E. Chassaing, M. Joussellin and R. Wiart, The kinetics of nickel electrodeposition inhibition by adsorbed hydrogen and anions, J. Electroanal. Chem.157, 1983, 75

109.   Xue Wei Wang, Guang Tao Fei, Xi Jin Xu, Zhen Jin, and Li De Zhang; Size-Dependent Orientation Growth of Large-Area Ordered Ni Nanowire Arrays; J. Phys. Chem. B,109, 2005, 24326-2433

110.   C.G. Jin, W. F. Liu, C. Jia, H. Q. Xiang, W. L. Cai, L. Z.Yao, and X. G. Li, High-filling, large-area Ni nanowire arrays and the magnetic properties, J. Cryst. Growth 258, 2003, 337

111.   Rosalinda Inguanta, Salvatore Piazza, Carmelo Sunseri, Influence of electrodeposition techniques on Ni nanostructures; Electrochimica Acta 53, 2008, 5766–5773

112.   linus Pauling, Atomic Radii and Interatomic Distances in Metals; J. Am. Chem. Soc. 69, 1947, 542

113.   Shu-Fang Chen, HaoHanWei, Chuan-Pu Liu,C.Y. Hsu, and J C A Huang, Microstructural effects on the magnetic and magneto-transport properties of electrodeposited Ni nanowire arrays, Nanotechnology 21, 2010, 425602

114.   F. Tian, Z. P. Huang and L. Whitmore, Fabrication and magnetic properties of Ni nanowire arrays with ultrahigh axial squareness , Phys. Chem. Chem. Phys., 14, 2012, 8537–8541

115.   Liana Movsesyan, Ina Schubert, Lilit Yeranyan, Christina Trautmann and Maria Eugenia Toimil-Molares; Influence of electrodeposition parameters on the structure and morphology of ZnO nanowire arrays and networks synthesized in etched ion-track membranes, Semiconductor Science and Technology, 31, Number 1, 2015

116.   Maria Eugenia Toimil-Molares, Characterization and properties of micro- and nanowires of controlled size, composition, and geometry fabricated by electrodeposition and ion-track technology, Beilstein J. Nanotechnol. 3, 2012, 860–883

117.	E.A. Dalchiele, R.E. Marotti, A. Cortes, G. Riveros, H. Go´mez, L. Martı´nez, R. Romero, D. Leinen, F. Martin, J.R. Ramos-Barrado; Silver nanowires electrodeposited into nanoporous templates: Study of the influence of sizes on crystallinity and structural properties; Physica E 37, 2007, 184–188

118.	Hui Pan , Binghai Liu , Jiabao Yi , Cheekok Poh , Sanhua Lim , Jun Ding , Yuanping Feng , C. H. A. Huan , and Jianyi Lin; Growth of Single-Crystalline Ni and Co Nanowires via Electrochemical Deposition and Their Magnetic Properties; J. Phys. Chem. B, 109 (8), 2005, pp 3094–3098

119.	I.Z. Rahman, K.M. Razeeb, Md. Kamruzzaman, Marina Serantoni; Characterisation of electrodeposited nickel nanowires using NCA template; Journal of Materials Processing Technology 153–154, 2004, 811–815

120.	A. Encians-Oropesa, M. Demand, L. Piraux, I. Huynen, and U. Ebels, Dipolar interactions in arrays of nickel nanowires studied by ferromagnetic resonance, Physical Review B, 63, 2001

121.	M. Vazquez, K. Pirota, M. Hernandez-Ve lez, V. M. Prida, D. Navas, R. Sanz, and F. Batallan, Magnetic properties of densely packed arrays of Ni nanowires as a function of their diameter and lattice parameter, J. Appl. Phys., 95, No. 11, 2004

122.	V. Vega, V. M. Prida, J. A. Garcia, and M. Vazquez, Torque magnetometry analysis of magnetic anisotropy distribution in Ni nanowire arrays Phys. Status Solidi A 208 (3), 2011

123.	K. Nielsch, R.B. Wehrspohn, S.F. Fischer, H. Kronmüller, J. Barthel, J. Kirschner, and U. Gösele, Magnetic Properties of 100 NM-Period Nickel Nanowire Arrays Obtained from Ordered Porous-Alumina Membranes, Mat. Res. Soc. Symp. Proc. 636, 2001

124.	J. Escrig and D. Altbir, Remanence of Ni nanowire arrays: influence of size and labyrinth magnetic structure, Physical review B 75, 2007, 184429

125.	Y. P. Ivanov, M Vazquez and O Chbykalo-Fesenko; Magnetic reversal modes in cylindrical nanowires; J. Phys. D: Appl. Phys. 46, 2013, 485001

126.   C. Bran, Yu. P. Ivanov, J. Garcia, R. P. del Real, V.M. Prida, O. Chubykalo-Fesenko and M. Vazquez, Tuning the magnetization reversal process of FeCoCu nanowire arrays by thermal annealing , J. Appl. Phys. 114, 2013, 043908

127.   P. Toson, W. Wallisch, A. Asali and J. Fidler, Modelling of Packed Co Nanorods for Hard Magnetic Applications, EPJ Web of Conferences 75, 2014, 03002

128.   Sara Liébana Viñas, Anisotropic cobalt-based nanostructures: synthesis and characterization, PhD thesis, Duisburg-Essen university, 2015

129.   I. Panagiotopoulos, W.Fang, F. Ott, F. Boué, K. Ait-Atmane, J-Y. Piquemal and G.Viau, Packing fraction dependence of the coercivity and the energy product in nanowire based permanent magnets, J. Appl. Phys. 114, 2013, 143902

130.   R. Skomski, Y. Liu, J.E. Shield, G.C. Hadjipanayis and D.J. Sellmyer, Permanent magnetism of dense-packed nanostructures, J. Appl. Phys. 107, 09A739, 2010

131.   V. Vega, T. Böhnert, S. Martens, M. Waleczek, J. M. Montero-Moreno, D. Görlitz, V. M. Prida, and K. Nielsch, Tuning the magnetic anisotropy of Co-Ni nanowires: comparison between single nanowires and nanowire arrays in hard-anodic aluminum oxide membranes, Nanotechnology 23, 2012, 465709

132.   D. J. Sellmyer, M. Zheng, and R. Skomski, Magnetism of Fe, Co and Ni nanowires in self-assembled arrays, J. Phys.: Condensed. Matter 13, 2001, R433-R460

133.   A. Encinas-Oropesa, M. Demand, L. Piraux, U. Ebels and I. Huynen, Effect of dipolar interactions on the ferromagnetic resonance properties in arrays of magnetic nanowires, Journal of applied physics 89, 2001

134.   T. Wang, Y. Wang, Y. Fu, T. Hasegawa, F. S. Li, H Saito, and S. Ishio; A magnetic force microscopy study of the magnetic reversal of a single Fe nanowire; Nanotechnology 20, 2009, 105707

135.   Y. Henry, K. Ounadjela, L. Piraux, S. Dubois, J.-M. George and J.L. Duvail, Magnetic anisotropy and domain patterns in electrodeposited cobalt nanowires, Eur. Phys. J. B 20, 2001

136.   L.G. Vivas, J. Escrig, D. G. Trabada, G. A. Badini-Confalonieri and M. Vázquez, Magnetic anisotropy in ordered textured Co nanowires, Appl. Phys. Lett.100, 2012

137.   Donald R. Askelan, Wendelin J. Wright; The Science and Engineering of Materials (seventh Edition); 2016

138.   C.A. Ramos, M. Vazquez, K. Nielsch, K. Pirota, J. Rivas, R.B. Wehrspohn, M. Tovar, R.D. Sanchez and U. Gösele, FMR characterization of hexagonal arrays of Ni nanowires Journal of Magnetism and Magnetic Materials 272–276 (2004) 1652–1653

139.   U. Ebels, J. L. Duvail, P. E. Wigen, L. Piraux, L. D. Buda, and K. Ounadjela, Ferromagnetic resonance studies of Ni nanowire arrays, Physical review B 64, 2001, 144421

140.   M. K. Gupta, T. König , R. Near, D. Nepal, L. F. Drummy, S. Biswas, S. Naik, R. A. Vaia, M. A. El-Sayed, V. V. Tsukruk, Surface assembly and plasmonic properties in strongly coupled segmented gold nanorods, small 9, 2013, 2979-90

141.   G. Giallongo, C. Durante, R. Pilot, D. Garoli, R. Bozio, F. Romanato, A. Gennaro, G. A. Rizzi and G. Granozzi, Growth and optical properties of silver nanostructures obtained on connected anodic, Nanotechnology 23, 2012, 325604

142.   Yugang Sun; Silver nanowires unique templates for functional nanostructures; Nanoscale 2, 2010; 1626-1642

143.   B. Willey, Y. Sun, and Y. Xia; Synthesis of silver nanostructures with controlled shapes and properties; Acc. Chem. Res. 2007, 40, 1067-1076

144.   Min Kyung Oh, Hyo Jin Baik, Seong Kyu Kim and Sungho Park; multiple surface plasmon resonances in silver and copper nanorods, J. Mater. Chem. 21, 2011, 19069-19073

145.   Rui-Long Zong, Ji Zhou, Qi Li, Bo Du, Bo Li, Ming Fu, Xi-Wei Qi, and Long-Tu Li; Synthesis and optical properties of silver nanowire arrays embedded in anodic alumina; J. Phys. Chem. B, 2004, 108, 16713-16716

146.   G. Schider, J. R. Krenn, A. Hohenau, H. Ditlbacher, A. Leitner, and F. R. Aussenegg; plasmon dispersion relation of Au and Ag nanowires; Physical review B, 68, 2003, 155427

147.   Zhi Yang, Minqiang Wang, Guodong Yan, Xiangyu Zhang, Jijun Ding; Optical properties of silver nanorods by adjusting aspect ratio in experiment and simulation;Proceedings of the 13th IEEE International Conference on Nanotechnology Beijing, China, 2013

148.   Hong Wei, Alejandro Reyes-Coronado, Peter Nordlander, Javier Aizpurua, and Hongxing Xu; Multipolar plasmon resonance in individual Ag nanorice; Acs Nano; 4; No. 5; 2012; 2649–2654

149.   B. Sepúlveda, A. Calle, L. M. Lechuga, and G. Armelles, Highly sensitive detection of biomolecules with the magneto-optic surface-plasmon-resonance sensor, Optics Letters, 31, No. 8, 2006,1085-1087

150.   Kishore Sridharan, Tamio Endo, Sang-Geun Cho, Jongryoul Ki, Tae Joo Park, Reji Philip, Single step synthesis and optical limiting properties of Ni–Ag and Fe–Ag bimetallic nanoparticles, J. Mater. Chem. 22, 2012, 6899–6906

151.   Lei Wang, Cesar Clavero, Zachary Huba, Kyler J. Carroll, Everett E. Carpenter, Diefeng Gu,| and Rosa A. Lukaszew, Plasmonics and enhanced magneto-optics in core-shell Co-Ag nanoparticles, Nano lett. 11, 2011, 1237-1240

152.   J. Erlebacher, P.C. Searson, and K. Sieradzki, Computer-Simulations of dense-branching patterns, Phys. Rev.Lett. 71, 1993, 3311

153.   B. Lim , M. Jiang, P. H. C. Camargo, E. C. Cho, J. Tao, X. Lu, Y. Zhu, Y. Xia, Pd-Pt Bimetallic Nanodendrites with High Activity for Oxygen Reduction, Science 324, 2009 , 1302

154.   K. J. Major, De Chandrima, Obare Sherine, Recent Advances in the Synthesis of Plasmonic Bimetallic Nanoparticles, Plasmonics 4, 2009 , 61

155.   A. Kolmakov, Y. Zhang, M. Moskovits, Topotactic thermal oxidation of Sn nanowires: Intermediate suboxides and core-shell metastable structures, Nano Lett. 2003, 3, 1125

156.   K. Chatterjee, S. Basu, D. Chakravorty, Plasmon resonance absorption in sulfide-coated gold nanorods, Journal of Materials Research 21, 2006, 34

157.   J. A. Sioss, and C. D. Keating, Batch preparation of linear Au and Ag nanoparticle chains via wet chemistry, Nano Lett. 5, 2005, 1779

158.   G. Armelles, A. Cebollada, A. García-Martín, J. M. Montero-Moreno, M. Waleczek, K. Nielsch, Magneto-optical properties of core-shell magneto-plasmonic Au-Co(x)Fe(3 - x)O4 nanowires, Langmuir 28, 2012 9127-30.

159.   N. I. Kovtyukhova, B. K. Kelley, T. E. Mallouk, Coaxially gated in-wire thin-film transistors made by template assembly, J. Am. Chem. Soc.2004, 126, 12738

160.   N. I. Kovtyukhova, T. E. Mallouk, Nanowire p-n heterojunction diodes made by templated assembly of multilayer carbon-nanotube/polymer/semiconductor-particle shells around metal nanowires, Adv. Mater. 2005, 17, 187

161.   V. M. Cepak, J. C. Hulteen, G. Che, K. B. Jirage, B. B. Lakshmi,E. R. Fisher, and C. R. Martin, Chemical strategies for template syntheses of composite micro- and nanostructures , Chem. Mater. 1997, 9, 1065

162.   J.R. Ku, R. Vidu, R. Talroze, P. Stroeve, Fabrication of nanocables by electrochemical deposition inside metal nanotubes, J. Am. Chem. Soc. 2004,126, 15022

163.   Y. Wu, T. Livneh, Y. X. Zhang, G. Cheng, J. Wang, J. Tang, M.Moskovits, G. D. Stucky, Templated synthesis of highly ordered mesostructured nanowires and nanowire arrays, Nano Lett. 2004, 4, 2337

164.   N. I. Kovtyukhova, T. E. Mallouk, T. S. Mayer, Templated surface sol-gel synthesis of SiO2 nanotubes and SiO2-insulated metal nanowires, Adv. Mater. 15, 2003, 780

165.   Shih-Chin Lin, San-Yuan Chen, Yun-Tien Chen, Syh-Yuh Cheng, Electrochemical fabrication and magnetic properties of highly ordered silver–nickel core-shell nanowires, Journal of Alloys and Compounds 449, 2008, 232–236

166.   M. Mckiernan, Jie Zeng, Suzida Ferdous, Facile Synthesis of Bimetallic Ag/Ni Core/Sheath Nanowires and Their Magnetic and Electrical Properties, Small 6, 2010, No. 17, 1927-1934

167.   Emilio C. C. M. Silva, Limin Tong, Sidney Yip, and Krystyn J. Van VliSize Effects on the Stiffness of Silica Nanowires, small 2, 2006, No. 2, 239 – 243

168.   Xian-Fang Li, Bao-Lin Wang, and Kang Yong Lee, Size effects of the bending stiffness of nanowires, Journal of applied physics 105, 2009, 074306

169.   K. P. Musselman, G. J. Mulholland, A. P. Robinson, L. Schmidt-Mende and J. L. MacManus-Driscoll, Low-Temperature Synthesis of Large-Area, Free-Standing Nanorod Arrays on ITO/Glass and other Conducting Substrates, Adv. Mater. 20, 2008, 4470

170.   Sara Liébana Viñas, Ruslan Salikhov, Cristina Bran, Ester M. Palmero, Manuel Vazquez, Behnaz Arvan, Xiang Yao, Peter Toson, Josef Fidler, Marina Spasova, Ulf Wiedwald, Michael Farle, Magnetic hardening of $Fe_{30}Co_{70}$ nanowires, Nanotechnology 26, 415704 (2015)

Acknowledgments

I would like to appreciate those people who have helped me during my Ph.D study.

First, I would like to express my sincere gratitude to my advisor Prof. Dr. Michael Farle for the continuous support of my Ph.D study, for his patience, and motivation. I would like to thank Prof. Farle for creating a friendly working atmosphere and bringing me to the world of the nanoscale magnetism with spending many hours in discussions. His advices and his immense knowledge helped me during my research and writing my thesis.

Beside my supervisor, I am thankful to Prof. Dr. Manuel Vazquez, from the Institute of materials science of Madrid, Prof. Dr. Pencheva, and Prof. Dr. Lorke at the University of Duisburg-Essen, whom accepted to be a member of the committee.

I am very grateful to thank Priv. Doz. Dr. Ulf Wiedwald and Dr. Marina Spasova for sharing with me their knowledge of magnetism at the nanoscale, and for their support, and hours of discussions, as well as explanations of measurement techniques. Special thanks to Dr. Wieldwald for his correcting manuscripts and translating the abstract of this thesis from English to German language.

I highly appreciate Dipl. Ing. Horst Zähres for his great cooperation for fabricating the required systems, such as anodization system that it was explained in chapter 3. I am thankful him for helping me in the chemistry lab, solving the technical problems, and sharing his experience and his encyclopedic knowledge of chemistry with me, as well as for his correcting manuscripts and his great advices. Many thanks to Dr. Sara Liébana-Viñas for her help in chemistry lab and her support.

Many thanks to Dr. Ruslan Salikhov, Prof. Dr. Mehmet Acet, and Dr. Ralf Meckenstock for their explanations and discussions of my results during my study. Special thanks to Dr. Salikhov for his explanations of FMR spectroscopy and guided me in the study of the Ni nanowires.

I am thankful Dr. Zi-An Li, Zheng Ma, and Dr. Anna Elsukova for the work on the structural and crystallinity of the Ni nanowires with the TEM. Dr. Jens Theis and Dr. Nathalie Reckers are knowledged for their explanations of UV/Vis spectroscopy and SEM system, respectively. Many thanks to Ms. Helga Mundt and Ms. Sabina Grubba for their great

List of own publication

1. Magnetic hardening of Fe30Co70 nanowires.
S. Liébana Viñas, R. Salikhov, C. Bran, E. M. Palmero, M. Vazquez, B. Arvan, X. Yao, P. Toson, J. Fidler, M. Spasova, U. Wiedwald and M. Farle.
Nanotechnology 26, 415704 (2015)
DOI:10.1088/0957-4484/26/41/415704

2. Segmented Nickel-Silver-Nickel Nanowires Produce Multiple Surface Plasmon Bands.
Behnaz Arvan, Marina Spasova, Leonardo Scarabelli, Horst Zähres, Zi-An Li, Luis M. Liz-Marzán, Michael Farle, Ulf Wiedwald
In preparation.

3. Structural and magnetic properties of Ni nanowires.
Behnaz Arvan, Marina Spasova, Zi-An Li, Horst Zähres, Ulf Wiedwald, Michael Farle
In preparation.